Universitat Autònoma de Barcelona

Transverse beam dynamics studies from turn-by-turn beam position monitor data in the ALBA storage ring

Michele Carlà

Universitat Autònoma de Barcelona

Faculty of Science - Department of Physics

2017

Ph.D. dissertation by

Michele Carlà

Transverse beam dynamics studies from turn-by-turn beam position monitor data in the ALBA storage ring

Director:

Dr. Gabriele Benedetti
ALBA-CELLS

Tutor:

Prof. Javier Rodríguez Viejo
Universitat Autònoma de Barcelona

Jury:

Dr. Caterina Biscari
ALBA-CELLS

Dr. Yuri Kubyshin
Universitat Politècnica de Catalunya

Dr. Ian Martin
Diamond Light Source and University of Oxford

Dr. Francis Pérez
ALBA-CELLS

Prof. Lluís Garrido
Universitat de Barcelona

Contents

Introduction

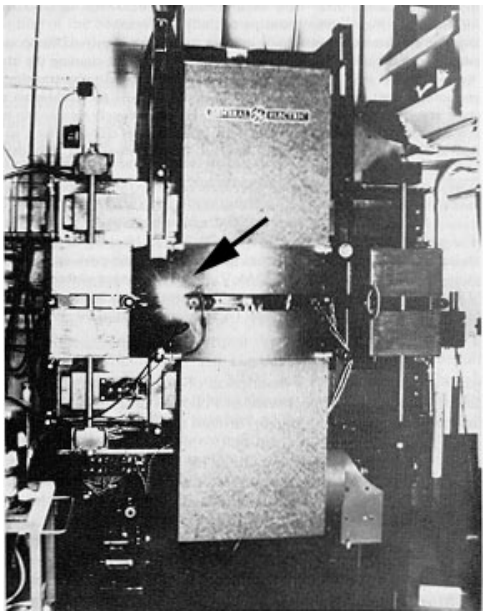

FIGURE 0.1. The 70 MeV electron synchrotron at the General Electric Company (Schenectady, New York) in 1947. A glass beampipe made it possible to observe the synchrotron radiation for the first time.

ALBA is a third generation light source, commissioned in 2011, serving a national and international scientific and industrial community. It provides synchrotron radiation up to the hard x-rays as a tool to multiple laboratories (beamlines) for a wide range of physical, chemical, and biological experiments.

In order to achieve the required radiation flux and small divergence, the electron storage ring employs an optimized design where strong magnets (dipoles, quadrupoles and sextupoles) are combined in a rather complex lattice to properly shape the characteristics of the electron beam. However, the lattice can have several errors, which detrimentally affect the electron beam characteristics such as size, divergence, or lifetime.

Unavoidable lattice errors can be due to manufacturing mechanical tolerances, magnet hysteresis, thermal variations and/or mechanical misalignments. The delicate "magnetic equilibrium" required to operate such light sources could be hardly met without a tool to measure and correct the actual magnetic lattice. For this purpose beam-based methods, where the stored beam serves as probe to inspect the lattice, have been developed [**45**] during the past years.

Closed orbit response matrix measurement methods received particular attention in the light sources community, and at ALBA it has been the workshorse to measure and correct magnet lattice errors [**11**].

In the closed orbit response matrix measurements approach, the orbit corrector magnets are varied one after the other and the resulting orbit change monitored using the Beam Position Monitors (BPMs). The dependency of the orbit change on the lattice parameters is then inverted in order to reconstruct a set of lattice errors. The large number of corrector magnets and BPMs allows to reconstruct an accurate linear lattice error model. However, the high precision of the closed orbit response matrix method comes at the cost of a time consuming measuring process, typically around 10 minutes in a synchrotron.

A different approach, commonly used in larger rings such as colliders, where the large number of lattice elements prevents from using a closed orbit approach, is provided by beam position turn-by-turn measurements. By abruptly displacing (ping) the beam from its equilibrium transverse orbit, and sampling the resulting transverse motion turn after turn, the lattice errors model is inferred. Since only a fast kicker magnet (pinger) is used, the method is in principle faster than the orbit response matrix approach. Furthermore, turn-by-turn measurements allow to separate easily the contribution of linear and non-linear lattice components that happen to affect different oscillatory modes of the transverse beam motion. Unfortunately an accurate turn-by-turn measurement requires special high bandwidth BPM electronics that usually are not included in the ordinary diagnostic instrumentation of a synchrotron light source.

The main purpose of this PhD work is to implement for the first time the turn-by-turn technique at ALBA in order to establish the capabilities of the measurements in the context of linear and non-linear lattice errors. Joining the effort to

test the capabilities of the turn-by-turn technique already underway in other light sources [**8, 10, 21, 37**], we conducted a series of experiments at the ALBA synchrotron, employing the state of the art BPMs electronics. In addition we repeat a similar set of experiments at the SOLEIL synchrotron, to compare them with previous tests [**46**] and confirm the reliability of the turn-by-turn method in third generation of synchrotron light sources.

Furthermore, the achieved precision of the turn-by-turn technique in this PhD work allows to apply it for the first time to characterize multiple transverse coupling impedance sources in a synchrotron light source. The electromagnetic interaction of the stored beam with the vacuum chamber (commonly known as coupling impedance) introduces a coupling mechanism to the beam motion, which can result in a beam instability if certain conditions are met. The PhD thesis shows that the characterization of the coupling impedance can be obtained with a technique similar to the ones used to monitor the magnetic lattice, since the presence of an impedance source is always accompanied by a local small beam defocusing.

The work is organized as follows:

In the first section of Chapter 1 the basic physics of a storage ring is introduced with particular attention to the linear transverse beam dynamics. In the second section the effect of linear, coupling and non-linear perturbations on the transverse beam dynamics are studied with a perturbative approach. A set of approximated analytical formula, that will be employed in the analysis of the experimental results, are derived.

In Chapter 2 the lattice of ALBA and SOLEIL are presented. Moreover the ALBA lattice is employed to carry out a series of tests where the approximated analytical formula derived in the previous chapter are compared against numerical simulations (tracking) to prove their validity.

In Chapter 3 an introduction to the basics of a BPM system is provided. Furthermore technical details of the BPM system employed in the ALBA and SOLEIL storage rings are presented.

Chapter 4 covers the description of the ALBA pinger magnet. In fact to carry out turn-by-turn measurements, the installation of a purposely build system of pulsed magnets (pingers) was required. Here the working principles of the magnet

are described and the main working parameters of the pingers are derived. Finally the first laboratory measurements are presented.

Chapter 5 covers the description of the experimental turn-by-turn set-up employed at ALBA and SOLEIL. Particular attention is devoted to the case of ALBA, where turn-by-turn measurements have been implemented for the first time. The description cover the set-up of the BPMs, the calibration of the pinger magnets and the set-up of the storage rings lattice.

The first results of the linear lattice measurements from turn-by-turn data are presented in Chapter 6, covering tune, betatron amplitude and phase measurements and a comparison with the nominal lattice models. Furthermore an analysis of the measurment errors is carried out.

In Chapter 7, the measurement technique introduced in Chapter 6, has been put under test by carrying out a series of experiments where known sources of gradient error (quadrupolar error) have been introduced in the storage ring lattices, therefore the results of the measurements have been compared against the expected values. Moreover the test is extended to skew-quadrupoles and sextupoles in order to demonstrate the capabilities of turn-by-turn measurements to characterize coupling sources and non-linear lattice elements.

Finally in Chapter 8 the turn-by-turn technique is extended to the characterization of multiple transverse coupling impedance sources in the ALBA storage ring.

CHAPTER 1

Transverse beam dynamics in a storage ring

1.1. Transverse linear optics

1.1.1. *Basic storage ring design*

Storing and confining in space a beam of high energy charged particles is one of the main and most complex tasks that has to be performed by a circular particle accelerator.

Magnetic and electric fields are the tools at our disposal to displace electric charges. Unfortunately electric fields get quickly non effective when high energy particles are involved, requiring excessively high field strength in order to bend noticeably their trajectory. A magnetic field as the one produced by a conventional iron-core magnet is instead an effective tool to manipulate high energy particles.

As a first attempt we can try to confine a particle by means of a simple constant and uniform magnetic field orthogonal to the direction of motion of the particle itself. The same way as a stone tied at the end of a string is whirled around on a circle, the particle would move around in a circular orbit under the effect of the Lorentz force.

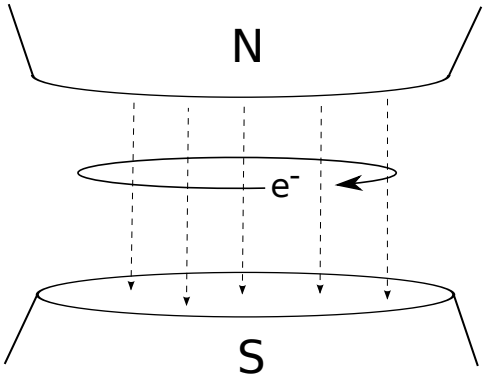

FIGURE 1.1. An electron surrounded by a magnetic field and moving perpendicularly to the field lines is trapped on a circular path as a result of the Lorentz force.

This is the very fundamental principle behind storage rings, where magnetic fields are used to "trap" charged particles on a closed path. The magnetic field responsible for bending the particles is provided by many dipolar magnets (bending magnets), as shown in Fig. 1.2 and the resulting design orbit consists of a sequence of arcs, corresponding to the dipole magnets which bend the particle trajectory, and straight sections.

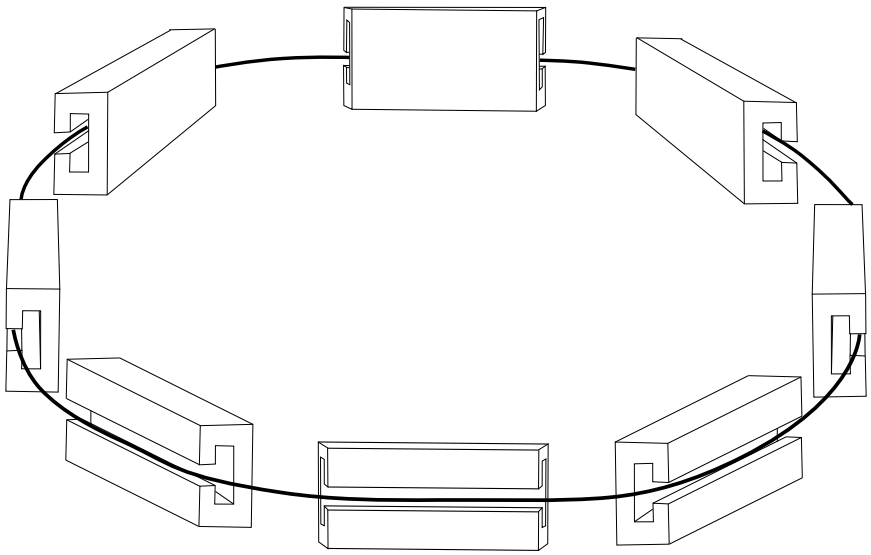

FIGURE 1.2. A rudimentary storage ring made of bending magnets only. Instead of using one huge magnet to produce the field required to bend the particle trajectory many smaller magnets provides a viable solution.

The presence of empty straight sections provides useful space required to host many other necessary devices vital to the accelerator.

Unluckily our rudimentary design would not be free of shortcomings. For instance, the "trapping" would be achieved only for a particle moving perpendicularly to the field, whereas a trajectory non perpendicular to the field would produce a helical orbit rather than a closed orbit and therefore an unbound motion. What is missing to achieve an effective confined particle motion is a restoring force (focusing) that deflects the particle toward the design orbit each time they try to escape. In other words, the reference orbit has to become an equilibrium curve for the particles.

To help the following discussion we need to define a reference frame. It is a common choice to define a transverse frame moving along the path of an imaginary

particle on the design orbit as shown in Fig. 1.3, where s represents the longitudinal position along the ring, while x and y denote the transverse displacements with respect to the reference orbit.

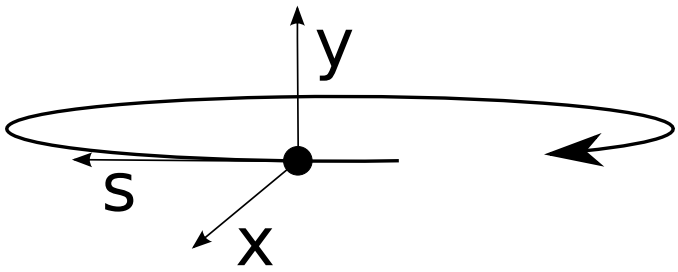

FIGURE 1.3. Coordinates are defined in a reference frame comoving with an ideal particle traveling exactly on the design orbit.

The focusing can be achieved by introducing a proper transverse gradient in the magnetic field. Quadrupole magnets are the choice of reference when a linear magnetic field gradient is required. Figure 1.4 shows how the four poles of a quadrupole magnet are arranged in such a way that the magnetic field vanishes at the center of the magnet and increases linearly when moving away from it. In analogy with the

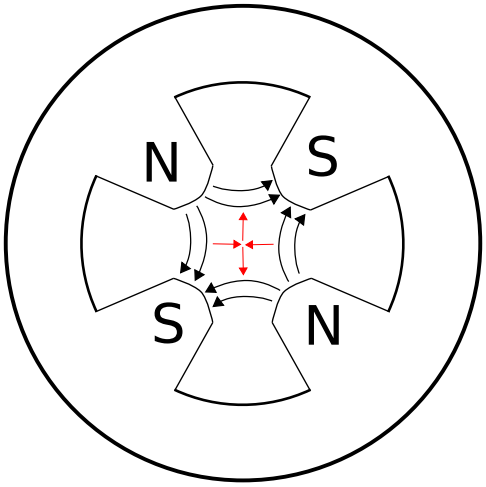

FIGURE 1.4. Transverse cross section of a quadrupole magnet. In a quadrupole four magnetic poles are arranged in such a way to produce a linear magnetic gradient that vanishes on its center. The pole tips are shaped to ensure a good linearity of the field in a large region of space. Black arrows shows the magnetic field, while red ones represent the Lorentz force for a negative particle traveling toward the image plane.

case of optical lenses, a particle crossing the quadrupole travels unaffected when

passing through the center of the magnet while experiences a transverse force that increases linearly moving away from the center as shown in Fig. 1.5.

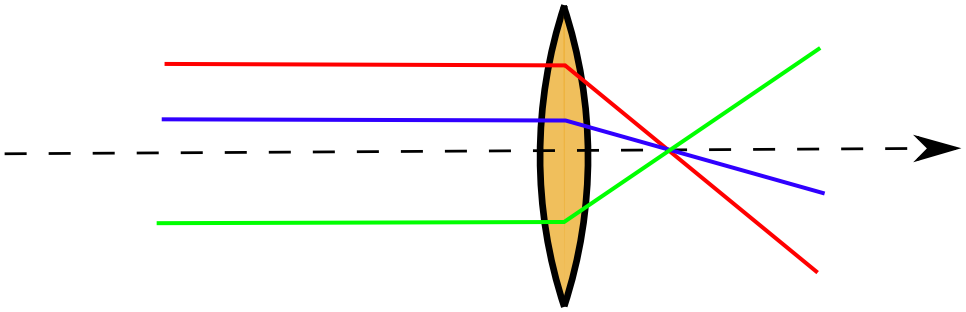

FIGURE 1.5. Particles crossing the center of the quadrupole travel unaffected while are deflected when passing off axis. As in a lens particles traveling on parallel trajectories cross the quadrupole and get deflected toward a focal point.

An explicit expression of the magnetic field produced in the transverse plane by a quadrupole magnet is:

$$\begin{cases} B_y = Gx \\ B_x = -Gy, \end{cases} \tag{1.1}$$

where, exploiting Maxwell's equations and the particular symmetry of the field, the two components have been written through the field gradient $G = \frac{\partial B_y}{\partial x}\big|_0$. A common way to provide the strength of a quadrupole magnet is through the normalized gradient K defined as:

$$K = G\frac{e}{pc}, \tag{1.2}$$

with e and p respectively the charge and momentum of the particles and c the speed of light.

It is important to note that such magnetic field arrangement is not able to focus the particle trajectory in the vertical and horizontal planes at the same time. Focusing the beam in the horizontal plane induces a defocusing effect in the vertical plane and vice versa. Nevertheless, it is possible to combine alternating focusing and defocusing quadrupoles with suitable strength and distance in order to obtain an overall focusing effect on both planes [**18**].

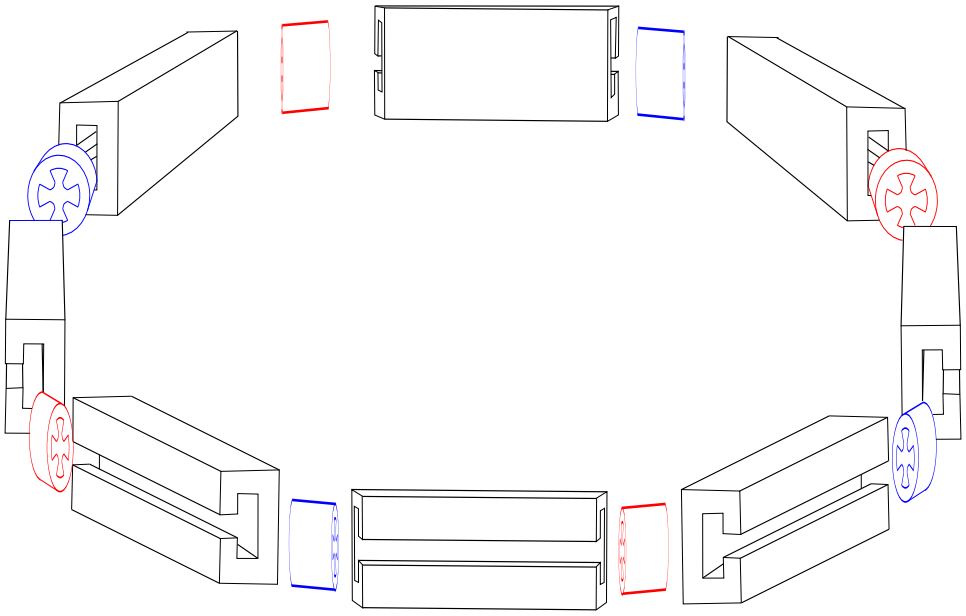

FIGURE 1.6. Quadrupoles are placed in between dipoles to overcome the lack of focusing of the previous design. Since a single quadrupole is not able to achieve focusing on both planes at the same time, horizontal focusing quadrupoles (in red) are alternated with vertical focusing quadrupoles (in blue) to obtain an overall focusing effect on both planes. The contribution of quadrupoles defines the periodicity of the magnetic lattice, now made of 4 identical cells each one comprising two bending magnets, one focusing and one defocusing quadrupole.

We proceed by adding very naively to our machine a few quadrupoles in the free space left in between the bending magnets bringing our accelerator a bit closer to what a real storage ring looks like. Of course such simplified approach if far away from reality, in fact since the overall beam characteristics are mainly determined by the magnets arrangement, commonly referred as the magnetic lattice, a complex lattice design process is always involved in order to meet the required performances.

Leaving aside the difficulty of the lattice design process itself, that represents a very complex topic by its own, we proceed with an introduction to the principles of the transverse dynamic of the particles confined in the storage ring.

The understanding of the transverse particle motion in a storage ring requires the study of the interaction of the particle with the different components of the magnetic lattice, that in our simplified design is made of a combination of three

different linear elements: bending magnets, focusing and defocusing quadrupoles magnets and empty space in between.

1.1.2. *Betatron oscillations*

A stored particle follows a similar dynamics in the vertical and horizontal planes defined by the Hill's equation [**48**]:

$$\frac{d^2u(s)}{ds^2} \pm K(s)u(s) = 0, \tag{1.3}$$

where $u(s)$ is the particle coordinate in the vertical or the horizontal plane and the s-dependent function $K(s)$ represents the focusing and defocusing quadrupole strength which shows opposite sign in the horizontal and vertical planes, reflecting the signs of Eq. 1.1

Since quadrupoles fill only a portion of the storage ring, the function $K(s)$ behaves as a step function that vanishes everywhere except across quadrupoles.

There is a strict similarity between the Hill's equation and a generalized harmonic oscillator, the only difference being that the force $K(s)$ is not constant in time but varies continuously between different values including also negative ones. Therefore we expect a stored particle to move following an almost harmonic motion with a time constant that changes from time to time according to the quadrupole being crossed, while drifting when passing trough a straight section or a bending magnet where no magnetic field gradient is present.

The Hill's equation belongs to the class of the second-order linear ordinary differential equations with the peculiarity of $K(s)$ being a periodic function, whose period C equals to the circumference of the storage ring, therefore satisfying the condition $K(s) = K(s + C)$. In fact a particle stored in the ring after having completed one turn will experience the same lattice as the turn before. In other words the interaction between a particle and the fields produced by the storage ring lattice is intrinsically periodic with a periodicity set by the storage ring circumference (or a higher periodicity in the very common case of a periodic magnetic lattice).

Being $K(s)$ a step-like continuous periodic function we can solve Eq 1.3 using the Floquet theorem. This states that the solution of such equation, if it exists, can be decomposed as the product of a real function with the same periodicity of

$K(s)$ times an oscillatory term. Therefore we look for a solution of the form:

$$u(s) = Aw(s)\cos(\psi(s) + \psi_0), \tag{1.4}$$

where the envelope function $w(s)$ satisfies the periodicity condition $w(s) = w(s + C)$ and the phase $\psi(s)$ is a s-dependent function. The two constants A and ψ_0 are defined by the initial condition of the motion and account for the oscillation amplitude and the initial phase, respectively.

To find an explicit solution for Eq. 1.3 we proceed by derivating Eq. 1.4 two times with respect to the longitudinal position s:

$$u'' = A(w'' - w\psi'^2)\cos(\psi + \psi_0) - A(2w'\psi' + w\psi'')\sin(\psi + \psi_0), \tag{1.5}$$

where we dropped the function argument s to ease the notation. Substituting Eq. 1.4 and 1.28 in Eq. 1.3 and separating the phase and quadrature parts we obtain a system of two equations:

$$\begin{cases} w'' - w\psi'^2 + kw = 0 & \text{(1.6a)} \\ 2w'\psi' + w\psi'' = 0. & \text{(1.6b)} \end{cases}$$

Eq. 1.6b establishes a relation between the phase function $\psi(s)$ and the amplitude function $w(s)$ and integrating one time with respect to s we get:

$$\psi'(s) = \frac{1}{w^2(s)}, \tag{1.7}$$

and hence

$$\psi(s) = \psi(s_0) + \int_{s_0}^{s} \frac{1}{w^2(s')} ds'. \tag{1.8}$$

To determine $w(s)$ we substitute Eq. 1.7 into Eq. 1.6a resulting in a new equation that now depends only on $w(s)$ and the function $K(s)$:

$$w''(s) + K(s)w(s) = \frac{1}{w^3(s)}. \tag{1.9}$$

While solving directly Eq. 1.9 is possible, it is preferable to follow a slightly different approach.

Given two locations in the storage ring s_1 and s_2 the coordinates of a particle at location s_2 can be expressed as a function of the coordinate at s_1 using Eq. 1.4 by the transformation:

$$
\begin{aligned}
u_2 &= \left[\frac{w_2}{w_1}\cos(\Delta\psi) - w_2 w_1' \sin(\Delta\psi)\right] u_1 + w_1 w_2 \sin(\Delta\psi) u_1', \\
u_2' &= \left[-\frac{1 + w_1 w_2' w_2 w_2'}{w_1 w_2}\sin(\Delta\psi) - (\frac{w_1'}{w_2} - \frac{w_2'}{w_1})\cos(\Delta\psi)\right] u_1 + \\
&\qquad \left[\frac{w_1}{w_2}\cos(\Delta\psi) + w_1 w_2' \sin(\Delta\psi)\right] u_1',
\end{aligned} \tag{1.10}
$$

where $\Delta\psi = \psi(s_2) - \psi(s_1)$ is the *phase advance* between s_1 and s_2. The above system is conveniently represented in matrix form by:

$$
\vec{u}_2 = M(s_1 \to s_2)\vec{u}_1, \tag{1.11}
$$

where we introduced the particle coordinate vector $\vec{u}$ defined as:

$$
\vec{u}(s) = \begin{pmatrix} u(s) \\ u'(s) \end{pmatrix}, \tag{1.12}
$$

and the matrix $M(s_1 \to s_2)$, commonly referred to as the transfer matrix, is defined by:

$$
M(s_1 \to s_2) = \tag{1.13}
$$

$$
\begin{bmatrix}
\frac{w_1}{w_2}\cos(\Delta\psi) - w_2 w_1' \sin(\Delta\psi) & w_1 w_2 \sin(\Delta\psi) \\
\begin{pmatrix} (\frac{w_2'}{w_1} - \frac{w_1'}{w_2})\cos(\Delta\psi) + \\ -\frac{1+w_1 w_2 w_1' w_2'}{w_1 w_2}\sin(\Delta\psi) \end{pmatrix} & \frac{w_1}{w_2}\cos(\Delta\psi) + w_1 w_2' \sin(\Delta\psi)
\end{bmatrix}.
$$

The ability to represent coordinates transformations with a matrix formalism proves to be a particularly convenient tool to study linear optics. In fact once defined the transfer matrix for each single element in the storage ring (i.e. straight sections and quadrupoles), finding the transfer matrix between two arbitrary locations is only matter of concatenating all the transformations representing the elements contained in between:

$$
M(s_1 \to s_N) = M_N \cdot M_{N-1} \cdot \ldots \cdot M_2 \cdot M_1. \tag{1.14}
$$

The one-turn transfer matrix is of particular interest. In this case the two locations s_1 and s_2 coincide and the matrix $M(s)$ represents the coordinate transformation for a particle that starting from a given location $s = s_1 = s_2$ completes one turn around the storage ring. In this case the matrix $M = M(s_1 \rightarrow s_2)$ simplifies and can be represented by the matrix:

$$M(s) = \begin{pmatrix} \cos(\nu) + \alpha \sin(\nu) & \beta \sin(\nu) \\ -\gamma \sin(\nu) & \cos(\nu) - \alpha \sin(\nu) \end{pmatrix}, \tag{1.15}$$

where β, α and γ are the Courant-Snyder parameters defined as [1]:

$$\begin{aligned} \beta(s) &\equiv w^2(s), \\ \alpha(s) &\equiv -\frac{1}{2}\beta'(s), \\ \gamma(s) &\equiv \frac{1+\alpha^2(s)}{\beta(s)}, \end{aligned} \tag{1.16}$$

and ν represents the overall phase advance of the storage ring, commonly known as the *tune* [2]:

$$\nu = 2\pi \int_0^C \frac{1}{w^2(s)} ds. \tag{1.17}$$

The one turn matrix at any position s, $M(s)$, is obtained explicitly by multiplying the transfer matrix of each element in the ring and from Eq. 1.16 it is possible to derive the value of the functions $\beta(s)$, $\alpha(s)$ and $\gamma(s)$ (and therefore also $w(s)$ and $w'^{(s)}$) all around the ring:

$$\begin{aligned} \beta(s) &= \frac{M_{12}(s)}{\sin(\nu)}, \\ \alpha(s) &= \frac{M_{11}(s) - M_{22}(s)}{\sin(\nu)}, \\ \gamma(s) &= -\frac{M_{21}(s)}{\sin(\nu)}. \end{aligned} \tag{1.18}$$

[1] According to the definition of the Courant-Snyder parameters, Eq. 1.4 turns into: $u(s) = \sqrt{\beta(s)J}\cos(\psi(s) + \psi_0)$, where the parameter $J = A^2$ is the action, and takes into account for the excitation strength.

[2] A more common definition of the tune is:

$$\nu = \int_0^C \frac{1}{w^2(s)} ds.$$

But in this case we prefer to include the factor 2π in the tune definition in order to simplify the notation

The last step consists in providing the transfer matrices for straight sections and quadrupoles. These are obtained by integrating Eq. 1.3 for a constant value of K. For a straight section ($K = 0$) of length l the transfer matrix assumes the simple form:

$$M = \begin{pmatrix} 1 & l \\ 0 & 1 \end{pmatrix}; \tag{1.19}$$

which, represents the drifting motion of a free particle.

Instead in the case of a quadrupole $K \neq 0$ of length l, a different solution is found depending on the sign of K:

$$M = \begin{cases} \begin{pmatrix} \cos(\sqrt{K}l) & \frac{1}{\sqrt{K}}\sin(\sqrt{K}l) \\ -\sqrt{K}\sin(\sqrt{K}l) & \cos(\sqrt{K}l) \end{pmatrix} & \text{if } K > 0 \\ \begin{pmatrix} \cosh(\sqrt{|K|}l) & \frac{1}{\sqrt{|K|}}\sinh(\sqrt{|K|}l) \\ \sqrt{|K|}\sinh(\sqrt{|K|}l) & \cosh(\sqrt{|K|}l) \end{pmatrix} & \text{if } K < 0. \end{cases} \tag{1.20}$$

A simplified formula is obtained in the case $l << \frac{1}{\sqrt{|K|}}$ (thin lens approximation), in such condition Eq. 1.20 is conventionally approximated as:

$$M = \begin{pmatrix} 1 & 0 \\ -1/f & 1 \end{pmatrix}, \tag{1.21}$$

where the focal length f is:

$$f = \frac{1}{Kl}. \tag{1.22}$$

Figure 1.7 shows an example of the horizontal and vertical beta for the very simple ring introduced in Fig. 1.2, obtained by evaluating Eq. 1.18 along the ring. It is clear how the betatron function reflects the same periodicity of the magnetic lattice as imposed by the Floquet theorem.

The transverse motion of a particle along s is not periodic (Fig. 1.8a). However, the envelope of the trajectories over many turns follows exactly the betatron function. Furthermore, observing turn after turn the particle transverse motion at one

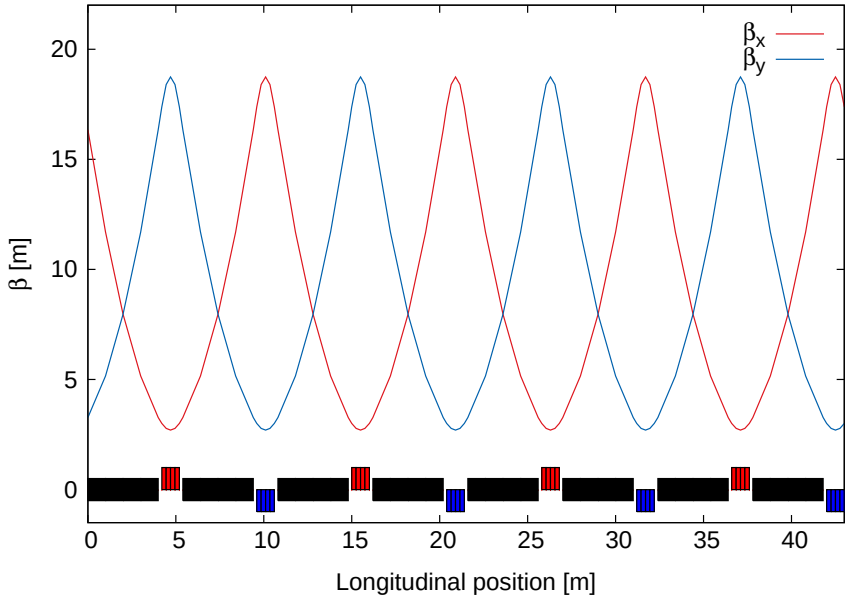

FIGURE 1.7. An example of the horizontal and vertical betatron functions for the simple storage ring introduced in the previous section. Bending magnets are depicted as black rectangles, while red and blue rectangles represent focusing and defocusing quadrupoles respectively.

fixed location of the ring exhibits a perfectly harmonic progression (see Fig. 1.8b) with a frequency equal to the machine tune ν as expected from Eq. 1.4

1.2. Transverse non-linear optics and errors

1.2.1. *Chromatic aberrations and correction*

So far we have limited the design of a storage ring to bending magnets and quadrupoles only. The previous analysis was carried out under the assumption of a well defined particle energy, but if we repeat the linear motion analysis for different particle energies we observe two phenomena:

- Orbit dispersion (Fig. 1.9a): an off energy particle is bent by bending magnets with a different radius, therefore it will describe a different horizontal orbit known as dispersive orbit.

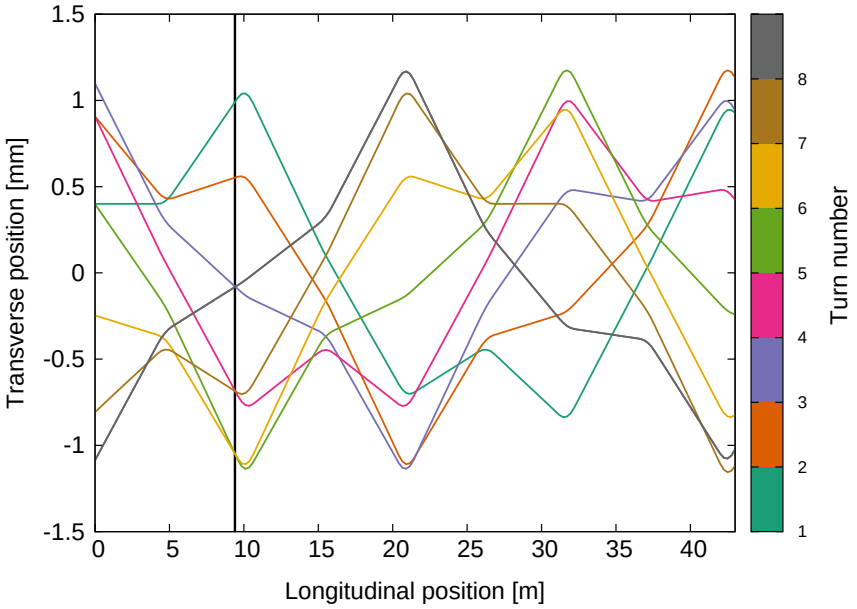

(A) A particle stored in the ring of Fig. 1.6 is kicked horizontally away from the reference orbit. The resulting betatron motion is followed for 8 consecutive turns. Even tough the particle motion does not reflect the periodicity of the magnetic lattice, the trajectory envelope does so and more precisely is proportional to the square root of the betatron function $\beta_x(s)$.

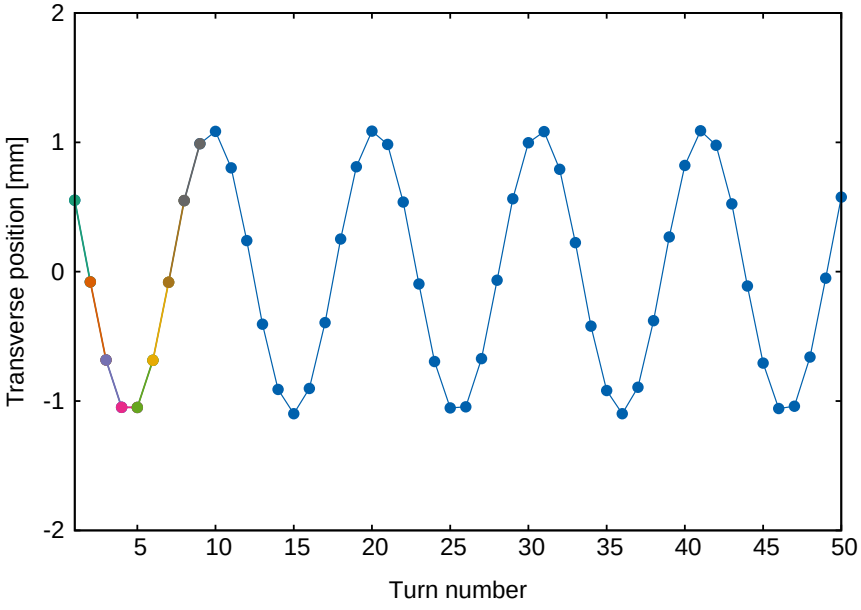

(B) The position of the same particle is now observed at one single location (shown as a black line in the previous picture) for 50 turns. The observed motion is a pure sinusoid with a frequency defined by the betatron tune, $\nu_x = 2\pi \cdot 1.095$ in this example.

FIGURE 1.8

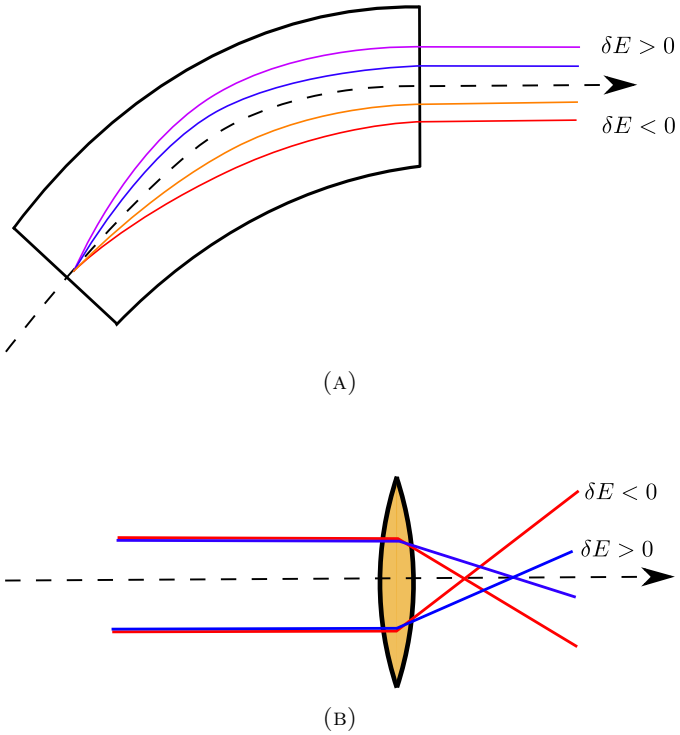

FIGURE 1.9. Magnetic fields get less effective in bending trajectory when dealing with higher energy particles. This leads to: a) *spectrometer effect* when particles with different energy travel across a dipole. b) A chromatic aberration in the case of a quadrupole.

- Chromaticity (Fig. 1.9b): an off energy particle is focused by quadrupole magnets with a different strength resulting in a shift of the betatron tune:

$$\delta\nu = \frac{\delta\nu}{\delta p}\delta p = \frac{\delta\nu}{\delta p/p}\frac{\delta p}{p} = \nu'\frac{\delta p}{p} \tag{1.23}$$

  where $\frac{\delta p}{p}$ represents the relative energy variation and ν' is the chromaticity.

While the first issue does not really affect the ability of the storage ring to store particles, the second one represents an important limiting factor and needs to be addressed.

To correct the natural chromaticity, i.e. the chromaticity produced only by the quadrupoles, we need to introduce in the magnetic lattice new elements. The strategy consists in taking advantage of the energy sorting produced in the transverse plane by the dispersion: particles with different energies lay on different orbits. By

introducing in a location of high dispersion a focusing element whose strength depends on the particle transverse position, it is possible to compensate the different focusing of the quadrupoles.

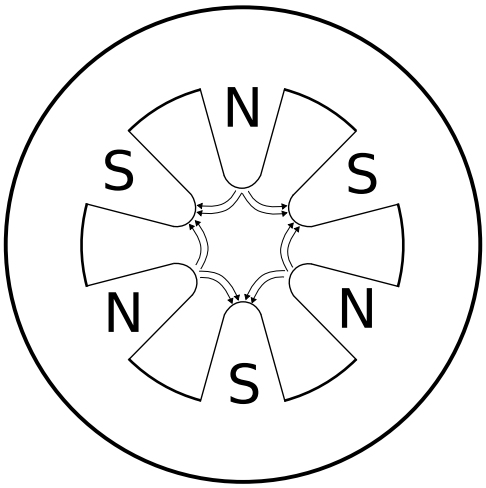

FIGURE 1.10. Transverse cross section of a sextupole magnet. In a sextupole six magnetic poles are arranged in such a way to produce a second order magnetic gradient.

Sextupolar magnets, as the one sketched in Fig. 1.10, produce a field of the kind [**47**]:

$$\begin{cases} B_x &= 2Sxy \\ B_y &= S(x^2 - y^2), \end{cases} \tag{1.24}$$

with S defined as:

$$S = \frac{1}{2}\frac{\partial^2 B_y}{\partial x^2}\Big|_0. \tag{1.25}$$

The quadratic term Sx^2 of Eq. 1.24 results in a focusing or defocusing effect whose strength varies linearly with the transverse position, therefore making the sextupole a solution for chromatic correction. Figure 1.11 shows how a sextupole strategically placed in a location of high dispersion, allows to compensate the chromatic aberration produced by a close quadrupole.

Such approach is used in storage rings where sextupoles placed at locations of high dispersion correct the chromatic aberrations. On the other hand the presence of sextupoles in the magnetic lattice introduces also a new class of problems. First

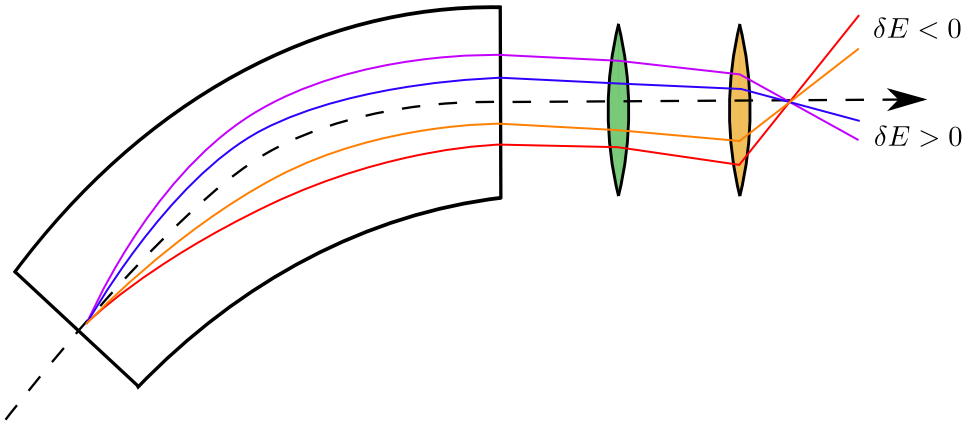

FIGURE 1.11. Schematics of a sextupole (green lens) is placed in a location of high dispersion to compensate for the chromatic aberration produced by a close quadrupole (yellow lens).

of all the equation of motion (Eq. 1.3) becomes non-linear. To further complicate things, the magnetic field from Eq. 1.24 couples the motion in the horizontal and vertical planes: from now on we are not allowed anymore to treat the two planes as two separated problems. Since it is not possible to derive an exact solution for the transverse motion approximated solutions are then to be inferred.

1.2.2. *Perturbation Theory*

In this chapter we introduce the transverse beam dynamics in the presence of non-linear forces and forces that couple the vertical and horizontal motion turning the simple Hill's equation (Eq. 1.3) in a rather complicated system of two coupled non-linear differential equations whose analytic solution is not available.

In fact it is common for such systems to exhibit a chaotic behavior whenever the non-linear contributions grows above a certain threshold, that is the case of particles moving far away from the magnet axis and therefore experiencing strong non-linear forces as the ones produced by sextupoles. Conversely a regular motion is still observed for particles moving close to the magnet axis, where the non-linear components of the fields vanish quickly. In this last case a perturbative approach is an effective way to study the beam dynamics providing an approximated and simple analytical expression for the particle motion.

After having introduced a generic perturbative term $f_{x,y}(x(s), y(s), s)$ that takes into account non-linear and coupling forces, the equation of motion turns

into:

$$\begin{cases} x''(s) + K(s)x(s) = f_x(x(s), y(s), s) \\ y''(s) - K(s)y(s) = f_y(y(s), x(s), s). \end{cases} \tag{1.26}$$

The new non-linear force term can be expressed in a general way with a polynomial expansion of the form:

$$f(x(s), y(s)) = \sum_{m,n} x^m(s) y^n(s) \cdot P_{m,n}(s), \tag{1.27}$$

where the longitudinal position dependent function $P_{m,n}(s)$ represents the non-linear perturbation distribution around the storage ring which, similarly to the function K, has a periodicity defined by the storage ring length. At small amplitude f_x and f_y vanish smoothly, therefore we expect Eq. 1.4 to provide still a good approximation of the transverse motion. We call this solution zero order approximation and we identify it with the subscript 0:

$$\begin{cases} x_0(s) = \sqrt{\beta_x(s) J_x} \cos(\psi_x(s)) \\ y_0(s) = \sqrt{\beta_y(s) J_y} \cos(\psi_y(s)). \end{cases} \tag{1.28}$$

Starting from the zero order approximation we proceed to include the contribution of f_x and f_y by means of a perturbative approach. Whenever $x, y \to 0$, we can replace $x(s)$ and $y(s)$ with $x_0(s)$ and $y_0(s)$ when evaluating the terms f_x and f_y committing a small error.

$$\begin{cases} x_1''(s) + K(s)x_1(s) = f_x(x_0(s), y_0(s), s) \\ y_1''(s) - K(s)y_1(s) = f_y(x_0(s), y_0(s), s). \end{cases} \tag{1.29}$$

The solution of the system of equations 1.29 is called first-order approximation. By evaluating f_x and f_y in the zero order solution we obtain two major effects: the non-linearity in the unknown variables x and y is removed along with coupling. Therefore the problem has been reduced to solving a much simpler couple of inhomogeneous linear differential equations. Once removed the coupling between vertical and horizontal planes we can switch back to consider one single general equation that applies for both planes and only at the end specialize the solution for

the two different cases [3]:

$$u_1''(s) + K(s)u_1(s) = f(u_0(s), s). \tag{1.30}$$

So far the particle motion has been studied in terms of the longitudinal variable s, on the other hand the beam experimental observations are carried out at fixed positions around the storage ring, where beam position monitors (BPMs) are located. Hence it is helpful to introduce a different notation, where the particle position is identified by the variable $r \in [0, C]$ and the turn number is explicitly introduced by the variable n, such that $s = r + nC$.

If multiple sources of error are present, the perturbation term becomes quickly complicated. To simplify our task the superposition principle comes in handy: in fact we can solve Eq. 1.30 for a single delta shaped error source, thereafter obtain the complete solution by performing a convolution over the full distribution of errors.

Because of the periodicity imposed by the storage ring, a single delta shaped perturbation is *perceived* by a particle as a Dirac comb (denoted by the symbol III_C): every time the particle completes a turn and travels through the perturbation it undergoes a kick. Therefore the perturbation term turns into:

$$f_{\mathrm{III}_C}(r, r_\mathrm{p}, n) = \sum_{n=0}^{+\infty} \delta(r - r_\mathrm{p}) u_0^m(r + nC), \tag{1.31}$$

where r_p represents the longitudinal position of the perturbation and the exponent m the perturbation order (1 for quadrupoles, 2 for sextupoles, etc.).

Starting the summation at zero instead of $-\infty$ might seem wrong at first sight. In fact the perturbation is present all time in the storage ring, while Eq. 1.31 represents a perturbation that affects the beam only after turn 0. Such a choice is made to reproduce the experimental condition under which the observations are actually carried out. As will be made clearer in the chapters dedicated to turn-by-turn measurements, the observation of the beam dynamics is only possible as long as a whole bunch of particles moves coherently behaving effectively as one single

[3] Here a simplified notation is used to indicate the perturbing function $f()$ that, instead of depending on both the transverse coordinates it is represented as a function of a single generic coordinate $u_0(s)$. Nevertheless the following discussion is still valid provided that the proper coordinates are substituted when evaluating $f()$.

macro-particle. This condition is experimentally obtained by abruptly displacing on the transverse plane "kicking" a bunch initially on axis and observing how it relaxes while undergoing betatron motion. Since before the excitation the bunch moves on the equilibrium orbit, where the perturbation vanishes, it is correct to assume that no perturbation is present before the bunch gets kicked at turn 0 and moved away from the reference orbit.

To find the solution u_{III_C} associated to the perturbation f_{III_C} we exploit a second time the superposition principle. Following the Green's function method we solve Eq. 1.30 for a non-periodic single delta perturbation located at r_p:

$$u''_\delta(r, r_\mathrm{p}, n) + K(s)u_\delta(r, r_\mathrm{p}, n) = \delta(r - r_\mathrm{p} + nC). \tag{1.32}$$

Therefore u_{III_C} is obtained by adding up the series:

$$u_{\mathrm{III}_C}(r, r_\mathrm{p}, n) = \sum_{t=0}^{\infty} u_\delta(r, r_\mathrm{p}, n - t) \cdot u_0^m(r_\mathrm{p} + tC). \tag{1.33}$$

The dynamics described by Eq. 1.32 is essentially the one of a particle at rest until it crosses r_p where the δ perturbation is located, thereafter undergoes a free betatron motion. An explicit expression for u_δ is obtained by modifying the solution previously found for the homogeneous Hill's equation [4] 1.28 as follows:

$$u_\delta(r, r_\mathrm{p}, n) = \theta(r - r_\mathrm{p} + nC)\sqrt{\beta(r)\beta(r_\mathrm{p})}\sin(\psi(r + nC) - \psi(r_\mathrm{p})), \tag{1.34}$$

where the Heaviside function $\theta(r)$ is defined as:

$$\theta(r) = \int_{-\infty}^{r} \delta(r')dr'. \tag{1.35}$$

Now that a solution for u_δ was found, the last remaining step is adding the series in Eq. 1.33. For this purpose we need to introduce explicitly the term u_0^m. Being such a term dependent on the kind of perturbation, we have to specialize the solution for each different kind of perturbation.

A sketch of the process of adding up the series in order to build the solution is shown in Fig. 1.12. According to Eq. 1.33 the effect of the perturbation is assessed

[4] Note that here the cosine from Eq. 1.28 has been turned into a sinus to match the excitation condition, that has been changed from a transverse displacement, as used in the previous section, to a transverse kick (trajectory angle).

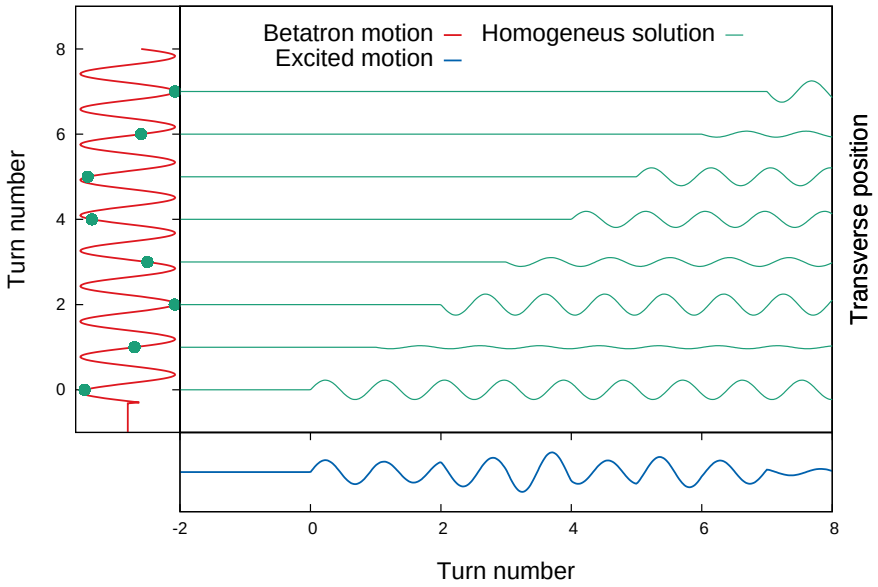

FIGURE 1.12. The overall motion (blue) excited by a perturbation is decomposed in series. Each term (green curves) represents the betatron motion induced by the beam crossing the perturbation at one specific turn. The strength of each excitation (green dots) depends on the beam coordinate $u_0^m(r_\mathrm{p} + nC)$ (red) and therefore varies at each turn. Since before turn 0 the beam is unexcited and sits on the equilibrium orbit there is no need to include in the series any term before turn 0 being identically zero. This condition reflects well the experimental observation where the relaxed beam get abruptly excited by a fast pulsed magnet in less than one turn, thence the system is left to relax again.

by following the particle turn after turn and at each turn including the contribution of the interaction with the perturbation in the form of a free betatron oscillation.

In the next paragraphs we will analyze two different cases: rotated quadrupoles, known as skew quadrupoles, that couple the horizontal and vertical motion, and sextupoles.

1.2.3. *Skew Quadrupoles*

The force produced by a skew quadrupole on one plane is proportional to the particle displacement in the other plane, therefore coupling the horizontal and vertical motion. An explicit expression of the magnetic field produced by a skew

quadrupole is:

$$\begin{cases} B_y = Gy \\ B_x = -Gx, \end{cases} \tag{1.36}$$

with $G = \frac{\partial B_x}{\partial x}\big|_0$.

For simplicity's sake we solve the problem for the horizontal plane only, since the effect is symmetrical the complementary solution for the vertical plane can be subsequently derived by simply swapping the indexes x and y.

The horizontal motion is therefore obtained from Eq. 1.33 by replacing u_δ with x_δ and substituting the zero order solution for the vertical motion in the place of u^m:

$$\begin{aligned} x_{\mathrm{III}_C}(r, r_\mathrm{p}, n) = \sum_{t=0}^{\infty} x_\delta(r, r_\mathrm{p}, n-t) \cdot y_0(r_\mathrm{p} + tC) = \\ \sum_{t=0}^{\infty} \theta(r + (n-t)C - r_\mathrm{p}) \sqrt{\beta_x^\mathrm{o} \beta_x^\mathrm{p}} \sin(\Delta\psi_x + (n-t)\nu_x) \times \\ \sqrt{\beta_y^\mathrm{p} J_y} \sin(\psi_y^\mathrm{p} + t\nu_y), \end{aligned} \tag{1.37}$$

where $\Delta\psi = \psi(r) - \psi(r_\mathrm{p})$ represents the phase advance between the observation point r and the location of the perturbation r_p. The superscripts o and p identify respectively a variable evaluated at the observation point r or at the location of the perturbation r_p (such that $\beta_x^\mathrm{p} = \beta_x(r_\mathrm{p})$ and $\beta_x^\mathrm{o} = \beta_x(r)$).

The operator $\theta(r)$ is removed by restricting the upper limit of the sum to n:

$$x_{\mathrm{III}_C}(r, r_\mathrm{p}, n) = \sum_{t=0}^{n} \sqrt{\beta_x^\mathrm{o} \beta_x^\mathrm{p} \beta_y^\mathrm{p} J_y} \sin(\Delta\psi_x + (n-t)\nu_x) \cdot \sin(\psi_y^\mathrm{p} + t\nu_y), \tag{1.38}$$

that is rewritten as:

$$\begin{aligned} x_{\mathrm{III}_C}(r, r_\mathrm{p}, n) = \frac{\sqrt{\beta_x^\mathrm{o} \beta_x^\mathrm{p} \beta_y^\mathrm{p} J_y}}{4} \left\{ \left[e^{-in\nu_x} e^{i(\psi_y^\mathrm{p} - \Delta\psi_x)} \sum_{t=0}^{n} e^{it(\nu_y + \nu_x)} + c.c. \right] \right. \\ \left. - \left[e^{in\nu_x} e^{i(\psi_y^\mathrm{p} + \Delta\psi_x)} \sum_{t=0}^{n} e^{it(\nu_y - \nu_x)} + c.c. \right] \right\}. \end{aligned} \tag{1.39}$$

The sum has been reduced to a geometric series, therefore we can proceed to add up all the terms by means of the identity:

$$\sum_{t=0}^{n} e^{it\nu} = \frac{1 - e^{i(n+1)\nu}}{1 - e^{i\nu}}. \tag{1.40}$$

After some manipulation the horizontal beam motion $x_{\mathrm{III}_C}(r, r_\mathrm{p}, n)$ is decomposed as the sum of two modes:

$$x_{\mathrm{III}_C}(r, r_\mathrm{p}, n) = \mathrm{H}_{\mathrm{III}_C}(1,0) + \mathrm{H}_{\mathrm{III}_C}(0,1), \tag{1.41}$$

where, following the notation from [**21**], H(n, m) represents a horizontal mode with frequency $n\nu_x + m\nu_y$. The two modes can be written as:

$$\mathrm{H}_{\mathrm{III}_C}(0,1) = \tag{1.42}$$
$$\frac{\sqrt{\beta_x^\mathrm{o}\beta_x^\mathrm{p}\beta_y^\mathrm{o}J_y}}{4}\left[\frac{e^{i(\psi_y^\mathrm{p}+\Delta\psi_x)}}{e^{-i(\nu_y-\nu_x)}-1} - \frac{e^{i(\psi_y^\mathrm{p}-\Delta\psi_x)}}{e^{-i(\nu_y+\nu_x)}-1}\right] e^{i\nu_y n} + \text{c.c.},$$

and

$$\mathrm{H}_{\mathrm{III}_C}(1,0) = \tag{1.43}$$
$$\frac{\sqrt{\beta_x^\mathrm{o}\beta_x^\mathrm{p}\beta_y^\mathrm{o}J_y}}{4}\left[\frac{e^{-i(\psi_y^\mathrm{p}-\Delta\psi_x-\nu_x-\nu_y)}}{e^{i(\nu_y+\nu_x)}-1} - \frac{e^{i(\psi_y^\mathrm{p}+\Delta\psi_x+\nu_x-\nu_y)}}{e^{i(\nu_x-\nu_y)}-1}\right] e^{i\nu_x n} + \text{c.c.}.$$

While Eq. 1.41 provides the first-order correction to the horizontal betatron motion due to the presence of a single delta shaped skew quadrupole, the overall correction is obtained by integrating the skew quadrupole distribution $P(r_\mathrm{p})$ in the storage ring:

$$x(r,n) = \mathrm{H}(1,0) + \mathrm{H}(0,1) = \int_0^C x_{\mathrm{III}_C}(r, r_\mathrm{p}, n) P(r_\mathrm{p}) dr_\mathrm{p}. \tag{1.44}$$

In conclusion a pulsed excitation[5] of the vertical betatron motion propagates to the horizontal plane through skew quadrupoles, resulting in turn in the excitation of the two horizontal modes: H(1,0) and H(0,1), whose amplitudes and phases

[5] The presence of the mode H(1,0) is to be attributed to the intrinsically wide spectrum excitation of the pinger magnet kick, where instead a "slow" excitation process such as the one provided by a radio frequency stripline, would strongly suppress the excitation of such mode. In the case of a slow excitation the vertical betatron motion amplitude (action) grows over many turns, as shown in the following figure:

are functions of the observer position (BPM location) and the skew quadrupole distribution.

From an experimental stand point, in order to obtain a clean picture of the contribution of the skew quadrupoles to the spectral line H(1,0), any direct excitation of the horizontal betatron motion has to be avoided. This condition is very hard to meet, requiring an extremely good alignment of the pinger magnet used to excite the vertical betatron motion. For this reason only the mode H(0,1) has been taken into account in the experimental coupling characterization carried out in Chapter 7.

Exploiting the symmetry of the problem, the analogous vertical motion correction is then obtained by swapping the x and y indexes:

$$y_{\mathrm{III}_C}(r, r_\mathrm{p}, n) = \mathrm{V}_{\mathrm{III}_C}(0,1) + \mathrm{V}_{\mathrm{III}_C}(1,0), \tag{1.47}$$

with:

$$\mathrm{V}_{\mathrm{III}_C}(1,0) = \frac{\sqrt{\beta_y^\mathrm{o}\beta_y^\mathrm{p}\beta_x^\mathrm{o}J_x}}{4}\left[\frac{e^{i(\psi_x^\mathrm{p}+\Delta\psi_y)}}{e^{-i(\nu_x-\nu_y)}-1} - \frac{e^{i(\psi_x^\mathrm{p}-\Delta\psi_y)}}{e^{-i(\nu_x+\nu_y)}-1}\right] e^{i\nu_x n} + \text{c.c.}, \tag{1.48}$$

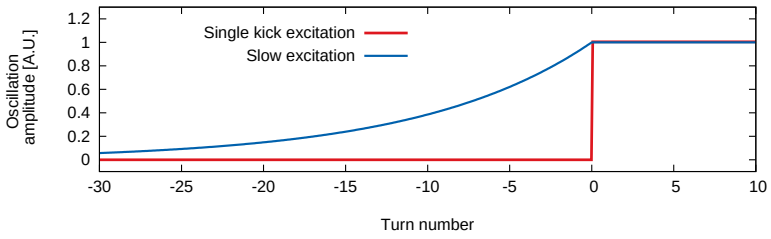

To take into account the slow excitation, Eq. 1.37 is modified by adding a "lead in" term:

$$x_{\mathrm{III}_C}(r, r_\mathrm{p}, n) = \sum_{t=-\infty}^{-1} a^t \cdot x_\delta(r, r_\mathrm{p}, n-t) \cdot y_0(r_\mathrm{p} + tC) + \sum_{t=0}^{\infty} x_\delta(r, r_\mathrm{p}, n-t) \cdot y_0(r_\mathrm{p} + tC), \tag{1.45}$$

where the parameter $a > 1$ defines the betatron motion amplitude growth rate. The change is propagated to the next equations and in order to compute the new term in the series we use the identity:

$$\sum_{t=-\infty}^{-1} (ae^{i\nu})^t = \lim_{n\to-\infty} \frac{(ae^{i\nu})^n - 1}{1 - ae^{i\nu}} = \frac{-1}{1-ae^{i\nu}}. \tag{1.46}$$

By adding up the series we find that as the excitation time tends to infinity ($a \to 1^+$), a complete suppression of the mode H(1,0) is observed, while not affecting the mode H(0,1).

and

$$\mathrm{V}_{\mathrm{III}_C}(0,1) = \tag{1.49}$$
$$\frac{\sqrt{\beta_y^{\mathrm{o}}\beta_y^{\mathrm{p}}\beta_x^{\mathrm{o}}J_x}}{4}\left[\frac{e^{-i(\psi_x^{\mathrm{p}}-\Delta\psi_y-\nu_y-\nu_x)}}{e^{i(\nu_x+\nu_y)}-1} - \frac{e^{i(\psi_x^{\mathrm{p}}+\Delta\psi_y+\nu_y-\nu_x)}}{e^{i(\nu_y-\nu_x)}-1}\right]e^{i\nu_y n} + \text{c.c.}.$$

Not surprisingly, because of the symmetry of the problem, the results is analogous to what observed in the horizontal plane.

1.2.4. *Sextupoles*

The approach we follow for the sextupolar perturbation is no way different from the skew quadrupole case, the only change we need to apply is in the definition of the force. This time since the effect on the vertical and horizontal plane is different, we need to deal with the two cases separately.

In the horizontal plane the perturbative force is proportional to $x^2 - y^2$. Therefore Eq. 1.33 turns into:

$$\begin{aligned} x_{\mathrm{III}_C}(r, r_{\mathrm{p}}, n) &= \sum_{t=0}^{\infty} x_\delta(r, r_{\mathrm{p}}, n-t)\cdot\left[x_0^2(r_{\mathrm{p}}+tC) - y_0^2(r_{\mathrm{p}}+tC)\right] = \\ &\sum_{t=0}^{\infty}\theta(r+(n-t)C-r_{\mathrm{p}})\sqrt{\beta_x^{\mathrm{o}}\beta_x^{\mathrm{p}}}\sin(\Delta\psi_x+(n-t)\nu_x) \\ &\left[\beta_x^{\mathrm{p}}J_x\sin^2(\psi_x^{\mathrm{p}}+t\nu_x) - \beta_y^{\mathrm{p}}J_y\sin^2(\psi_y^{\mathrm{p}}+t\nu_y)\right], \end{aligned} \tag{1.50}$$

where the same notation as in the case of the skew quadrupole applies. Rewriting the squared sine terms by making use of the identity $\sin^2(\alpha) = \frac{1}{2}[1-\cos(2\alpha)]$, an expression very similar to the previous case of the skew quadrupole is obtained. After adding up the series and performing some minor manipulation the correctrion the horizontal beam motion is decomposed as the sum of four modes:

$$x_{\mathrm{III}_C}(r, r_{\mathrm{p}}, n) = \mathrm{H}_{\mathrm{III}_C}(2,0) + \mathrm{H}_{\mathrm{III}_C}(0,2) + \mathrm{H}_{\mathrm{III}_C}(1,0) + \mathrm{H}_{\mathrm{III}_C}(0,0), \tag{1.51}$$

with:

$$\mathrm{H}_{\mathrm{III}_C}(0,2) = \frac{\beta_y^{\mathrm{p}} J_y \sqrt{\beta_x^{\mathrm{o}}\beta_x^{\mathrm{p}}}}{8i} \cdot \left[\frac{e^{i(2\nu_y+\nu_x-\Delta\psi_x+2\psi_y^{\mathrm{p}})}}{e^{i(2\nu_y+\nu_x)}-1} - \frac{e^{i(2\nu_y-\nu_x+\Delta\psi_x+2\psi_y^{\mathrm{p}})}}{e^{i(2\nu_y-\nu_x)}-1} \right] e^{2i\nu_y n} - \text{c.c.}, \tag{1.52}$$

$$\mathrm{H}_{\mathrm{III}_C}(2,0) = \frac{\beta_x^{\mathrm{p}} J_x \sqrt{\beta_x^{\mathrm{o}}\beta_x^{\mathrm{p}}}}{8i} \cdot \left[\frac{e^{i(3\nu_x-\Delta\psi_x+2\psi_x^{\mathrm{p}})}}{e^{3i\nu_x}-1} - \frac{e^{i(\nu_x+\Delta\psi_x+2\psi_x^{\mathrm{p}})}}{e^{i\nu_x}-1} \right] e^{2i\nu_x n} - \text{c.c.}, \tag{1.53}$$

$$\begin{aligned}\mathrm{H}_{\mathrm{III}_C}(1,0) = &\frac{\beta_y^{\mathrm{p}} J_y \sqrt{\beta_x^{\mathrm{o}}\beta_x^{\mathrm{p}}}}{8i} \cdot \left[\frac{e^{i(\Delta\psi_x+2\psi_y^{\mathrm{p}})}}{e^{i(2\nu_y-\nu_x)}-1} + \frac{e^{i(\Delta\psi_x-2\psi_y^{\mathrm{p}})}}{e^{-i(2\nu_y+\nu_x)}-1} - \frac{2e^{i(\Delta\psi_x)}}{e^{-i\nu_x}-1} \right] e^{i\nu_x n} + \\ &\frac{\beta_x^{\mathrm{p}} J_x \sqrt{\beta_x^{\mathrm{o}}\beta_x^{\mathrm{p}}}}{8i} \cdot \left[\frac{e^{i(\Delta\psi_x+2\psi_x^{\mathrm{p}})}}{e^{i\nu_x}-1} + \frac{e^{i(\Delta\psi_x-2\psi_x^{\mathrm{p}})}}{e^{-3i\nu_x}-1} - \frac{2e^{i(\Delta\psi_x)}}{e^{-i\nu_x}-1} \right] e^{i\nu_x n} - \text{c.c.},\end{aligned} \tag{1.54}$$

and

$$\mathrm{H}_{\mathrm{III}_C}(0,0) = \frac{\beta_y^{\mathrm{p}} J_y \sqrt{\beta_x^{\mathrm{o}}\beta_x^{\mathrm{p}}}}{4i} \cdot \frac{e^{i(\Delta\psi_x-\nu_x)}}{e^{-i\nu_x}-1} + \frac{\beta_x^{\mathrm{p}} J_x \sqrt{\beta_x^{\mathrm{o}}\beta_x^{\mathrm{p}}}}{4i} \cdot \frac{e^{i(\Delta\psi_x-\nu_x)}}{e^{-i\nu_x}-1} - \text{c.c.}. \tag{1.55}$$

The overall correction is then obtained by integrating over the sextupole distribution $P(r_{\mathrm{p}})$ in the storage ring:

$$\begin{aligned} x(r,n) &= \mathrm{H}(2,0) + \mathrm{H}(0,2) + \mathrm{H}(1,0) + \mathrm{H}(0,0) \\ &= \int_0^C x_{\mathrm{III}_C}(r, r_{\mathrm{p}}, n) P(r_{\mathrm{p}}) dr_{\mathrm{p}}. \end{aligned} \tag{1.56}$$

Of the four modes, H(2,0) and H(0,2) have the well recognizable frequency of two times the horizontal and two times the vertical tune respectively, providing good candidates for experimental studies since they do not overlap with any other line of the spectrum. H(1,0) instead will not be used for the same reason discussed in the previous case about the skew quadrupole, while the zero frequency mode (orbit offset) H(0,0) also will not be used because of limitations in the ALBA

experimental setup that prevented to obtain a reliable orbit measurements when acquiring turn-by-turn data.

The last missing step is to calculate the effect produced on the vertical plane. In this case the force is proportional to two times the product of the horizontal and vertical displacements $2xy$, turning Eq. 1.33 into:

$$y_{\mathrm{III}_C}(r, r_\mathrm{p}, n) = \sum_{t=0}^{\infty} \theta(r + (n-t)C - r_\mathrm{p}) \sqrt{\beta_y^\mathrm{o} \beta_y^\mathrm{p}} \sin(\Delta\psi_y + (n-t)\nu_y) \cdot 2\sqrt{\beta_x^\mathrm{p} J_x \beta_y^\mathrm{p} J_y} \sin(\psi_x^\mathrm{p}) + t\nu_x) \sin(\psi_y^\mathrm{p}) + t\nu_y). \tag{1.57}$$

Proceeding as before we find the following expression for the first-order correction to the vertical betatron motion:

$$y_{\mathrm{III}_C}(r, r_\mathrm{p}, n) = \mathrm{V}_{\mathrm{III}_C}(1,1) + \mathrm{V}_{\mathrm{III}_C}(1,-1) + \mathrm{V}_{\mathrm{III}_C}(0,1), \tag{1.58}$$

with:

$$\mathrm{V}_{\mathrm{III}_C}(1,1) = \frac{\beta_y^\mathrm{p} \sqrt{\beta_x^\mathrm{p} \beta_y^\mathrm{o} J_x J_y}}{4i} e^{\psi_x^\mathrm{p} + \psi_y^\mathrm{p} + \nu_x} \cdot \left[\frac{e^{i(2\nu_y - \Delta\psi_y)}}{e^{i(\nu_x + 2\nu_y)} - 1} - \frac{e^{i\Delta\psi_y}}{e^{i\nu_x} - 1} \right] \cdot e^{i(\nu_x + \nu_y)n} - \text{c.c.} \tag{1.59}$$

$$\mathrm{V}_{\mathrm{III}_C}(1,-1) = \frac{\beta_y^\mathrm{p} \sqrt{\beta_x^\mathrm{p} \beta_y^\mathrm{o} J_x J_y}}{4i} e^{\psi_x^\mathrm{p} - \psi_y^\mathrm{p} + \nu_x} \cdot \left[\frac{e^{i(\Delta\psi_y - 2\nu_y)}}{e^{i(\nu_x - 2\nu_y)} - 1} - \frac{e^{-i\Delta\psi_y}}{e^{i\nu_x} - 1} \right] \cdot e^{i(\nu_x - \nu_y)n} - \text{c.c.} \tag{1.60}$$

$$\mathrm{V}_{\mathrm{III}_C}(0,1) = \frac{\beta_y^\mathrm{p} \sqrt{\beta_x^\mathrm{p} \beta_y^\mathrm{o} J_x J_y}}{4i} \cdot \left[\frac{e^{i(\Delta\psi_y + \psi_x^\mathrm{p} + \psi_y^\mathrm{p})}}{e^{i\nu_x} - 1} + \frac{e^{i(\Delta\psi_y - \psi_x^\mathrm{p} - \psi_y^\mathrm{p})}}{e^{-i(\nu_x + 2\nu_y)} - 1} + - \frac{e^{i(\Delta\psi_y + \psi_x^\mathrm{p} - \psi_y^\mathrm{p})}}{e^{i(\nu_x - 2\nu_y)} - 1} - \frac{e^{i(\Delta\psi_y - \psi_x^\mathrm{p} + \psi_y^\mathrm{p})}}{e^{-i\nu_x} - 1} \right] e^{i\nu_y n}. \tag{1.61}$$

Also this time we observe a behavior similar to the previous cases: the correction is composed by several terms some of which overlap with the betatron

TABLE 1.1. Observables obtained by combining the spectral lines relative to perturbations and the tune lines in order to remove the dependency on the initial motion condition.

Skew quadrupole	
$F_{xy} = \lvert F_{xy}\rvert e^{iq_{F_{xy}}}$	$\begin{cases} \lvert F_{xy}\rvert = \lvert H(0,1)/[2\lvert V(0,1)\rvert] \\ q_{F_{xy}} = \psi_{H(0,1)} - \psi_{V(0,1)} - \frac{3}{2}\pi \end{cases}$
$F_{yx} = \lvert F_{yx}\rvert e^{iq_{F_{yx}}}$	$\begin{cases} \lvert F_{yx}\rvert = \lvert V(1,0)/[2\lvert H(1,0)\rvert] \\ q_{F_{yx}} = \psi_{V(1,0)} - \psi_{H(1,0)} - \frac{3}{2}\pi \end{cases}$
Sextupole	
$F_{NS3} = \lvert F_{NS3}\rvert e^{iq_{F_{NS3}}}$	$\begin{cases} \lvert F_{NS3}\rvert = \lvert H(-2,0)/[4\lvert H(1,0)\rvert^2] \\ q_{F_{NS3}} = \psi_{H(-2,0)} - \psi_{H(1,0)} + \frac{3}{2}\pi \end{cases}$
$F_{NS2} = \lvert F_{NS2}\rvert e^{iq_{F_{NS2}}}$	$\begin{cases} \lvert F_{NS2}\rvert = \lvert H(0,-2)/[4\lvert H(0,1)\rvert^2] \\ q_{F_{NS2}} = \psi_{H(0,-2)} - \psi_{H(0,1)} + \frac{3}{2}\pi \end{cases}$
$F_{NS1} = \lvert F_{NS1}\rvert e^{iq_{F_{NS1}}}$	$\begin{cases} \lvert F_{NS1}\rvert = \lvert V(-1,-1)/[4\lvert H(1,0)\rvert\lvert V(0,1)\rvert] \\ q_{F_{NS1}} = \psi_{V(-1,-1)} + \psi_{H(1,0)} + \psi_{V(0,1)} - \frac{3}{2}\pi \end{cases}$
$F_{NS0} = \lvert F_{NS0}\rvert e^{iq_{F_{NS0}}}$	$\begin{cases} \lvert F_{NS1}\rvert = \lvert V(1,-1)/[4\lvert H(1,0)\rvert\lvert V(0,1)\rvert] \\ q_{F_{NS1}} = \psi_{V(1,-1)} - \psi_{H(1,0)} + \psi_{V(0,1)} - \frac{3}{2}\pi \end{cases}$

oscillation frequency, while the others have instead a frequency that is characteristic of the field produced by a sextupolar magnet and can be used to characterize the sextupoles in the magnetic lattice.

The previous analysis shows how the contribution of each non-linear lattice element is associated to a perturbation of the betatron motion characterized by a well defined resonance mode. Given a turn-by-turn observation of the beam transverse motion in a storage ring, the uniqueness of such frequencies allows to isolate and study the contribution of the different magnetic components. On the other hand the perturbations depend not only on the lattice, but also on the initial motion condition (excitation amplitude and initial phase [6]). Following the approach

[6]In the previous calculation the betatron motion initial phase has been assumed to be $\psi_0 = 0$ that coincides with exciting the beam at $n = 0, r = 0$. Whenever this condition is not met the solution can be obtained by shifting the reference frame along s in order to restore the condition $\psi_0 = 0$. The overall effect on the solution is therefore a phase shift equal to ψ_0.

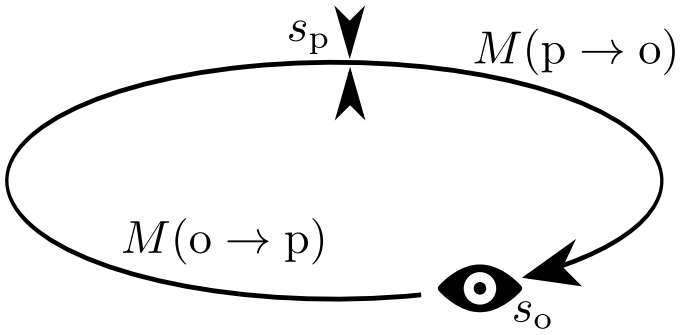

FIGURE 1.13. A small perturbation is located at S_p producing some distortion of the storage ring optical functions everywhere along the ring, including at S_o where an hypothetical observer is located.

proposed in [**21**] we get rid of these unknown quantities by properly "normalizing" the spectral lines with respect to the tune lines, obtaining a new set of observable quantities (Tab. 1.1). This technique requires to sample the linear betatron motion through the observation of the tune lines H(1,0) and V(0,1), on the other hand, as shown previously, such lines are affected in small part by the same skew quadrupoles and sextupoles. However since the correction to those lines is always limited to a negligible fraction (below 1‰ of the overall motion), it is safe to apply the method.

1.2.5. *Small quadrupolar error*

In the previous section a general procedure to evaluate the linear lattice parameters (i.e. $\beta(s)$, $\alpha(s)$ and $\gamma(s)$ functions) in a storage ring was provided. Such procedure required a rather intricate integration process where the effect of every single optical element was concatenated. On the other hand one of the most common and important issue in storage ring is represented by the presence of gradient errors, that could arise either from gradient errors produced by quadrupole magnets, i.e. mechanical errors or power supply inaccuracy, or as the result of more subtle effects as in the case of electromagnetic interaction between the beam and the metallic vacuum chamber (a more detailed description of this phenomenum will be presented in Chapter 8). Therefore in this section we aim at finding a simple way to estimate the optical distortion produced by a generic small gradient perturbation, avoiding the complete and time consuming calculation of the optical functions.

Figure 1.13 outlines the case under study: a single small perturbation is located in the storage ring at position s_p producing an alteration of the optical functions at the position s_o where an hypothetical observer is placed. Being small, the perturbation is accurately represented by the thin lens approximation provided by Eq. 1.21. If $M(\mathrm{o} \to \mathrm{p})$ and $M(\mathrm{p} \to \mathrm{o})$ represent the transfer matrices from the observer to the perturbation location and from the perturbation location to the observer, we can write the overall one turn matrix in presence of the perturbation as:

$$\bar{M} = M(\mathrm{p} \to \mathrm{o})\mathrm{M_e}\mathrm{M}(\mathrm{o} \to \mathrm{p}), \tag{1.62}$$

where M_p is the transfer matrix of the thin lens approximation of the perturbation.

Exploiting relations in Eq. 1.18 it is now possible to calculate the new values of the optical functions. Among them, a quantity of great interest is the relative variation of the $\beta(s)$ function, usually referred as the *β-beating*, that can be calculated from the matrix element $\bar{M}_{12}$:

$$\bar{M}_{12} = -Kl\beta_\mathrm{p}\beta_\mathrm{o}\sin(\psi_\mathrm{p} - \psi_\mathrm{o})\sin(\nu + \psi_\mathrm{o} - \psi_\mathrm{p}) + \beta_\mathrm{o}\sin(\psi_\mathrm{o}), \tag{1.63}$$

where K and l represent respectively the strength and length of the perturbation and the tune ν has been approximated with the tune ν of the lattice free of perturbations.

Substituting Eq. 1.63 in Eq. 1.18 provides an expression of the β-beat produced by a single small gradient error:

$$\frac{\Delta\beta_\mathrm{o}}{\beta_\mathrm{o}} = -\frac{Kl\beta_\mathrm{p}\cos(\nu_0 + \psi_\mathrm{o} - \psi_\mathrm{p})}{2\sin(\nu_0)}. \tag{1.64}$$

The tune shift is obtained by operating in a similar way, this time the new one turn transfer matrix is written as:

$$\bar{M} = MM_p, \tag{1.65}$$

where the matrix M represents the unperturbed one turn transfer matrix. Using Eq. 1.15 the tune is written as:

$$\cos(\bar{\nu}) = \bar{M}_{11} + \bar{M}_{22}. \tag{1.66}$$

Therefore the tune variation $\Delta\nu$ is obtained:

$$\Delta\nu \simeq \cos(\bar{\nu}) - \cos(\nu) = -\frac{1}{2}\beta_p K l. \tag{1.67}$$

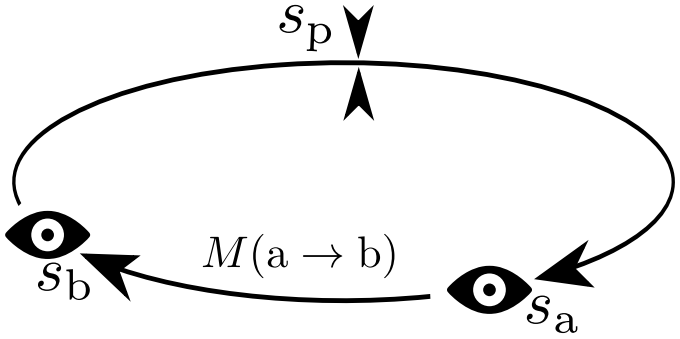

FIGURE 1.14. A small perturbation is located at S_p distorting the phase advance between the positions a and b. In this particular case the perturbation not located between the two points, the special case of an error included in between the two considered points needs to be treated separately.

A similar approach applies also to the calculation of the phase-advance change ("phase-beat") between two locations. A schematic view of the problem is given in Fig. 1.14. For an unperturbed ring the transfer matrix element $M_{12}(\mathrm{a} \to \mathrm{b})$ between two generic points a and b, is:

$$M_{12}(\mathrm{a} \to \mathrm{b}) = \sqrt{\beta_{\mathrm{a}}\beta_{\mathrm{b}}}\sin(\psi_{\mathrm{b}} - \psi_{\mathrm{a}}). \tag{1.68}$$

Since the transfer matrix is defined only by the elements in between the points a and b, the matrix element M_{12} will be equal to the perturbed transfer matrix element $\bar{M}_{12}$, except where the perturbation is located in between the two points (such a case will be covered separately). Expanding the condition $M_{12} = \bar{M}_{12}$ with Eq. 1.68 yields:

$$\begin{aligned} \sin(\bar{\psi}_{\mathrm{b}} - \bar{\psi}_{\mathrm{a}}) = \frac{\sqrt{\beta_{\mathrm{a}}\beta_{\mathrm{b}}}}{\sqrt{\bar{\beta}_{\mathrm{a}}\bar{\beta}_{\mathrm{b}}}}\sin(\psi_{\mathrm{b}} - \psi_{\mathrm{p}}) = \\ \frac{\sqrt{\beta_{\mathrm{a}}\beta_{\mathrm{b}}}}{\sqrt{(\beta_{\mathrm{a}} + \Delta\beta_{\mathrm{a}})(\beta_{\mathrm{b}} + \Delta\beta_{\mathrm{b}})}}\sin(\psi_{\mathrm{b}} - \psi_{\mathrm{a}}), \end{aligned} \tag{1.69}$$

where the perturbed β values have been expanded as the unperturbed ones plus a small variation according to the previous definition of beta-beating. Neglecting the second order term $\Delta\beta_a\Delta\beta_b$ and expanding in a Taylor series truncated to the

first-order yields:

$$\sin(\bar{\psi}_{\mathrm{b}} - \bar{\psi}_{\mathrm{a}}) - \sin(\psi_{\mathrm{b}} - \psi_{\mathrm{a}}) = -\frac{1}{2}\left(\frac{\Delta\beta_{\mathrm{a}}}{\beta_{\mathrm{a}}} + \frac{\Delta\beta_{\mathrm{b}}}{\beta_{\mathrm{b}}}\right)\sin(\psi_{\mathrm{b}} - \psi_{\mathrm{a}}). \tag{1.70}$$

Finally, expanding up to the first-order the left hand side and after some minor manipulations, an expression for the phase-beat $(\Delta\psi_{\mathrm{b}} - \Delta\psi_{\mathrm{a}})$ in the case of a perturbation not included in between the two points a and b is obtained:

$$(\Delta\psi_{\mathrm{b}} - \Delta\psi_{\mathrm{a}})^{\mathrm{p}\notin[\mathrm{a,b}]} = -\frac{1}{2}\left(\frac{\Delta\beta_{\mathrm{a}}}{\beta_{\mathrm{a}}} + \frac{\Delta\beta_{\mathrm{b}}}{\beta_{\mathrm{b}}}\right)\tan(\psi_{\mathrm{b}} - \psi_{\mathrm{a}}), \tag{1.71}$$

where the beta-beat $\frac{\Delta\beta_{\mathrm{a}}}{\beta_{\mathrm{a}}}$ and $\frac{\Delta\beta_{\mathrm{b}}}{\beta_{\mathrm{b}}}$ can be evaluated from Eq. 1.64.

The previous approach holds also in the case of a perturbation located in between the two positions a and b with the exception that now we need to include the additional phase advance ψ_{p} provided by the perturbation itself:

$$(\Delta\psi_{\mathrm{b}} - \Delta\psi_{\mathrm{a}})^{\mathrm{p}\in[\mathrm{a,b}]} = (\Delta\psi_{\mathrm{b}} - \Delta\psi_{\mathrm{a}})^{\mathrm{p}\notin[\mathrm{a,b}]} + \psi_{\mathrm{p}}. \tag{1.72}$$

To evaluate ψ_{p} it is useful to consider the limit case of a=0 and b=L, where the whole storage ring except the perturbation is included in between. Since the phase-advance of the whole ring is by definition the tune, the observed phase-beat coincides with the overall tune-shift $\Delta\nu$ from Eq. 1.67. Therefore ψ_{p} is written as:

$$\psi_{\mathrm{p}} = \Delta\nu - (\Delta\psi_{\mathrm{L}} - \Delta\psi_{0})^{\mathrm{p}\notin[0,\mathrm{L}]}, \tag{1.73}$$

that can be evaluated by means of Eq. 1.71 providing:

$$\psi_{\mathrm{p}} = \Delta\nu - 2\Delta\nu = -\Delta\nu. \tag{1.74}$$

In presence of multiple perturbation sources, or sources with finite length it is possible to estimate the cumulative effect by integrating the previous expressions for the beta-beat, tune-shift and phase-beat over the perturbation distribution:

$$\frac{\Delta\beta_{\mathrm{o}}}{\beta_{\mathrm{o}}} = -\frac{1}{2\sin(\nu_0)}\int_0^C \beta(s)K(s)\cos(\nu_0 + \psi_{\mathrm{o}} - \psi_{\mathrm{p}})ds, \tag{1.75}$$

$$\Delta\nu \simeq -\frac{1}{2}\int_0^C \beta(s)K(s)ds, \tag{1.76}$$

(1.77)

$$\Delta\psi_{\rm b} - \Delta\psi_{\rm a} = \begin{cases} -\frac{1}{2}\int_0^C \left(\frac{\Delta\beta_{\rm a}}{\beta_{\rm a}} + \frac{\Delta\beta_{\rm b}}{\beta_{\rm b}}\right)\tan(\psi_{\rm b} - \psi_{\rm a})K(s)ds & \text{if } s_{\rm p} \notin [s_{\rm a}, s_{\rm b}] \\ -\frac{1}{2}\int_0^C \left(\frac{\Delta\beta_{\rm a}}{\beta_{\rm a}} + \frac{\Delta\beta_{\rm b}}{\beta_{\rm b}}\right)\tan(\psi_{\rm b} - \psi_{\rm a})K(s)ds - \Delta\nu & \text{if } s_{\rm p} \in [s_{\rm a}, s_{\rm b}]. \end{cases}$$

Despite the carefully construction, calibration and alignment of magnets, the tight requirements over the lattice parameters necessary to operate a third generation light source can be hardly met without a beam based measurement and correction process, where the properties of the stored beam are measured and used to extrapolate and correct the optics parameters. The ability to quickly and precisely measure the lattice parameters represents therefore a key tool in this context. In the next chapters we will show how turn-by-turn beam position measurements can be used to extrapolate the parameters described by the theory introduced in this chapter.

CHAPTER 2

The ALBA and SOLEIL storage ring lattices

In the previous chapter the basics of the transverse beam dynamics of a storage ring has been covered introduced. Here the lattices of the two cases under study, ALBA and SOLEIL, are described specifically.

In the next sections an overview of the optics of the two machines is presented focusing mainly on the ALBA storage ring, where most of the work has been carried out.

Furthermore the ALBA lattice is used as a bench test to carry out a comparison between the first-order approximated analytical formulas introduced in the previous chapter and a numerical simulation (tracking) obtained with the accelerator simulation AT [**43**], a well proven simulation code largely used to study the beam dynamics in synchrotrons.

2.1. Storage rings lattice design

The ALBA and SOLEIL storage rings share many characteristics, especially regarding the design of the lattice. Here follows a description of the two lattices.

2.1.1. *The ALBA storage ring lattice*

A summary of the main lattice and machine parameters for the ALBA storage ring is provided in Tab. 2.1.

The magnetic lattice employed by the ALBA storage ring [**19, 34**] has a four-fold symmetry, where each of the four quadrants is composed by four cells: two "unit cells" embedded in two "matching cells" (see Fig. 2.2, 2.3 and 2.4).

Empty straight sections, characterized by small values of beta functions and dispersion, are provided in between the cells in order to host insertion devices. The small transverse beam size at these locations ensures the emission of synchrotron radiation from a well defined source point, condition required by the experimental

TABLE 2.1. ALBA storage rings lattice operation parameters (2015).

Circumference	268.8 m
Energy	3.0 GeV
Emittance	4.6 nm
Q_x	18.155
Q_Y	8.362
Natural ξ_x	-40
Natural ξ_y	-27
Corrected ξ_x	+2
Corrected ξ_y	+4
β_x / β_y at medium straight sections	2.0 m / 1.2 m

TABLE 2.2. r.m.s. variation for alignment and magnetic errors in the ALBA storage ring. Magnets are bolted onto girders, ensuring a small alignment error between magnets sharing the same girder while a worst girder-to-girder accuracy is observed.

Parameter	r.m.s. variation
Girder-to-Girder σ_x	150 µm
Girder-to-Girder σ_y	150 µm
Girder-to-Girder σ_ϕ	50 µm
Magnet-to-Magnet σ_x	25 µm
Magnet-to-Magnet σ_y	25 µm
Magnet-to-Magnet σ_ϕ	50 µm
Dipole field	0.1%
Quadrupole field	0.1%

beam-lines. Four long straight sections with a high value of beta functions are instead provided in between the quadrants, one of which hosts the injection section.

Each cell contains several magnets arranged in a double-bend achromat (DBA) configuration, where two dipoles are arranged with quadrupoles in order to keep under control the value of the dispersion in the straight sections. A sample of the magnets used in the ALBA storage ring is visible in Fig. 2.1.

The dipoles include a transverse defocusing gradient [**20**]. This results in a very compact layout and a lower transverse emittance at expense of a reduced flexibility, since the combined gradient can not be varied.

The design specification for the magnet alignment and magnetic errors are reported in Tab. 2.2. The optics change due to the magnetic and alignment errors are routinely corrected with beam-based techniques.

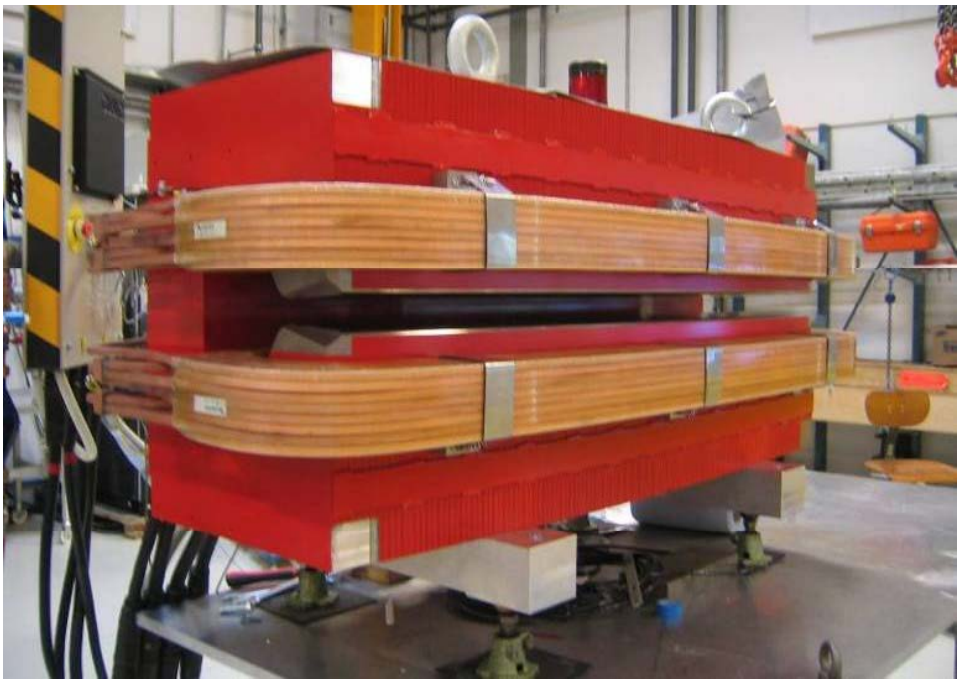

(A)

(B)

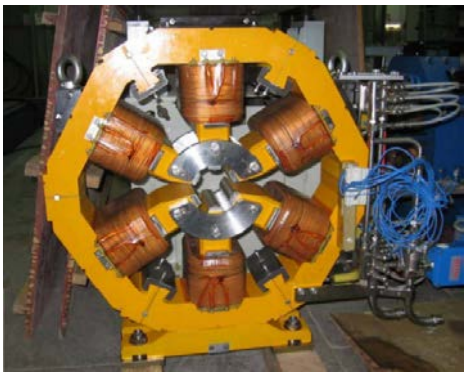

(C)

FIGURE 2.1. The three main components of the ALBA magnetic lattice: Combined-function dipoles (A), quadrupoles (B), Sextupoles (C). Sextupoles magnets incorporates multiple windings in order to provides an additional corrector field over the sextupolar one, that can be configured to produce either a small dipole (orbit corrector) or a skew quadrupole field. Out of 120 sextupoles 88 are wired as orbit correctors while the remaining 32 are wired as skew quadrupoles.

LOCO [**40, 23**] has been the tool of reference to measure the optics since the early commissioning phase of ALBA and therefore provides a solid reference to test the results of turn-by-turn measurements. The errors specified in Tab. 2.2, have been used as the basis of a previous study [**32**] to establish the ability of LOCO to

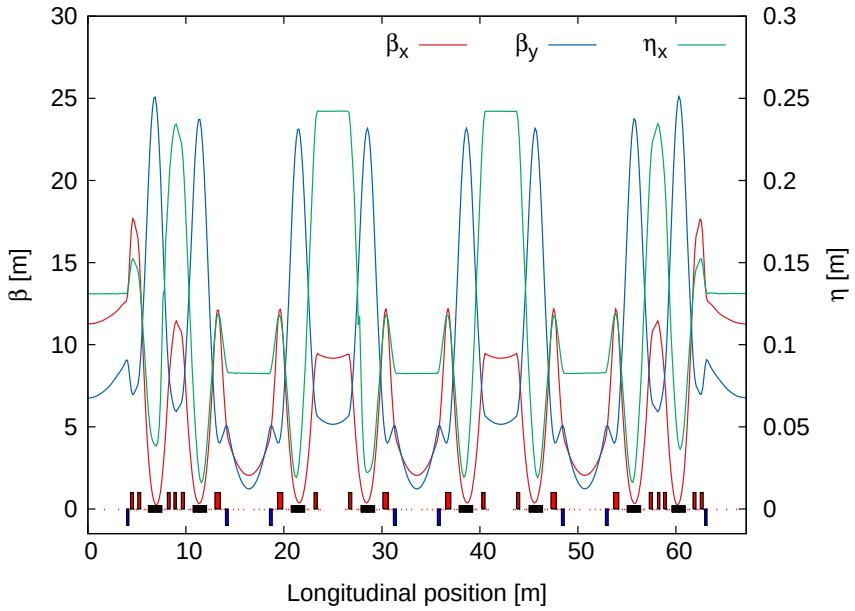

FIGURE 2.2. One quadrant of the ALBA lattice. Each quadrant is made of four cells containing two dipoles each (represented as a black rectangle) plus several focusing (red rectangles) and defocusing (blue rectangles) quadrupoles. The straight sections in between each couple of cells, where β_x and β_y reach a minimum, are reserved for insertion devices. The injection section instead, is located in the first one of the exceptionally long sections in between quadrants. The plot includes also the horizontal dispersion (η_x).

correct the storage ring lattice. The test shows an r.m.s. beta-beat respect to the nominal betatron amplitude of $\sim$1.0% for both planes, setting a measurement of the lattice accuracy. This value has to be compared against the results of the linear turn-by-turn measurements, that have been carried out on the lattice corrected with LOCO.

The ALBA storage ring is equipped with 120 sextupoles magnets, the sextupoles are grouped in 9 families, such that sextupoles belonging to the same family are powered in series by the same power supply. This solution simplifies the setup but at the same time excludes the ability to fine-tune the strength of each individual magnet in order to correct the unavoidable magnet to magnet differences. Sextupoles magnets incorporates multiple windings in order to provides an additional corrector field over the sextupolar one, that can be configured to produce

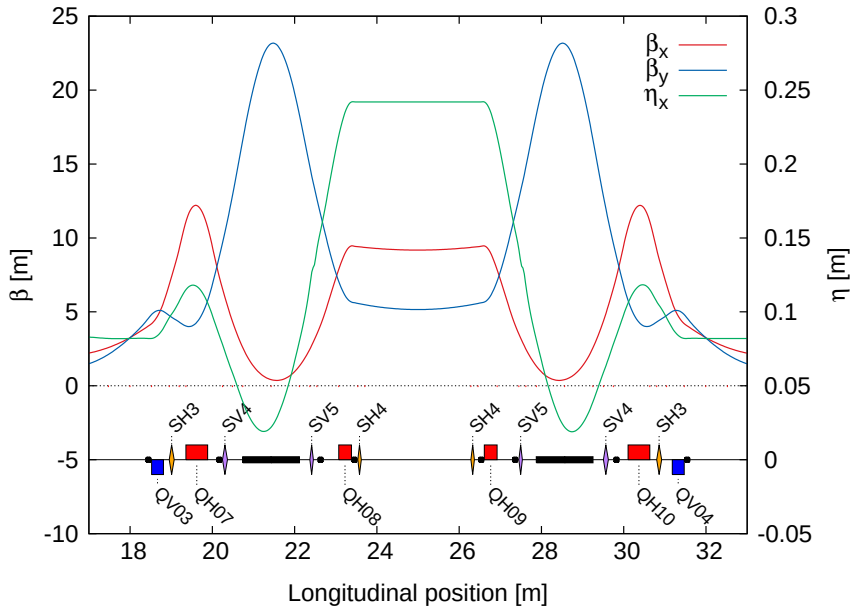

FIGURE 2.3. The ALBA unit cell includes several magnets: combined-function dipoles (black rectangles), focusing and defocusing quadrupoles (in red and blue respectively) and sextupoles (in purple and yellow depending on the polarity). The unit cell includes also 8 BPM (black dots). The available short straight sections in between the two dipoles are useful for hosting small diagnostic devices such as, for example, the pinger magnets.

TABLE 2.3. The ALBA lattice includes several types of magnets. For each type the number of elements is provided with a description of the powering scheme.

Elements	number	notes
Dipoles	32	one family
Quadrupoles	112	individual powering
Sextupoles	120	9 families
Orbit correctors	88	individual powering
Skew quadrupoles	32	individual powering
BPMs	120	

either a small dipole (orbit corrector) or a skew quadrupole field. Out of 120 sextupoles 88 are wired as orbit correctors while the remaining 32 are wired as skew quadrupoles. A list of the elements included in the ALBA lattice is provided in Tab 2.3.

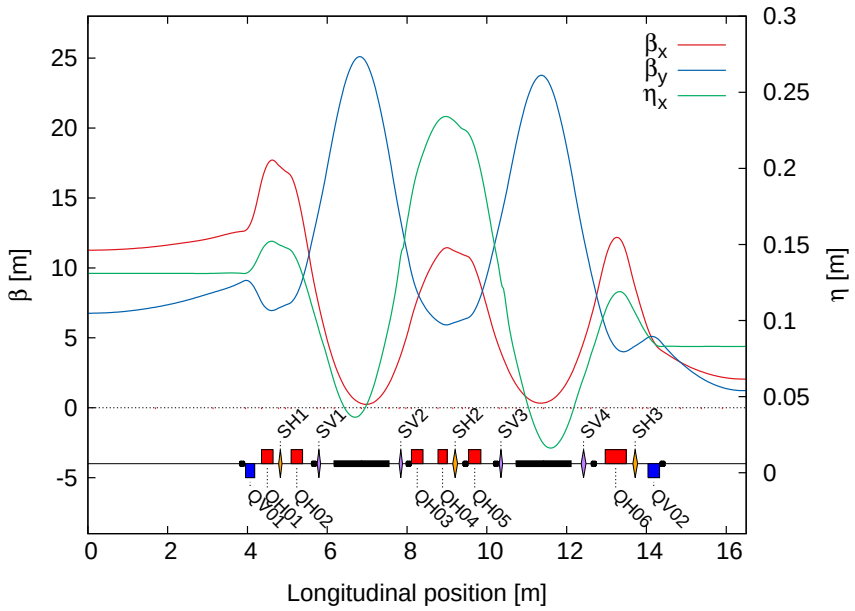

FIGURE 2.4. The ALBA matching cell has a design similar to the unit cell with the exception of providing a longer straight section (in this case on the left side) with a value of β_x and β_y suitable for the injection. Unlike the unit cell, the matching cell includes 7 BPM (black dots) instead of 8.

TABLE 2.4. SOLEIL storage rings lattice operation parameters (2015).

Circumference	354.1 m
Energy	2.75 GeV
Emittance	3.9 nm
Q_x	18.157
Q_Y	10.228
Natural ξ_x	-53
Natural ξ_y	-23
Corrected ξ_x	+1.4
Corrected ξ_y	+2.3
β_x / β_y at medium straight sections	4.2 m / 1.7 m

2.1.2. *The SOLEIL storage ring lattice*

A summary of the main lattice and machine parameters is provided in Tab. 2.4.

The SOLEIL storage ring [**15**] employs a design very similar to ALBA. In fact, except for the use of standard dipoles rather than combined-function ones, it follows the same lattice arrangement of ALBA. The storage ring has a four fold symmetry where each quadrant is composed by four cells with similar functionality as the one described for ALBA. The lattice functions for one quadrant of SOLEIL are visible in Fig. 2.5.

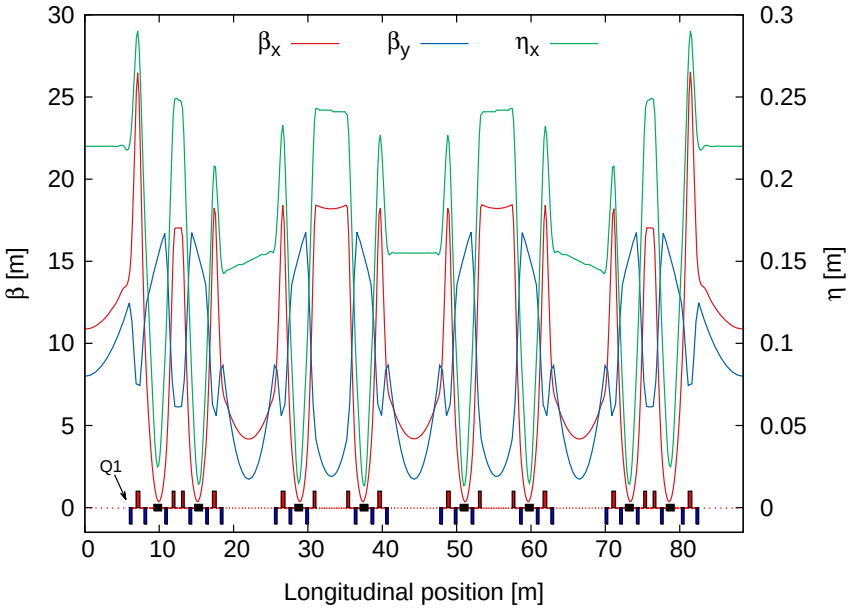

FIGURE 2.5. One quadrant of the SOLEIL lattices. As in the case of ALBA, the SOLEIL quadrant is made of four cells containing two dipoles each (represented as a black rectangle) plus several focusing (red rectangles) and defocusing (blue rectangles) quadrupoles. In between each couple of cells there are straight sections reserved for the insertion devices, where β_x and β_y reach a minimum. Similarly to ALBA the injection system is located in one of the exceptionally long straight sections in between two quadrants. The plot includes also the horizontal dispersion (η_x). The quadrupole labeled Q1 is the one used in Chapter 7 for testing the linear lattice errors assessment capabilities of turn-by-turn measurements.

2.2. Comparison of the first-order approximated and tracking simulation of coupling and non-linear errors in ALBA.

As shown in Section 1.1.2, at small amplitude, sextupoles and skew quadrupoles contribute to the transverse motion by introducing a set of new spectral components to the betatron motion (Eq. 1.41, 1.47, 1.51 and 1.58). Numerical integration is a widely used and well established tool implemented by many accelerator simulation codes that allows to obtain a very precise estimation of the betatron motion. On the other hand the computational power required to carry out the tracking makes it unpractical whenever several evaluations of the trajectory are required. This is the case of the analysis carried out in Chapter 6, where the dependency of the betatron motion on each lattice element is evaluated (magnets response matrix) and inverted in order to establish a relation between magnetic errors and experimental observations.

In this context the first-order approximated analytical formulas provide a quick alternative to tracking, but their range of validity has to be proven.

Since the existing accelerator simulation codes did not provided the functionality required to compute the first-order analytical formulas for skew quadrupoles and sextupoles, we have developed a specific code for this task.

The first-order corrections to the transverse motion due to skew quadrupoles and sextupoles have been implemented in a first instance using the MATLAB language and subsequently implemented as a "patch" to the accelerator simulation code Elegant [**14**] [1] using the C language (See Annex I for the full patch code).

In order to prove the correct functionality of the code and to establish the range of validity of the analytical formulas, we carried out a set of tests, where the results of the first-order approximation were compared against the tracking obtained with the simulation code AT [**43**]. All the tests were performed by using the ALBA linear lattice, including the skew quadrupoles and sextupole magnets and mimicking as close as possible the conditions encountered in the experimental work that will be presented in the next chapters.

[1]The patch has been accepted in the official Elegant codebase since the version 28.1.0 released on July 24, 2015.

2.2.1. *Skew quadrupoles*

A single source of coupling has been introduced in the ALBA lattice by powering one of the 32 skew quadrupoles at 8 A (as done during measurements). The horizontal turn-by-turn beam position has been computed by means of tracking and analytical formulas at one BPM location for an initial vertical beam excitation such to produce a maximum oscillation amplitude of 2 mm (equivalent to $J_y = 1.5 \cdot 10^{-7}$m).

The simulation of the resulting horizontal motion, plotted in Fig. 2.6, reveals the presence of two spectral lines: one with frequency equal to the vertical tune, signature of the coupling, and a second line at the horizontal tune. On the other hand, the superposition of the line frequency with the unperturbed horizontal tune line, makes this latter spectral line hard to measure. In fact, while it is possible to simulate a pure vertical initial excitation, it is hard to produce experimentally the same condition, where any misalignment in the pinger magnet (used to excite the initial motion) can introduce a direct excitation of the horizontal tune. Because of this limitation all the first-order corrections to the tune lines H(1,0) and V(0,1) will not be considered in the experimental work.

To finish the comparison between tracking and first-order approximation, a set of tests has been repeated including also the vertical plane and for different skew quadrupole strengths. This time the simulations have been extended to all the BPMs in the storage ring and the r.m.s. discrepancy between tracking and first-order approximation calculated. As shown in Fig. 2.7, the discrepancy gets comparable with the uncertainties observed in the experimental results only for a skew quadrupole current higher than the one used in the measurements, which confirm the validity of the analytical formula in this regime.

2.2.2. *Sextupoles*

A test similar to the previous case has been repeated to validate the first-order approximated analytical formulas. This time the sextupole SH02 from sector 4 has been powered in order to produce a non-linear integrated normalized gradient K_2 =0.3 m^{-2} (as done during measurements). In order to observe all the sextupolar spectral lines, a large betatron motion has been excited in both planes at the

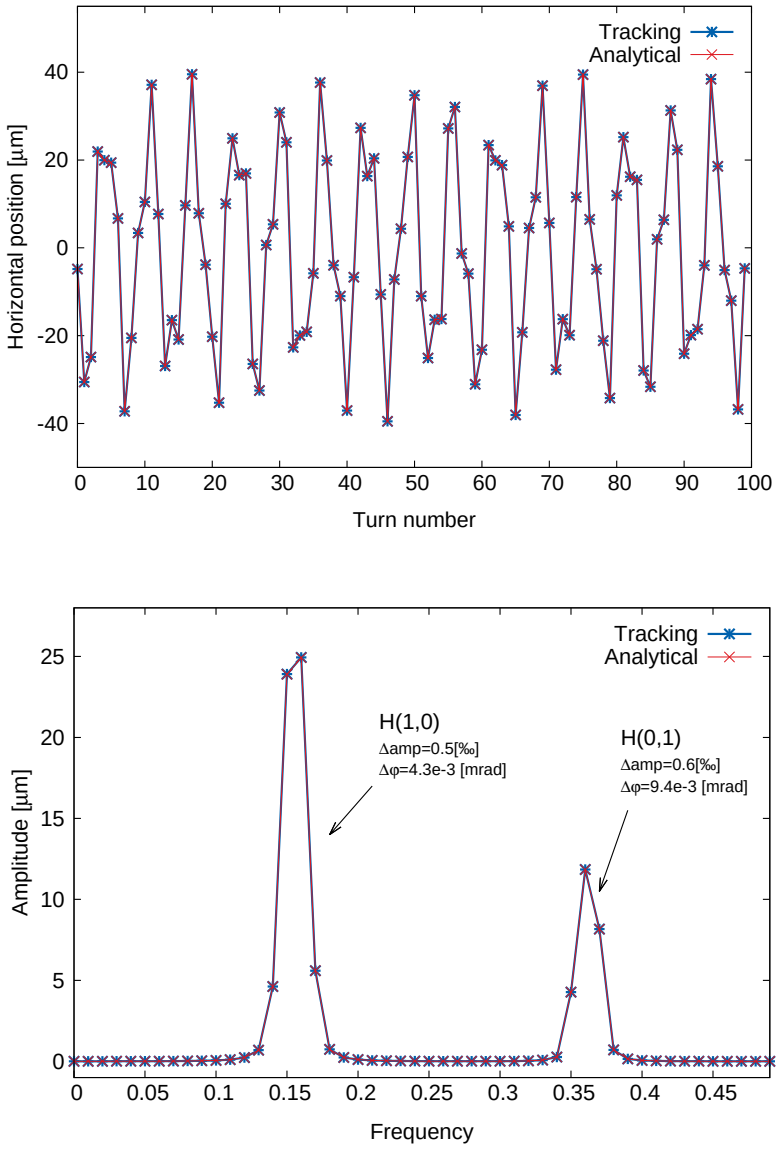

FIGURE 2.6. Horizontal turn-by-turn trajectory (top) and its Fourier transform (bottom) obtained through tracking and analytical formula. The trajectory has been sampled at one BPM location for 100 turns. In the spectrum are also shown the amplitude and phase discrepancies, between the two methods of the main peaks.

same time with maximum amplitude of 2.5 mm and 3.9 mm for the horizontal and vertical plane respectively (equivalent to $J_x = 3.6 \cdot 10^{-7}$m and $J_y = 6.0 \cdot 10^{-7}$m), values close to the ones used during measurements. Figure 2.8 shows the spectra of the horizontal and vertical turn-by-turn trajectory sampled by one BPM obtained

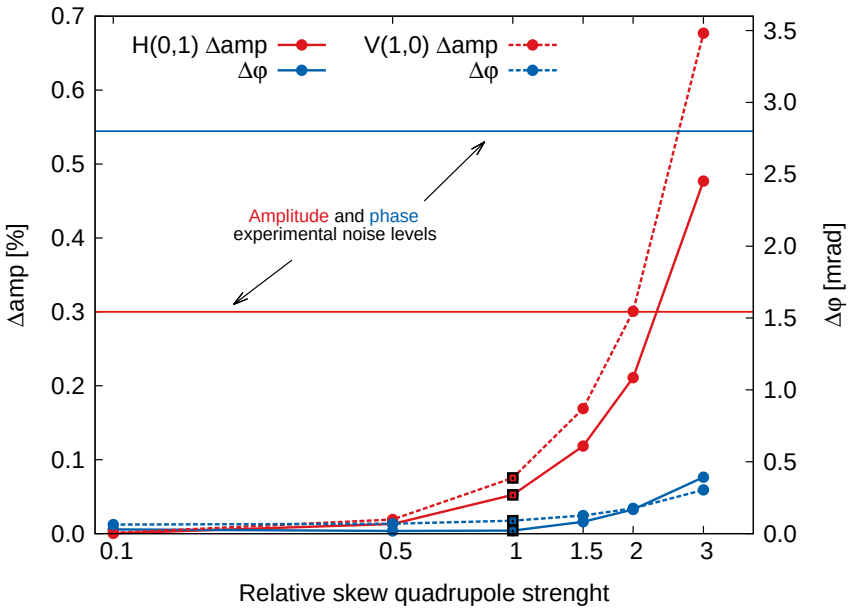

FIGURE 2.7. Comparison of tracking and first-order approximation for different strengths of the skew quadrupole, including both planes and all the BPMs. The black squares indicate the case of a skew quadrupole current of 8 A (as used for measurements), the strength is expressed relatively to this case. The two horizontal lines show the typical uncertainty that has been observed in the measurements. The discrepancy between first-order approximation and tracking gets important with respect to the experimental noise, only for a skew quadrupole strength higher than what used in the measurements.

through the analytical formula and tracking. To make the comparison of the results easier, the tracking simulations have been deprived from the high amplitude betatron oscillation ($\sim$ 3 orders of magnitude stronger than the lines under investigation) leaving the sextupolar lines only. The removal of the tune line has been obtained by repeating the tracking with and without the sextupolar perturbation, hence plotting the difference between the two simulations. Unfortunately the small amount of tune shift, introduced by the presence of the sextupole, prevents from obtaining a complete cancellation of the tune line and results in a discrepancy between tracking and analytical formula higherthan what observed for the other lines. A similar mechanism is also probably responsible for the higher discrepancy of the

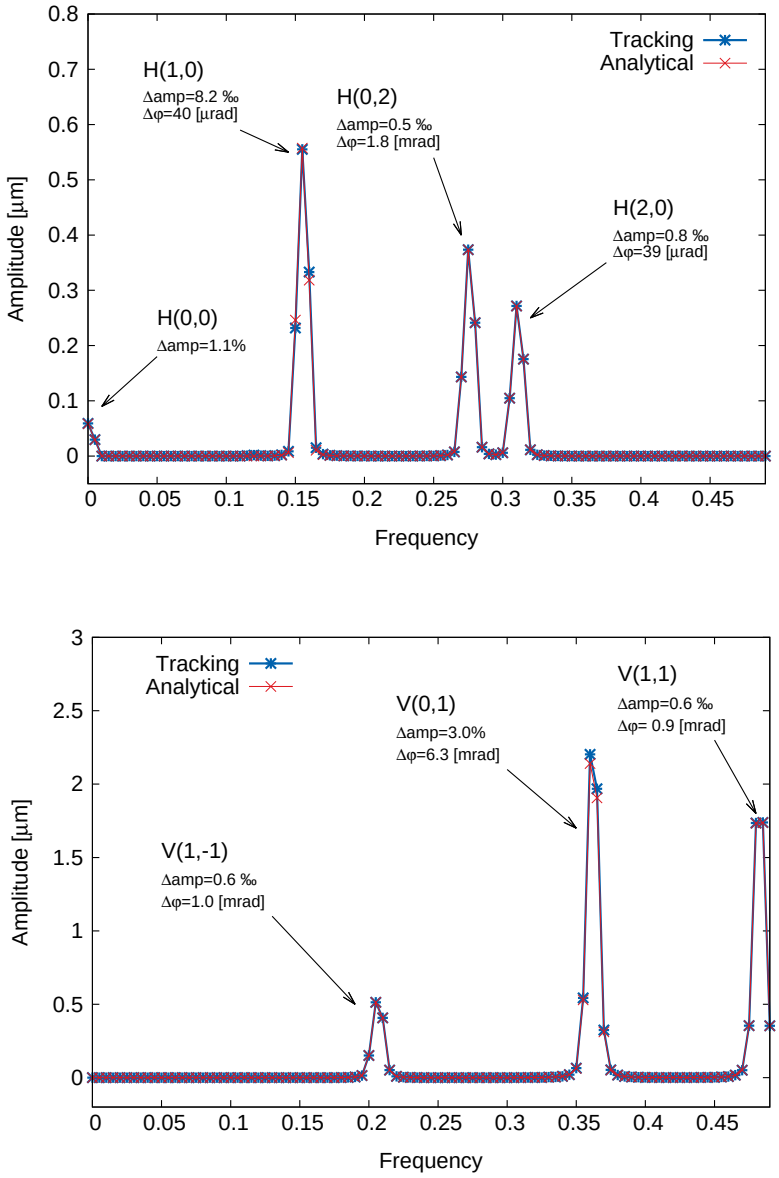

FIGURE 2.8. Spectra of the horizontal (top) and vertical (bottom) turn-by-turn trajectory obtained through tracking and analytical formula. The trajectory has been sampled for 200 turns at one BPM location. The contribution to the transverse motion due to the large amplitude betatron oscillation has been removed in the tracking by repeating the simulation without the sextupolar perturbation, hence plotting the difference between the two. A complete removal of the betatron oscillation would require the tune to not change between the two simulations. The small tune shift ($\Delta\nu_x = 7.2 \cdot 10^{-8}$ and $\Delta\nu_y = 5.0 \cdot 10^{-8}$) due to the sextupole is likely the responsible for the higher discrepancy observed in the spectral lines H(1,0) and V(0,1).

offset on the horizontal plane (spectral line H(0,0)). In fact the tracking takes into account also the orbit change produced by other effects that have not been included in the analytical formula, such as the path lengthening [**42**] due to the excitation of the betatron motion. On the other hand, because these lines have not been used in the experimental work, no further investigation has been necessary.

To complete the validation of the analytical formula, a set of simulations have been repeated, including all the BPMs, and for different sextupole strengths and excitation amplitudes. In fact, unlike in the case of skew quadrupole where no amplitude dependency was observed, the sextupolar strength changes non-linearly with the transverse position, resulting in a stronger effect at high amplitudes. As visible in Fig. 2.9, also in this case the discrepancy becomes important with respect to the experimental uncertainties only when departing significantly from the parameters used during measurements.

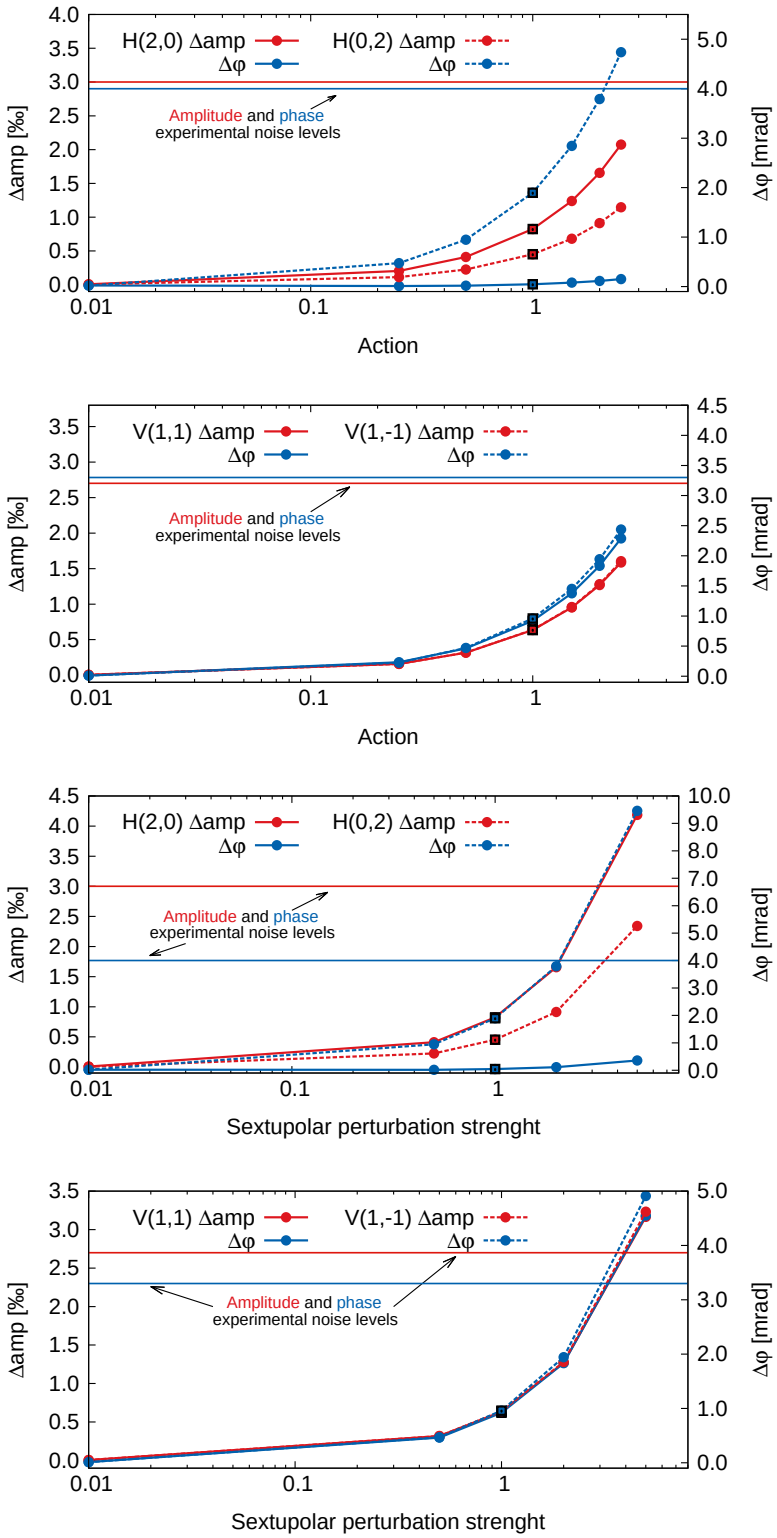

FIGURE 2.9. Comparison of tracking and first-order approximation for different sextupole strengths and excitation amplitudes. The black squares indicate the reference case described in the text. The two horizontal lines show the typical uncertainty that has been observed in the measurements. Sextupole strengths and excitation amplitudes are expressed relatively to the reference case.

CHAPTER 3

BPM turn-by-turn data acquisition

3.1. Beam position monitor

Beam orbit observation has become a workhorse for accelerator diagnostic, being widely used in modern machines, which are equipped with an increasing number of beam position monitoring device. Different applications with different requirements resulted in the development of many different beam position monitoring techniques. In this case the beam position monitoring technique of election is based on sampling the electric field produced by the charge stored in the ring through a capacitive coupling. This approach allows for a very quick and precise measurement of the beam transverse position without intercepting the beam itself and therefore, allowing to sample the transverse beam position on a turn-by-turn basis over thousands of consecutive turns.

3.2. Theory of operation

Approaching the ultrarelativistic limit, the electric field lines emanated by a point-like electric charge get squeezed in the direction of motion, resulting in a pancake like shape as depicted in Fig. 3.1. If the charge moves in a conductive beam pipe an image charge on the beam-pipe walls is observed as a result of the interaction between the field emanated by the charge itself and the beam-pipe. Since the field strength on the beam-pipe walls depends on the charge position, the

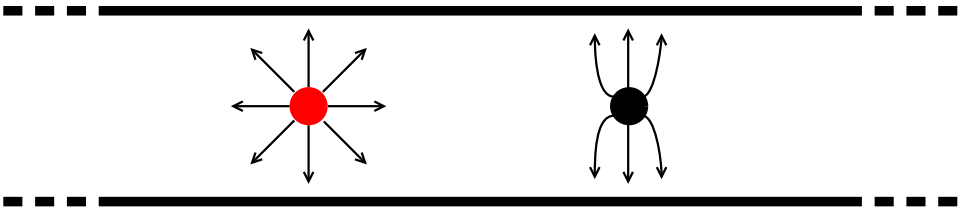

FIGURE 3.1. The Electric field lines of a charge (red) get squeezed in the direction of motion when approaching the ultrerelativistic limit (black).

measurement of the induced image charge at different azimuthal angles allows to determine the transverse position of the charge. In his simplest implementation, a BPM uses a set of capacitive pickup electrodes (buttons) to sample the electric field produced by the charge at different azimuthal angles field produced and determines the beam position. A common configuration is shown if Fig. 3.2 where four electrodes spaced 90 degrees each other, pierce through the beam pipe and surround the beam allowing for a full determination of the transverse beam position. When the beam pass through the BPM an electric field reach each button with a

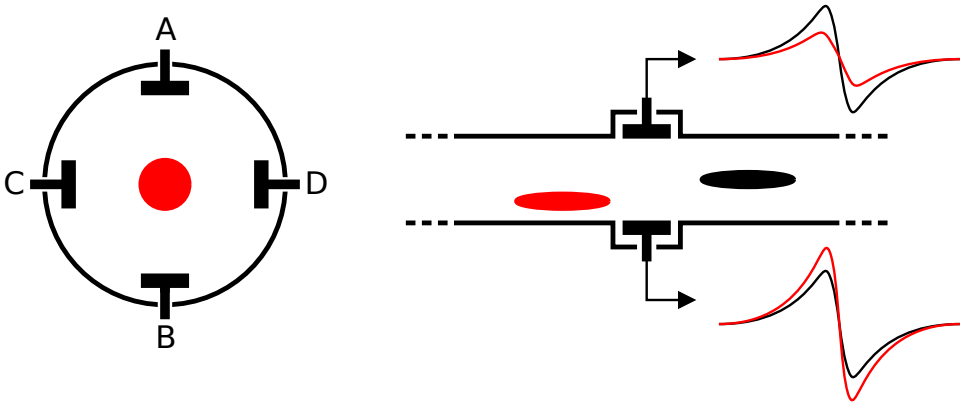

FIGURE 3.2. On the left a transverse cross section of a BPM. Here the four buttons facing toward the beam (red dot) are visible. On the right a longitudinal cross section showing two bunches (red and black ellipses) crossing the BPM. The signals produced on two opposing buttons is also shown.

different strength depending on the beam-button distance, inducing a proportional image charge Q on the button it self. Accordingly a voltage $V = Q/C$, where C is the button capacitance is induced on the button. In a properly designed BPM the induced voltage will be proportional to the beam position in a fairly large region of the transverse space. In this linear region the beam position can be calculated from the measured voltage using the simple expression:

$$x \propto \frac{V_a - V_b}{V_a + V_b}, \tag{3.1}$$

where V_{i} is the voltage induced on two facing buttons. At higher beam displacement a proper electromatgnetich simulation of the BPM response is required in order to take into account the non-linearity and reconstruct the beam position with high accuracy.

Whenever a beam pipe with complex geoemetry is employed, e.g. elliptical beam pipe, is common to use buttons geometries that differ from the reference case of Fig. 3.3. This is the case of light sources, where beam pipes are designed

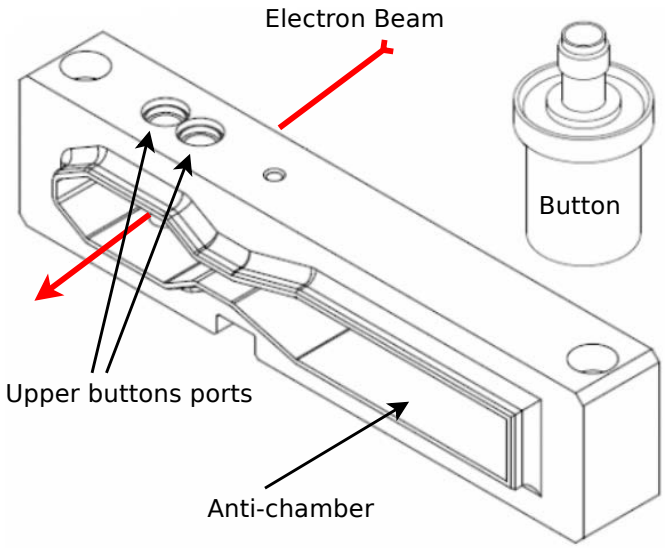

FIGURE 3.3. Schematic drawing of an actual BPM used in the ALBA light source. The electron beam, in red, travels through the smaller portion of the chamber while an antichamber is needed in some section of the machine to accomodate for synchrotron radiation extraction. The four buttons are located at a different angle respect to the more traditional round chamber geometry.

to accommodate for synchrotron radiation. In this case flattened geometries and antichambers, to allow the extraction of synchrotron radiation, are common choices.

Figure 3.4 shows the geometry of the BPM employed in the machines referred in this work. A round chamber and a stripline solution is used in the case of LHC, while all the three light sources under investigation employ capacitive BPM and asymmetric vacuum chambers. The use of asymmetric chamber geometry do not pose any limitation for the small amplitude measurements, where the beam is confined to the linear region, while at high amplitude intricated electromagnetic simulations are required to characterize the BPM response.

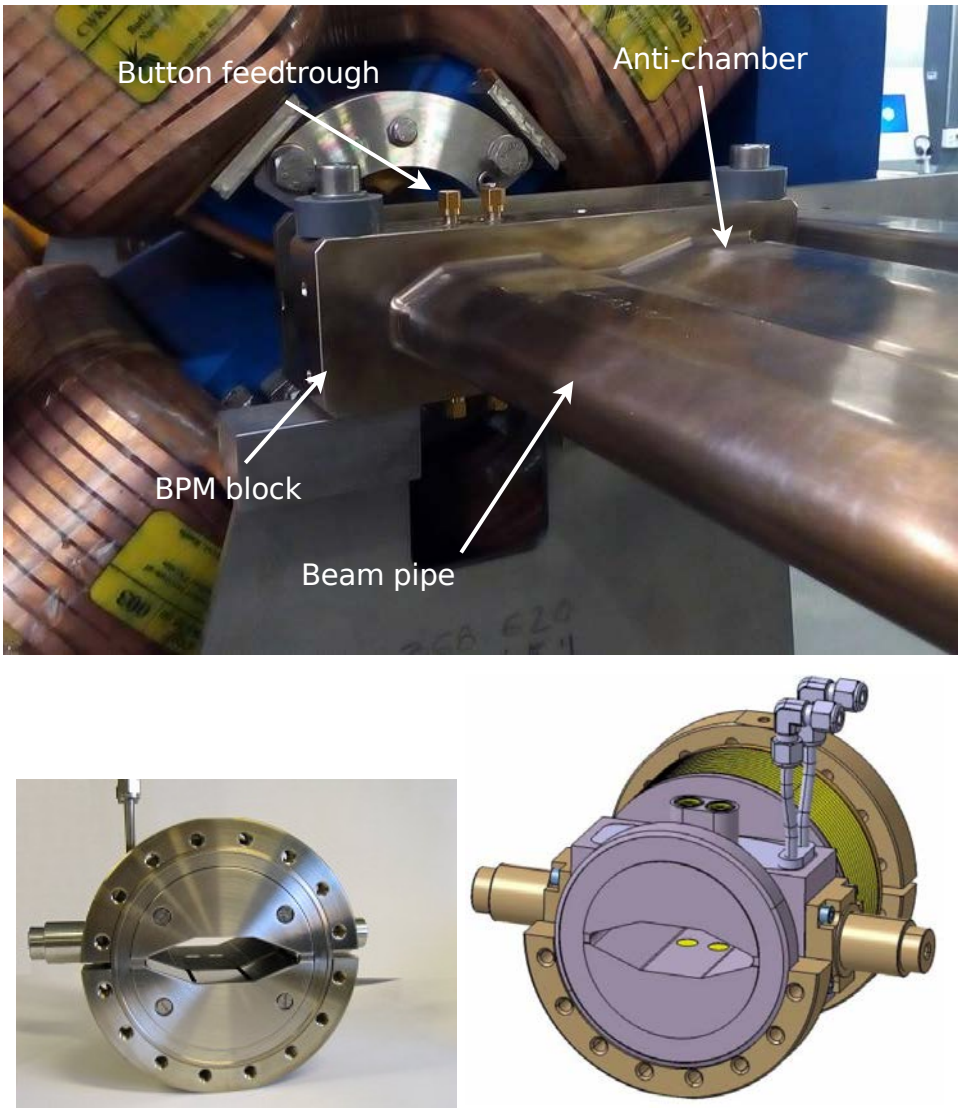

FIGURE 3.4. Different flavors of BPM: On top one of the ALBA BPM installed in the ring. In the picture is visible the BPM block provided with the four feed-troughs that connects to the buttons (contained inside the block and not visible in the picture) and the characteristic flattened vacuum chamber. The SOLEIL BPM, that employ a very similar design, is instead visible on the bottom.

3.3. Single turn capable electronics

The temporal structure of the produced signal follows closely the longitudinal beam structure. Each time a bunch travels across the BPM a very fast signal is induced on each button (Fig. 3.2), therefore a train of bunches travelling through the BPM, induce on each button a radio frequency burst whose fundamental frequency

is determined by the intra-bunch spacing, that for an electron storage ring usually falls in the range between 10 ns (100 MHz) and 2 ns (500 MHz), while hadron machine can easily extend to lower frequency. Common radio receiving and demodulation techniques are suitable in order to measure the amplitude of such radio frequency signal and accordingly deduce the beam position.

Furthermore in order to carry out a beam position measurement on a turn-by-turn basis the measurement itself should last less than the storage ring revolution time that, in the case of a light source, is roughly between 1 µs and 3 µs.

All such considerations pose some significant constraint on the electronic receiver and demodulation-chain.

3.3.1. *Down frequency convertion approach*

As in a radio receiver the very first high frequency signal preconditioning is carried out by a fully analog front-end, consisting of a tuned filter, amplifiers and attenuators. Followed by a next step of down conversion, further filtering and signal detection.

As the radio frequency techniques have evolved replacing more and more of the analog components with their digital counterpart, a similar trend was observed in BPM technology where an early digital to analog conversion is performed just after the analog front-end, removing the need for a down frequency conversion and therefore drastically simplifying the analog front-end section. One of the major advantage of such approach is a very general and flexible solution, in fact, since most of the signal manipulations are realized in the digital domain usually in a field programmable gate array (FPGA) it is possible to employ the same BPM electronics on different machines requiring only some minor parameters adjustment. Only the very first filtering stage in the analog front-end needs a complete redesign to cope with the specific RF frequency employed by each different machines. This made it possible the commercialization of standardized BPM solutions that require minimal tuning to fit the requirements of different customers. Figure 3.5 shows the schematic of a typical modern BPM electronics as the one employed in most of the synchrotron light sources. After a first programmable attenuator and a tuned filter, which is the only machine specific component, the analog to digital conversion

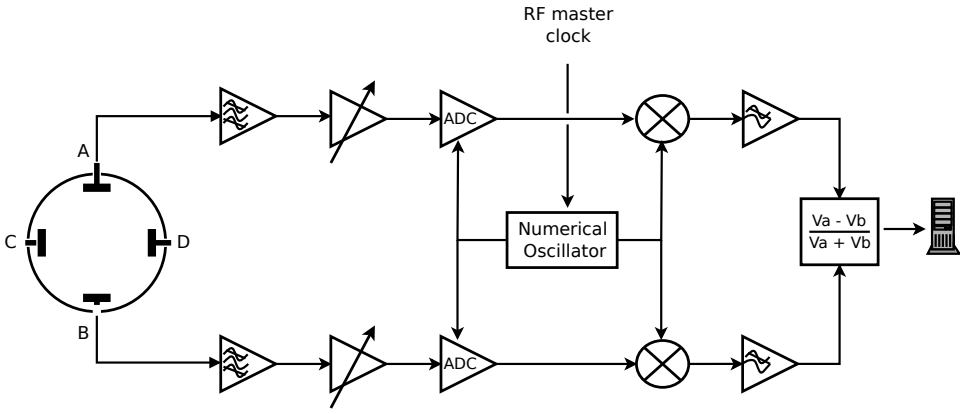

FIGURE 3.5. Block diagram of two channels of a BPM operating with the subsampling technique.

stage follows directly. Because the input signal frequency falls in the range between 100 MHz and 500 MHz, a full bandwidth analog to digital conversion would be impractical requiring a very expensive converter, instead down sampling technique is preferred. The Shannon sampling theorem states that, in order to fully reconstruct a signal without any information loss, the digital conversion has to be operated with a frequency at least twice the signal characteristic frequency. Sampling the signal at a lower frequency would result in the aliasing phenomena where different parts of the spectrum fold one over the other and get indistinguishable. In other words the sampling frequency defines a set of zones, known as the Nyquist zones, where a signal that belongs to a higher Nyquist zone would alias down into the first Nyquist zone (Fig. 3.6). Therefore, since the signal collected by the BPM buttons signal has relatively low bandwidth, it is common to operate the analog to digital conversion with a lower frequency such that the whole signal spectrum falls in a higher Nyquist zone and still being able to fully reconstruct the signal. Special ADC, with a particularly short acquisition window are required to operate in higher Nyquist zone, still a downside of such technique is a reduction of the overall ADC performance. Nevertheless the overall simplification deriving from the down-sampling approach is very appealing.

If all bunches in the beam follow the same transverse motion in a rigid manner, the overall signal bandwidth would be determined by the revolution frequency: the bunches train crosses the BPM at a different position at every turn, while during

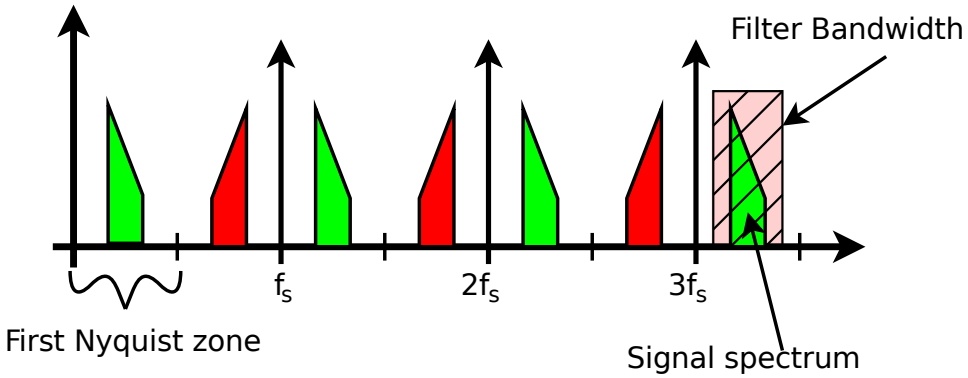

FIGURE 3.6. Frequency domain representation of the subsampling process. In this case the sampling frequency f_s has been chosen such that the sampled signal falls into the seventh Nyquist zone. The observed signal after the sampling is virtually indistinguishable from a replica that belongs to another nyquist zone, for this reason a band-pass filter is needed to remove all the frequencies that do not belongs to the selected Nyquist zone.

the same turn all bunches stay at the same location resulting in a turn by turn change in amplitude of the RF carrier. Both the tuned filter in the analog front-end and the bandwidth of each Nyquist zone in the analog conversion is well above this limit guaranteeing a proper signal reconstruction.

Once the signal has been converted to the digital domain the demodulation proceeds with a numerical direct conversion independently for each button. A numerical oscillator, driven by the storage ring RF, feeds two numerical mixers with a quadrature and phase signal tuned at the same frequency of the sampled signal in a direct conversion fashion. Next follows a filtering stage, a magnitude detector and the final beam position is calculated applying Eq. 3.1. In order to guarantee a proper reconstruction of the beam position on a turn-by-turn basis the bandwidth of this last filter has to be higher than the ring revolution frequency. Unluckily this last filtering stage implemented in the BPM electronics under examination at the three light sources, ESRF, ALBA and Soleil, did not fully satisfied this requirement.

Both ESRF and ALBA have BPM equipped with a "Libera Brilliance" commercial electronics provided by Itech [**1**], while at Soleil a sligltly older version, under the name "Libera Electron" is in use. All these electronics are provided by

default with a rather slow filter that do not allow for proper turn by turn measurement, reulting in what is commonly known as "turn mixing". Two different approaches are possible to solve the problem:

- Replacing the filter with a properly designed one, which does not mix consecutive turns.
- Postprocess the data by deconvoluting the turn by turn beam position with the response function of the filter in order to undo the actions of the filter.

While the first approach, being more elegant and efficient, would be preferred over the second one, lack of documentation prevented to apply it in the case of Soleil BPMs. Instead a new filter, known as MAF (moving average filter), developed on purpose was used for ESRF and ALBA [**41, 28**].

In this new filter the in-phase and quadrature components of each BPM button streamed at the ADC sampling rate are decimated down to the ring revolution frequency by means of averaging over a fixed time window shorter than one turn and synchronized with the beam crossing: each time the bunch train starts passing through the BPM, the averaging process is initiated (the window is opened) and is terminated only once the whole train has passed (the window is closed). This approach makes it impossible for the signals produced at different turns to affect each other and ensures a proper turn-by-turn reconstruction of the beam position. On the other hand, since the BPM has no means to establish when the train starts or finishes the timing of the averaging window has to rely on a tight synchronization with the accelerator timing system. For this purpose each BPM receives a clock signal that marks the turn of the train. Each BPM determines the start of the averaging window by waiting a predefined delay after the clock signal has been asserted and the window is closed after a fixed time equal for each BPM. Since each BPM is physically located at a different position in the storage ring and connected to the buttons and to the timing system, with cables of different and sometimes unknown length, a proper delay value has to be measured precisely for each individual BPM. For this purpose we measured for each BPM the proper delay between train and clock arrival by scanning the delay value while observing

the sum of the signal amplitude of the 4 buttons, which do not depends on the beam position but only on the signal intensity. If the measurement is carried out with a short window and a short train it is easy to observe when the averaging window and train overlap (A detailed description of the procedure and results will be provided in Chapter 5).

3.3.2. *MAF implementation at ALBA*

Because of the limited resources available on the FPGA, the MAF and standard firmwares can not cohabit on the BPMs. Instead, whenever the turn-by-turn capabilities are required, the MAF firmware has to be loaded on each BPM and unloaded before resuming standard operations resulting in a rather convoluted procedure. In fact, this routine is far from being error-proof and requires a certain amount of "human intervention" in order to make sure that every BPM is working correctly after the FPGA has been reprogrammed and the BPM rebooted. The whole process can last easily up to 30 minutes discouraging the use of turn-by-turn measurements whenever not really required. For this reason, during the normal operation of the ALBA storage ring, slow acquisition measurements are still preferred over the turn-by-turn ones that instead have been tested limited to the time assigned for machine studies. On the other hand it is important to stress that this condition is due only to a technical issue and is not an intrinsic limitation of the turn-by-turn technique.

CHAPTER 4

The ALBA pinger magnet

In order to provide a transverse beam excitation required for the turn-by-turn studies, the ALBA storage ring has been equipped with a pair of fast pulsed dipolar magnets (pingers). Two pingers, which provide horizontal and vertical beam displacement, are placed one next to the other.

An accurate characterization of the pingers was realized before the installation in the storage ring. Measurements in the ALBA laboratory were carried out in order to verify the proper operation of the magnets.

It is important to note that in the context of this work a thorough characterization of the pingers pulse is not required since, the analysis of the measurements to follow have been carried out in such a way to remove any dependency on the initial phase and amplitude of the betatron motion, that in turn are determined by the pinger pulse characteristics.

4.1. Design of the pinger

Two main parameters, defined according to the experimental requirements, characterize the pingers: the maximum peak magnetic field strength and the pulse length. While the peak magnetic field strength is determined from the maximum beam oscillation amplitude allowed by the physical aperture, the magnetic pulse length is constrained by the storage ring circumference. In fact, in order to excite a short train of bunches in one single turn, the magnetic pulse has to last less than two times the beam revolution period minus the train length, as explained in Fig. 4.1. For the ALBA storage ring this conditions results in a pulse length shorter than 1.7 µs.

Because eddy currents would not allow the pulsed magnetic field to penetrate the standard stainless steel vacuum chamber used in the ALBA storage ring, a ceramic (allumina) chamber has been employed. A 400 nm titanium coating, on the

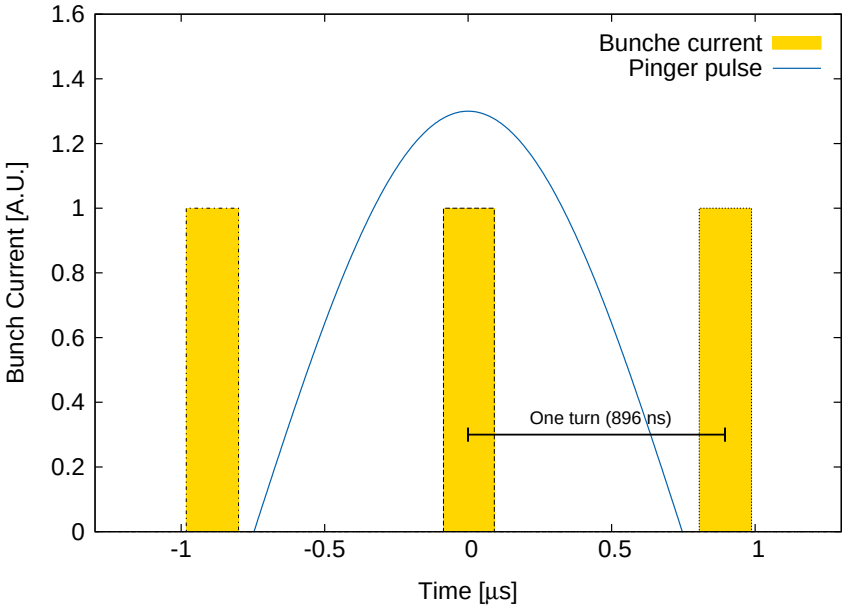

FIGURE 4.1. Single pulse short train excitation scheme. Dealing only with short trains of bunches allows to use a magnetic pulse length up to two times the revolution time minus the train length (90 ns) and still obtain a single turn excitation. In the case of ALBA the target pulse duration has been fixed to 1.5 µs for both pingers (horizontal and vertical).

inner wall of the ceramic chamber, is required in order for the beam-image current to flow without interruption. A single loop of copper, wound directly around the vacuum chamber, produces the magnetic field that is guided with the help of ferrite blocks (CMD5055, from Ceramic Magnetic Ltd [**2**]) arranged in a window frame geometry (Fig. 4.2). A complete description of the magnetic design is covered in [**39**]

The maximum kick angle is fixed to $\theta_x = 2.0\,\text{mrad}$ and $\theta_y = 1.4\,\text{mrad}$ for the horizontal and vertical pinger respectively. Therefore, assuming a homogeneous magnetic field along the longitudinal axis, the required field $B_{x,y}$ can be obtained from the relation:

$$B_{x,y} = \frac{p}{c}\frac{\theta_{x,y}}{l}, \tag{4.1}$$

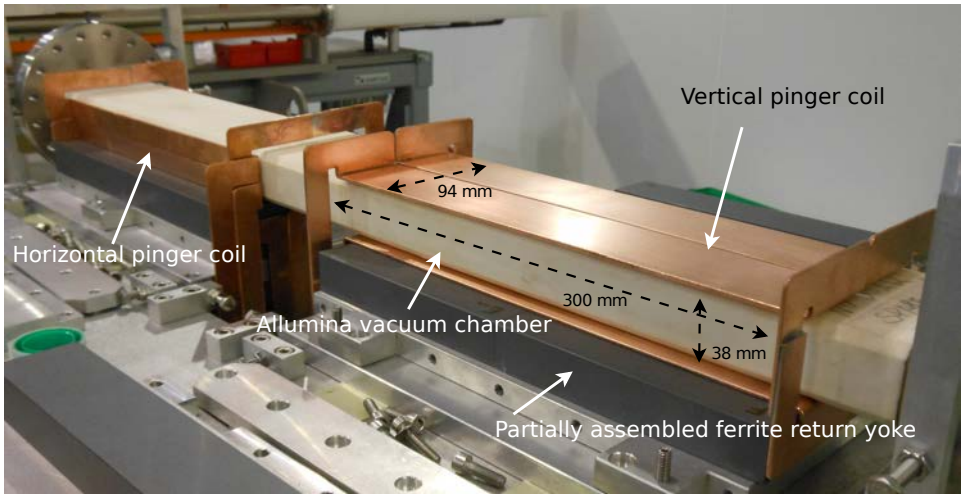

FIGURE 4.2. A view of the two semi-assembled pingers. In the picture are visible the copper coils wound around the ceramic vacuum chamber and a few ferrite blocks that constitute part of the magnetic field return yoke. The high voltage pulsed power supply (not visible) is housed below the pinger as close as possible to the coils in order to keep the leads short reducing the stray inductance.

where p is the beam momentum, c the speed of light and l the magnet length that in this case is 300 mm. Hence a magnet current I_x=2.0 kA and I_y=3.5 kA is calculated from the required magnetic field (B_x =67 mT and B_y =77 mT) using the Ampere's law:

$$B_{x,y} \simeq \frac{\mu_0 I_{x,y}}{l}. \tag{4.2}$$

From an electrical point of view the magnet behaves almost as a pure inductor, allowing to drive the circuit in a resonator configuration, where a high voltage charged capacitor C is connected, through a high speed isolated solid state switch (Behlke, model HTS 120-500-SCR [**3**]), to the magnet coil forming a tank circuit as shown in Fig. 4.3.

The capacitors are sized in order to obtain, when connected to the magnets coils, a resonant circuit with a time constant of τ=1.5 µs. The time constant has been fixed in order to allow a single turn excitation (condition realized for $\tau <$ 1.8 µs), but still guaranteeing a flat temporal profile along a short train of bunches (bunch to bunch excitation discrepancy is less than 1% for a 45 bunches train as the one used for measurements). The capacitance $C_{x,y}$ is inferred from the pulse

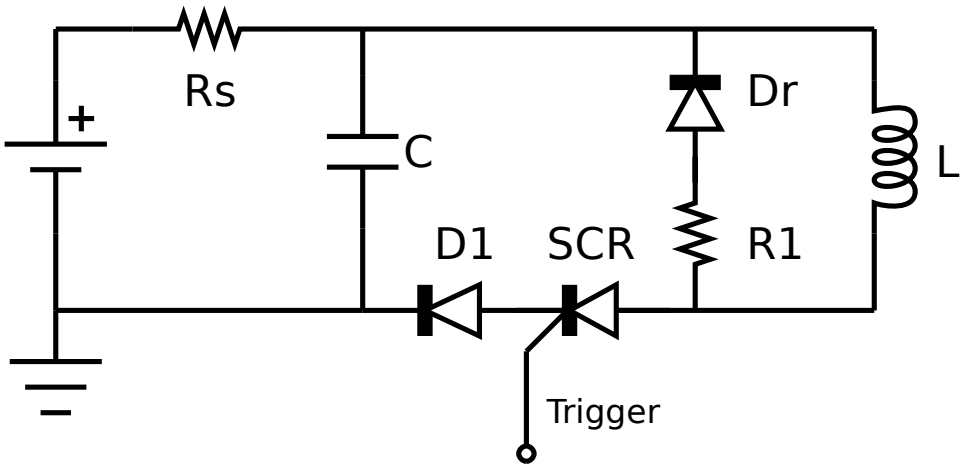

FIGURE 4.3. Pinger pulsed power supply schematics. The coil of the pinger is represented as an inductor (L). To power the pinger magnet the high voltage SCR is switched on connecting the capacitor C, charged at high voltage through the resistor Rs, to L and therefore forming a resonant circuit. The diode D1 is required in order to inhibit the SCR from switching on again during the negative voltage phase of the oscillation, while Dr and R1 provide a path for the energy stored in the coil to be dissipated.

length and the inductance $L_{x,y}$ of the coil (plus the coil leads) using the resonant frequency ω of the tank circuit:

$$\omega = \frac{\pi}{\tau} = \frac{1}{\sqrt{L_{x,y} \cdot C_{x,y}}}, \tag{4.3}$$

where the value of $L_{x,y}$ can be approximated as (one turn coil):

$$L_{x,y} \simeq \frac{B_{x,y} \cdot S_{x,y}}{I_{x,y}}, \tag{4.4}$$

with $S_{x,y}$ the coil surface and $I_{x,y}$ the peak current. Solving for the two coils provides L_x=933 nH and L_y=152 nH to which is added 600 nH to take into account for the stray inductance of the leads. Finally, substituting the values into Eq. 4.3 a value of $C_x \simeq$150 nF and $C_y \simeq$300 nF is obtained.

The capacitor charge voltage $V_{x,y}$ is instead determined from the required peak magnetic field using the relation:

$$V_{x,y} = L_{x,y} I_{x,y} \omega = L_{x,y} I_{x,y} \sqrt{\frac{L_{x,y}}{C_{x,y}}}, \tag{4.5}$$

TABLE 4.1. Main design parameters for the horizontal and vertical pingers.

Parameter	Horizontal	Vertical
Max transverse kick [mrad]	2.0	1.4
Max peak field [mT]	67	47
Max coil voltage [kV]	6.5	5.5
Peak current [kA]	2.0	3.5
Pulse length [μs]	1.5	1.5
L (including cables) [μH]	1.5	0.75
C [nF]	150	300
Length [mm]	300	300
Magnet gap [mm]	38	94
Pulse to pulse r.m.s. fluctuation [%]	< 0.1	< 0.1
Pulse jitter [ns]	< 1	< 1

providing $V_x \simeq 6.5\,\mathrm{kV}$ and $V_y \simeq 5.5\,\mathrm{kV}$. A comprehensive table of the design parameters for the two pingers is found in Tab 4.1.

The choice of a resonant circuit design was driven mainly by the resulting simplification of the power supply. A major weakness of such approach lies in the inability to excite, with a sinusoidal pulse, a long train of bunches at constant amplitude. This condition constrains effectively the maximum amount of charge that can be used in the turn-by-turn measurements, and therefore the signal strength produced by the BPMs. On the other hand the limited bandwidth of the BPM receivers employed at ALBA along with the small circumference of the storage ring would not allow in any case to work with much longer train of bunches, mitigating the limitations introduced by such design choice.

4.2. Characterization of the field and length of the pulse as a function of the current

Figure 4.4 shows the results of measurement performed at ALBA of the vertical pinger magnetic field and current for the a capacitor voltage of 1.0 kV, which is the minimum value used during experiments. The field was measured by placing a loop of wire inside the magnet bore while the pinger coil current with an inductive probe (transformer) on the coil leads. The measured pulse length was 1.7 µs, which is a value higher than the design one of 1.5 µs. Repeating the measurement for

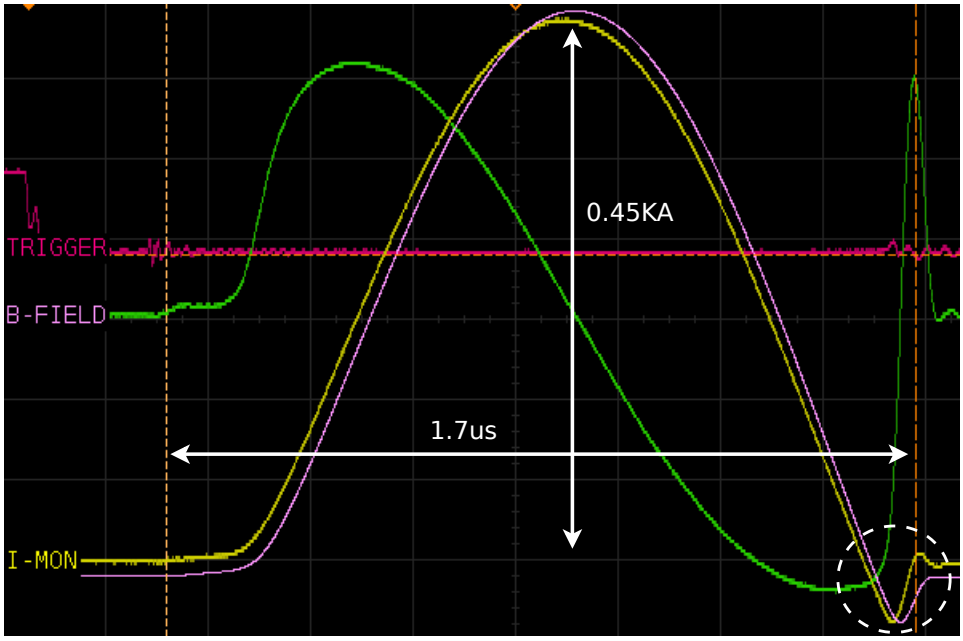

FIGURE 4.4. Measurement of the magnetic field and current for the vertical pinger observed for a capacitor voltage of 1.0 kV. This setting represents the worst condition the pinger has been operated for experiments. In fact, because of the non-linear behaviour of the solid state switch, lowering the voltage results in a lenghthening of the pulse, that in this case reaches 1.7 µs. At 2.5 kV, the higher setting used for experiments, instead the pulse length drops to 1.4 µs. Due to the capacitance and storage time of the diodes and SCR the current drops to a negative value (white circle) for a short time before swinging back to zero, anyhow this feature has no effect on the performance of the magnet.

higher voltages has shown instead a shortened pulse as a consequence of the non-linear behaviour of the solid state switch (whose resistance depends on the current), dropping to 1.4 µs for a capacitor voltage of 2.5 kV (maximum value used in the tests). The horizontal pinger instead exhibits a rather flat behaviour around the settings used for experiments (between 0.5 kV and 1.5 kV) with a pulse length oscillating between 1.1 µs and 1.0 µs.

The pinger magnets are triggered at 3.125 Hz by the ALBA timing system and are locked to the beam revolution frequency. An adjustable delay makes it possible to synchronize the magnetic pulse with the beam passage. The magnets have been installed in a short straight section (see Fig. 2.3), in between the two dipoles of a unit cell, where the relatively high values of $\beta_{x,y}$ allow to excite the beam with a lower magnetic field.

CHAPTER 5

Turn-by-turn measurements setup

In order to implement correctly turn-by-turn measurements a tight synchronization between pinger, BPMs and the storage ring timing system is mandatory. Especially in the case of the "young" ALBA light source, where the turn-by-turn technique was implemented for the first time an extensive setup of the different components has been required. Indeed such timing adjustment represented the most demanding part of the whole work being the result of a long trial-and-error process. Conversely the measurements carried out at SOLEIL did not require any complex adjustment procedure since most of the synchronization issues had already been solved during the previous years of operation.

5.1. ALBA setup

The ALBA storage ring turn-by-turn experimental setup includes 120 BPMs, two pinger magnets (one for the vertical and one for the horizontal plane) and a timing distribution network that delivers a trigger signal to the pingers and to the BPMs. Figure 5.1 shows a schematic view of the timing distribution network. The trigger signal is synchronized with the accelerator revolution frequency and the 50 Hz line frequency in order to suppress any noise induced by the power lines in the measurements. Since the timing distribution network and the connection between the BPM pickups and the BPM receiver electronics is realized through cables of different length stretching for several tenths of meters, a proper calibration is required in order to establish the overall delay of the connections and achieve the required synchronization.

5.1.1. *BPM synchronization*

Measuring and comparing the betatron phase at different locations around the storage ring requires the readout of all the BPMs to be synchronized on a turn-basis in such a way that the data gathered from each BPM refers to the same turn.

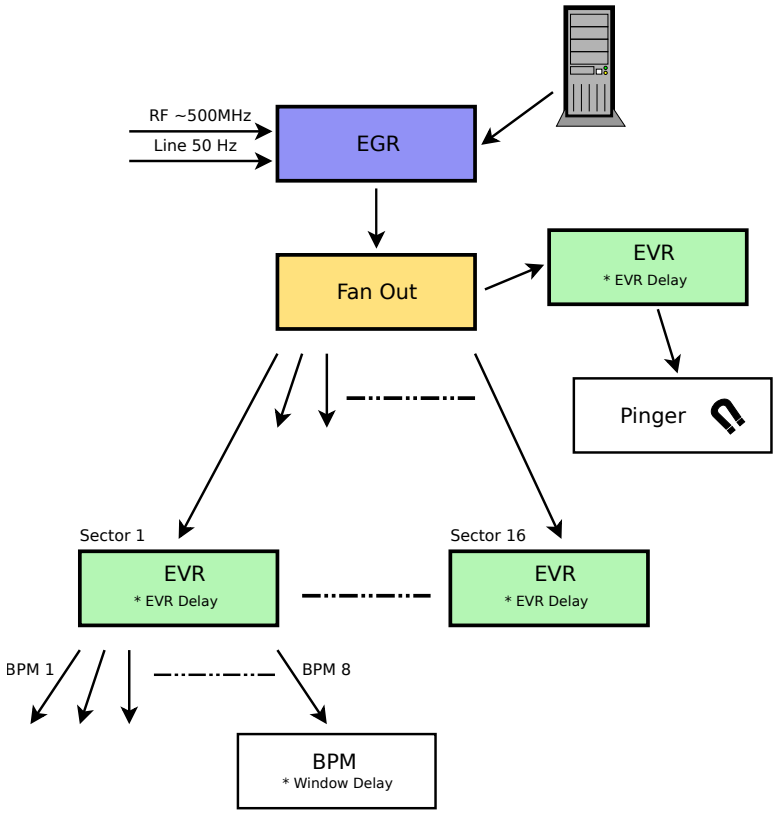

FIGURE 5.1. The timing system of the ALBA storage ring includes an *event generator* (EVG) which broadcasts timing message on a dedicated network. The network splits in 16 branches, one for each sector where is connected to an *event receiver* (EVR). The EVR decodes and forwards the trigger signal to all the BPMs in the same sector. the EVRs allow to introduce a per-sector delay, while a fine delay adjustment is provided internally by each BPM. Timing signals are generated by the EVG synchronously with revolution frequency of around 1.116 MHz which in turn is locked to the main RF frequency ($\sim$ 500 MHz). The trigger signals sent to the BPMs are also kept synchronous with respect to the main line frequency of 50 Hz, to minimize the effect of the unavoidable coupling of main signal to the experimental apparatus. The timing of the pinger magnet is driven by a dedicated EVR connected to the same timing network.

Furthermore the beam signal and the MAF window must be properly synchronized for each BPM to maximize the acquired signal.

Two approaches have been used for this purpose:

- Single pass synchronization: a fresh bunch is injected every time in the storage ring and dumped after exactly one turn.

- MAF window delay scan: a short train of bunches is stored in the ring, the delay parameter of the MAF window is scanned for all BPMs allowing to locate the delay that maximize the strength of the acquired signal.

The "single pass synchronization" provides a valuable tool to cross-check the synchronization on a turn basis. However, due to the short acquisition period (one turn) and the small amount of charge that can be injected each time in the storage ring, this technique suffers from a high noise level and does not allow a precise sub-turn synchronization. On the other hand the "MAF window delay scan" provides a much cleaner and robust measurement, but it is affected by a one turn ambiguity: increasing the MAF delay by one revolution period results exactly in the same measured strength, therefore not allowing for a turn-basis synchronization. The two techniques have been used complementary in order to achieve a proper synchronization on a turn and sub-turn level.

Once the required timing corrections have been defined, the synchronization can be adjusted by acting on different elements along the timing distribution chain.

A first rough timing adjustment is obtained on a per-sector basis by acting on each one of the 16 EVRs. The EVRs allow to introduce a delay in the trigger signal common to all the driven BPMs. Since most of the delay is introduced in the connection between the EVG and the individual EVR of each sector, this per-sector correction takes out most inequalities in the timing distribution network. Instead the fine delay tuning is achieved on a per-BPM basis by adjusting the internal delay of each BPM receiver electronics.

The "single turn synchronization" measurements were acquired by closing a scraper, located immediately downstream of the injection point, this way the beam was stopped exactly after having completed one turn. Figure 5.2 shows the results for the "single pass synchronization". The discrepancy between different BPMs has been reduced to a value below one turn ensuring a synchronization level adequate to proceed with the "MAF window synchronization".

For this purpose a short train of 45 bunches (one tenth of the maximum 448 available buckets) was stored in the ring and a MAF window length of the same length (90 ns) has been configured in each BPM. Figure 5.3 shows the measured

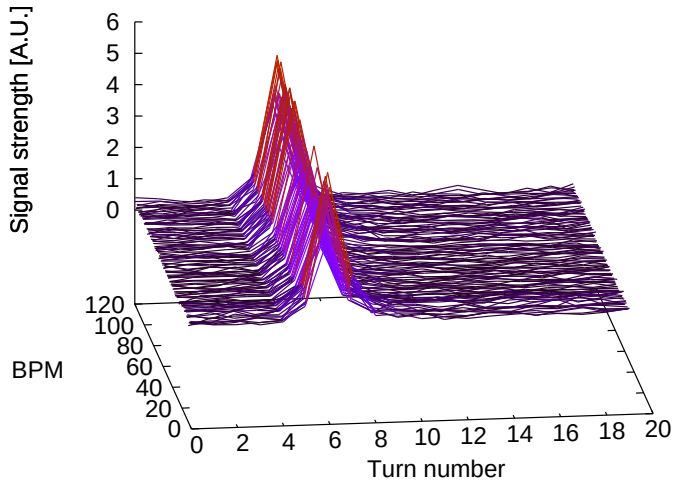

FIGURE 5.2. In the single pass synchronization a fresh train of bunches is injected in the storage ring and dumped after exactly one turn by blocking the beam passage with a scraper. The signal strength, defined as the sum of the strengths measured on the 4 BPM buttons, is plotted as a function of the turn number. The maximum signal strength falls for every BPM at the same turn number, therefore a synchronization better than one turn is guaranteed. Because the measurement was carried out without the MAF filter, the effect of the turn-smearing is visible in the turns following and preceding the maximum, as the signal needs more than one turn to fall to zero.

signal strength as a function of the window delay and the optimum observed delay that has been used for the following measurements.

5.1.2. *Pinger magnet calibration*

In order to excite in a consistent way the betatron motion of a short train of bunches a proper timing between the beam and the pinger is needed. In fact because of the sinusoidal shape of the magnetic pulse of the pinger only a small time interval around the top of the pulse offers an adequately flat profile suitable for a uniform excitation along the whole train length. Furthermore the kick pulse

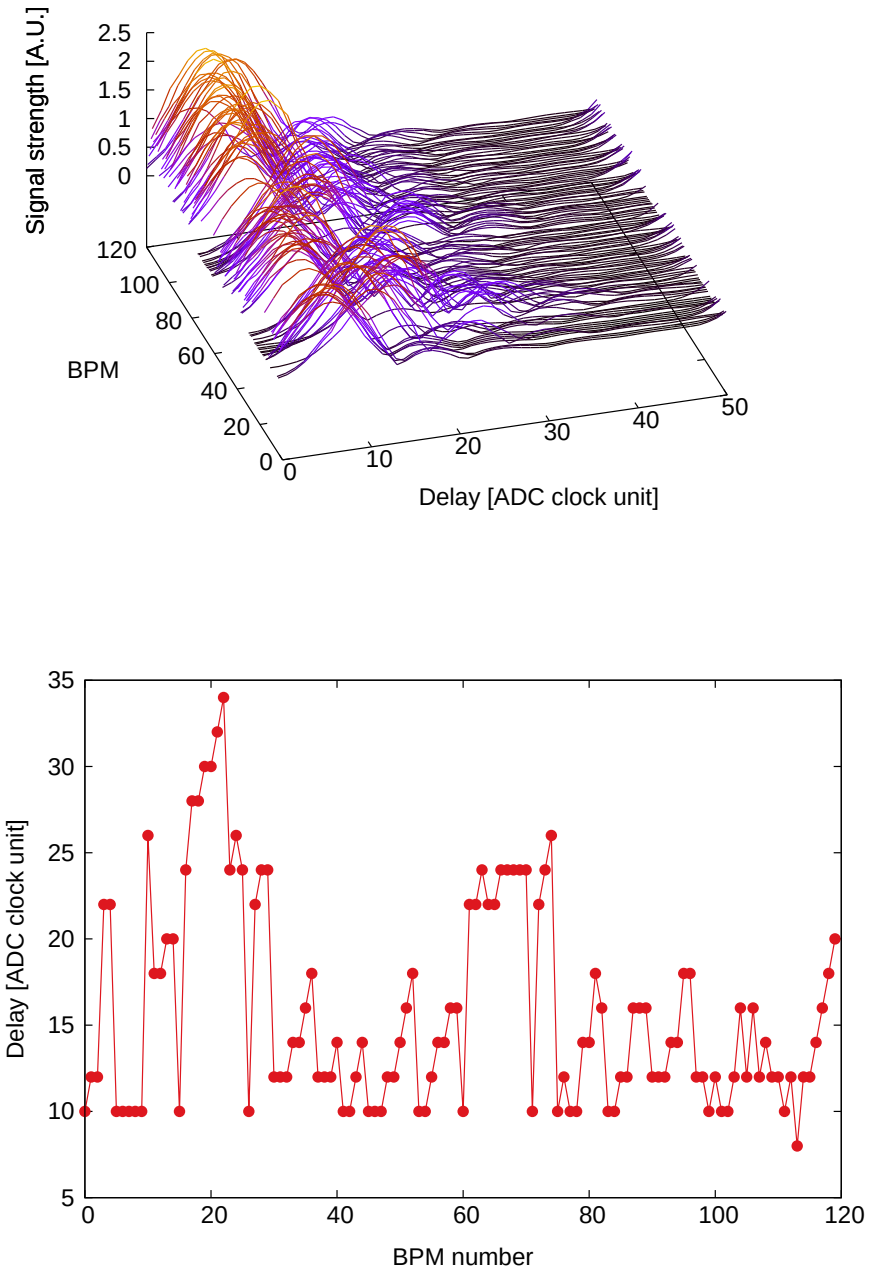

FIGURE 5.3. (Top) the delay of the MAF window has been increased from 0 to 50 units of ADC clock (~ 8 ns) while measuring the sum of the signal strength of each button for each BPM. The first and highest encountered maximum defines the best synchronization, the secondary maxima are due to a partial overlapping of the MAF window and the signal, stretched in time by the band-pass filter in the analog front-end (as discussed in Section 3.3.1). The delay relative to the first maximum is computed for each BPM and taken as the optimum delay value (bottom picture).

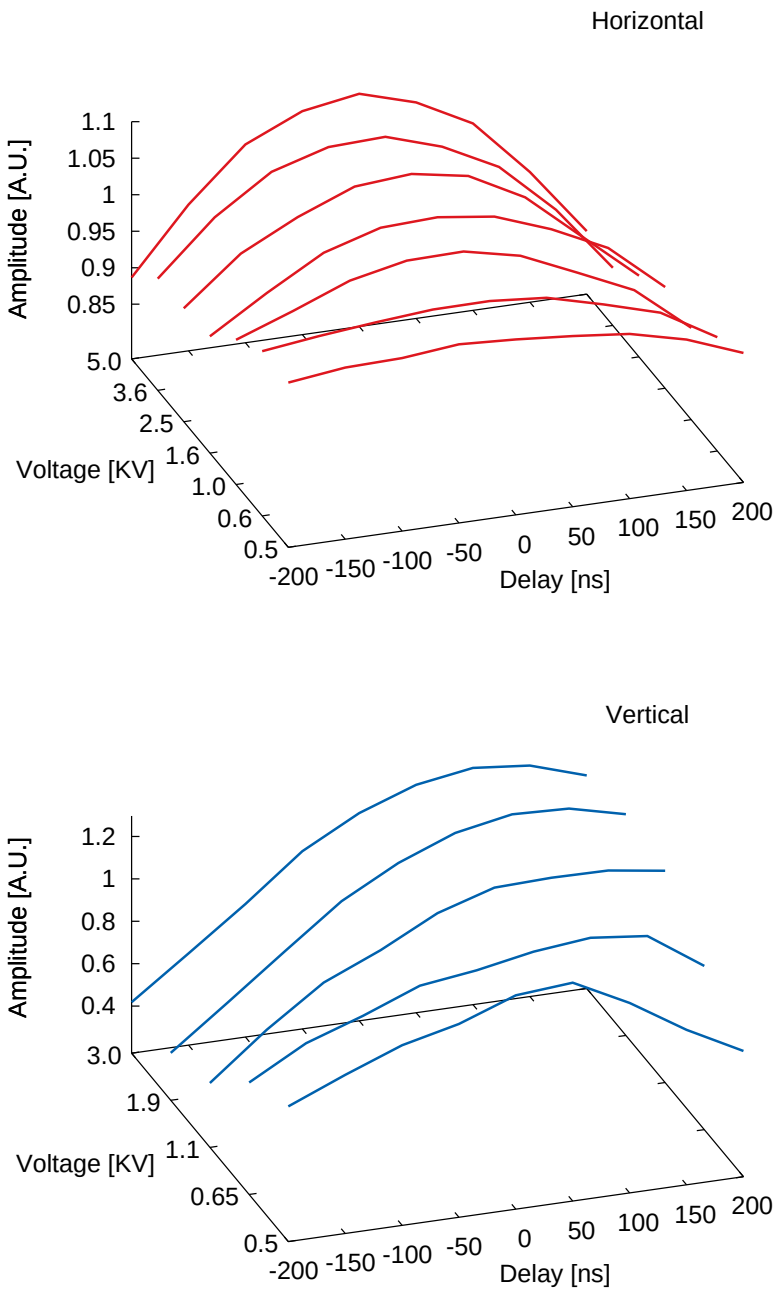

FIGURE 5.4. Pinger delay scan. The timing between beam and pinger is established by scanning the pinger EVR delay and measuring the induced betatron amplitude for each delay.

stretches in time when decreasing its strength, therefore a proper characterization of the pulse temporal properties for different kick strengths is required.

The calibration is obtained by measuring the produced betatron oscillation amplitude as a function of the pinger EVR delay for every working voltage (kick strength). The results of the measurements are presented in Fig. 5.4.

Once established the optimal pinger delay for each voltage, we proceed with a second important calibration: establishing the relation between the pingers voltage and the resulting induced betatron amplitude. The results are shown in Fig. 5.5, where the betatron action averaged over all the BPMs is plotted against the pinger voltage.

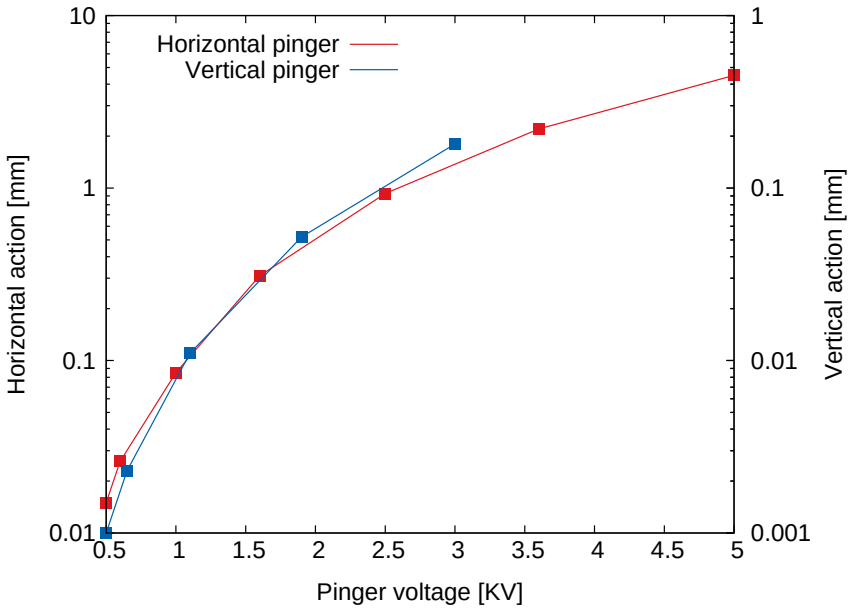

FIGURE 5.5. Excitation amplitude (action) induced by the horizontal and vertical pinger have been measured for different pinger voltages.

5.1.3. *Low chromaticity lattice*

During the standard operation the ALBA storage ring operates with a horizontal and vertical unnormalized chromaticity respectively of +2.0 and +4.5 to avoid the so called head-tail instability. Due to the natural energy spread of the beam, the high value of the chromaticity results in some important limitation to turn-by-turn observations. In fact the BPMs are able to sample the betatron motion as

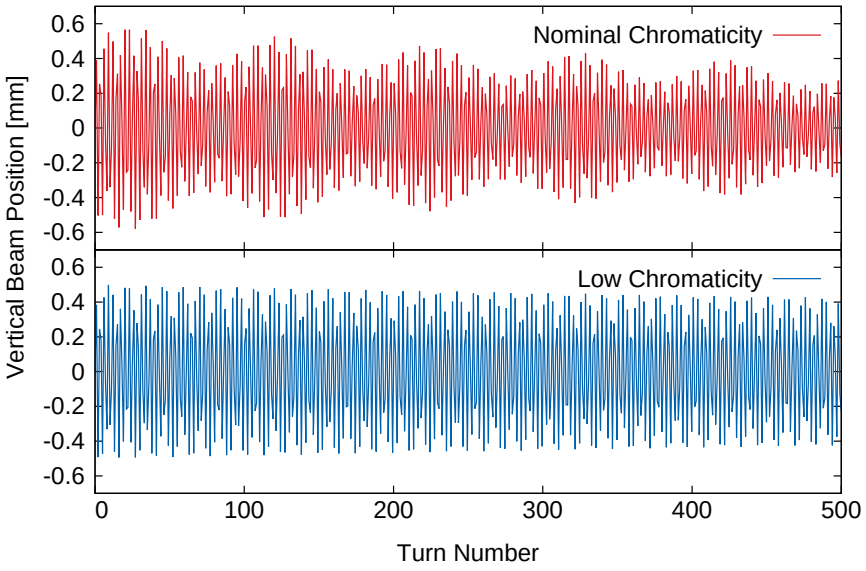

FIGURE 5.6. Turn-by-turn vertical beam position measurements for the standard operation and zero chromaticity lattice. In the standard operation case (top) a fast damping along with the characteristic pulsating amplitude is observed while the zero chromaticity case (bottom) has an almost purely exponential decay.

long as the particles within each bunch move all together in a coherent oscillation, on the other hand the albeit small tune difference produced by the chromaticity, leads to a quick decoherence between the betatron motion of particles of different energy. As a result of the decoherence process the overall bunch motion observed through a BPM does not resemble anymore the one described in Section 1.1.2, showing instead a characteristic pulsating envelope plus an overall faster damping as depicted in Fig. 5.6. Reducing chromaticity to a value as close as possible to zero is an easy work around to solve the problem at the root. Moreover the limited amount of charge used during these measurements does not require a strong positive chromaticity in order to maintain the beam stability. Once corrected the sextupoles to produce zero chromaticity the artifacts (envelope modulation and fast damping) introduced by the decoherence process disappear. A visual inspection of

the acquired turn-by-turn beam position from one BPM confirms the correct tuning of the lattice (Fig. 5.6).

5.2. SOLEIL setup

The SOLEIL storage ring is also equipped with two pingers [**31**] (one for the vertical and one for the horizontal plane) and 122 BPMs with "Libera Electron" receiver electronics. Unlike the "Libera brilliance" BPM receivers used in the ALBA storage ring, these older units do not allow to use a moving average filter as was done at ALBA. On the other hand, since the demodulation chain of the BPM has a bandwidth smaller than the revolution frequency of the beam, the turn mixing effect discussed in chapter 3.3.1 is an issue that has to be addressed.

5.2.1. *BPM turn mixing*

The strategy developed at SOLEIL and Diamond light sources in the past years [**27, 10**] to compensate for the turn mixing effect is based on a deconvolution approach where the response of the BPMs to a single pass of a bunch (impulse response) is measured and removed from the turn-by-turn data with a deconvolution.

The BPMs impulse response was characterized with an approach similar to the one used to achieve the single pass synchronization at ALBA (Fig. 5.2): a scraper, located immediately before the injection point was closed in order to stop the beam exactly after having completed one turn making it possible to acquire the single turn response of each BPMs. Figure 5.7 shows a typical signal measured for one BPM. The acquired impulse response was then used to compute a filter that cancel out the effect produced by the BPM internal filtering. First, the Fourier transform of the impulse response is calculated. Then the impulse response spectrum is inverted and transformed again to the time domain. Finally the obtained function is convoluted with the measured turn-by-turn data.

Such procedure provides data free of the turn mixing effect as long as the BPM impulse response has been measured correctly and no time fluctuation in the BPM behavior is present. While the first condition is met by averaging over many single pass acquisitions, the last one depends solely on the BPM stability.

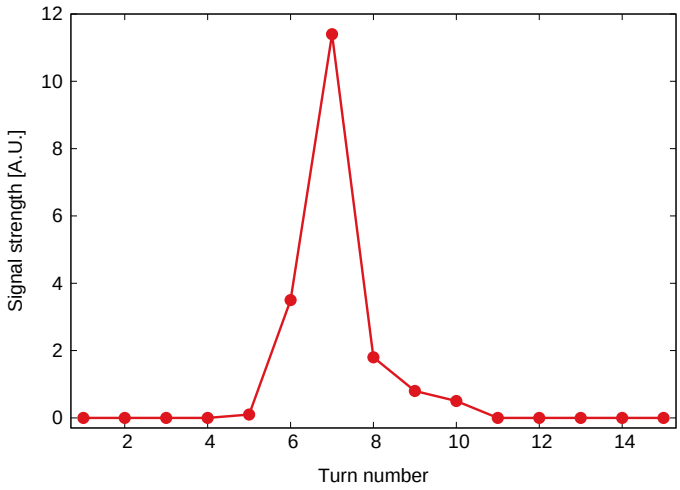

FIGURE 5.7. Impulse response for one BPM measured in the SOLEIL storage ring. The turn mixing effect is evident and extends to around 6 consecutive turns.

CHAPTER 6

Turn-by-turn measurements analysis and results

As discussed in Section 1.1.2 at small amplitudes the betatron oscillation is fully determined on each transverse plane by a set of 3 parameters: a frequency (tune), an amplitude (betatron-amplitude) and a phase (betatron-phase). Each one of the 3 parameters can be deduced from turn-by-turn beam position measurements by means of a spectral analysis as described in Appendix A. Since the betatron-amplitude and betatron-phase are both functions that depends on the location of the observation point respect to the lattice, it is possible to combine the information gathered from many BPMs in order to obtain a detailed picture of the storage ring optics. On the contrary the tune, being a constant of motion does not provide any position dependent information but still represents a very robust tool to confirm the functionality of the experimental apparatus and to investigate the overall stability of the storage ring lattice.

In the following sections the results of the turn-by-turn beam position measurements carried out at the ALBA and SOLEIL storage rings in the linear regime are presented: first of all the tune measurements have been employed to confirm the functionality of the experimental setup and to verify the storage ring stability next the analysis has been extended also to the betatron amplitude and betatron phase.

6.1. ALBA turn-by-turn measurements

6.1.1. *Tune: measurements and sources of error*

In a properly functioning setup the measurement of the betatron tune, realized at different locations around the storage ring should provide the same result, within the experimental uncertainty.

The measurement was carried out by exciting the beam with the horizontal or the vertical pinger at small betatron amplitude in order to make negligible the

non-linear optics effects. A maximum betatron amplitude of $\sim$ 0.6 mm and $\sim$ 0.9 mm respectively for the horizontal and vertical plane (that corresponds to an action J_x=0.22 µm and J_y=0.37 µm or to an average amplitude of $\sim$ 0.5 mm for both planes) was chosen. The whole process was repeated for 100 acquisitions in order to obtain a sufficient statistics to study the repeatibility of the measurement and the stability of the storage ring optics. During each acquisition the beam is excited with the pinger in both planes and the beam position recorded by all the 120 BPMs for 1000 consecutive turns, allowing for a very precise reconstruction of the tune frequency. Once the data were transferred from the BPMs to the control computer the spectral analysis described in Appendix A was performed and the tune frequencies extrapolated.

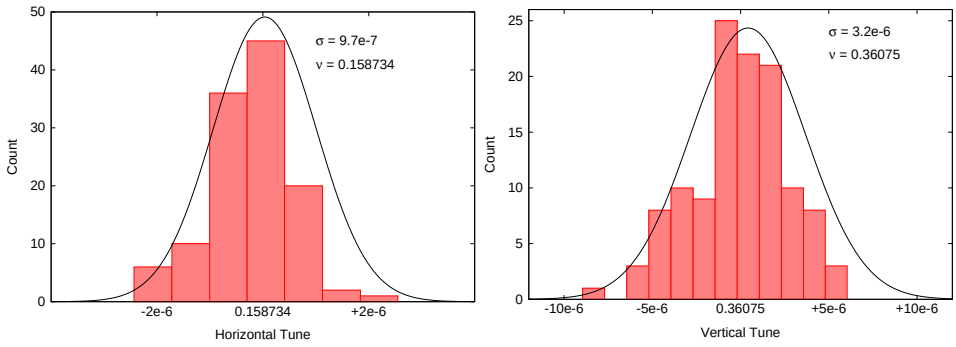

FIGURE 6.1. Histogram of the horizontal and vertical tune measured by the 120 BPMs one acquisition. A Gaussian fit of the experimental data is shown along with the value of the sigma and mean value for both planes.

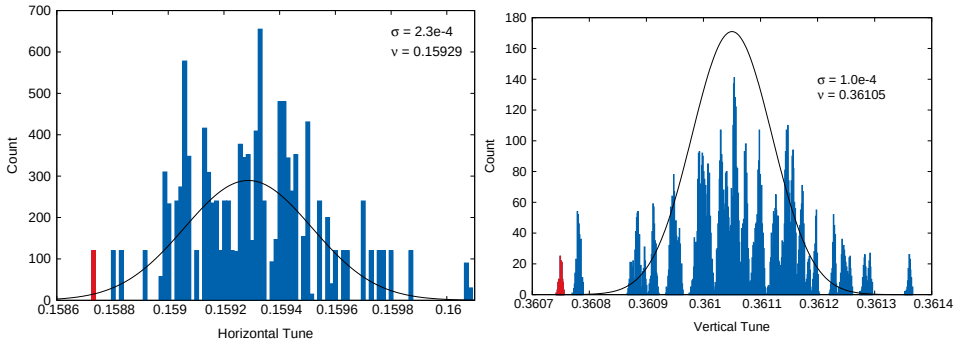

FIGURE 6.2. Histogram of the horizontal and vertical tune measured by the 120 BPMs during 100 acquisition. A Gaussian fit of the experimental data is shown along with the value of the sigma and mean value for both planes. The red bins identify the same acquisition shown in Fig. 6.1.

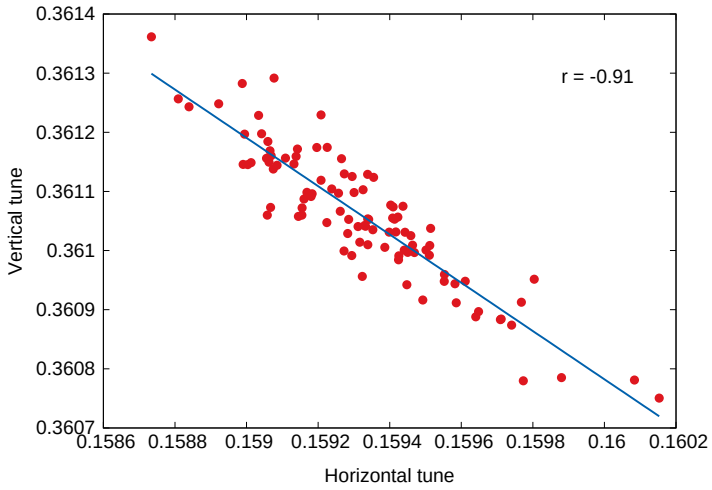

FIGURE 6.3. Correlation plot and Pearson correlation coefficient (r) for the horizontal and vertical tune shift. The clear anticorrelation manifests the presence of one or more quadrupolar error sources.

Figure 6.1 shows the histogram of the measured vertical and horizontal tunes obtained for a set of 100 acquisitions. The variation among BPMs is within $1 \cdot 10^{-6}$ and $3 \cdot 10^{-6}$ respectively for the horizontal and vertical planes.

On the other hand an overall tune fluctuation common to all the BPMs is observed among different sets of acquisitions (Fig. 6.2).

A tune change measured consistently by all BPMs suggests the presence of a real fluctuation of the optics of the lattice. In fact since each BPM measures independently of the others, there is no other reason to expect a common error.

Equation 1.67 shows how the presence of a quadrupolar error induces a tune shift on both planes with opposite sign, independently of the perturbation polarity and beta values. As a consequence the presence of an anticorrelation (correlation with negative slope) between horizontal and vertical tune variations represents the signature of a time varying quadrupolar error.

Figure 6.3 shows that a correlation is indeed present confirming the hypothesis.

The nature of such an error has now to be investigated. Assuming the source is actually a magnetic element of the storage ring, most likely one or more quadrupoles

being the elements with the stronger impact on the machine tune, we subdivide the possible causes in two categories:

- Drifts: for example produced by temperature change of a magnet which produce an alteration of the magnetic field.
- Magnetic field noise: induced by electrical noise in magnets power supplies.

In order to identify the presence of drifts both tunes were plotted against the time and the correlation between tune and time calculated. As it appears from Fig. 6.4 no correlation is observed, therefore the hypothesis of a drift has to be excluded.

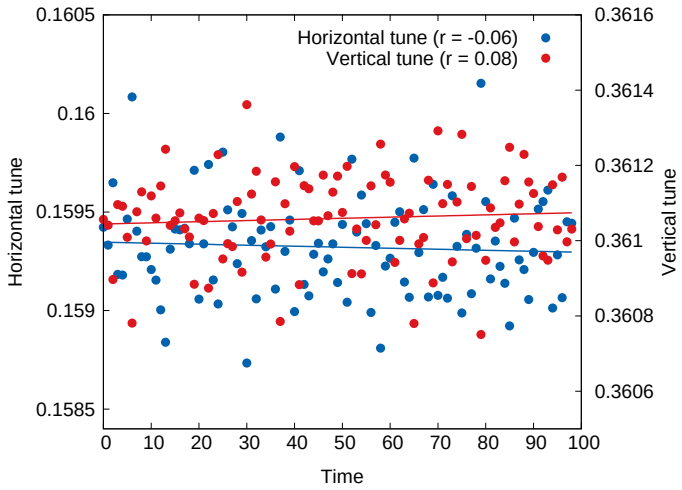

FIGURE 6.4. Correlation plot and Pearson correlation coefficient (r) of the tune shift as a function of time for the horizontal and vertical plane. The absence of a correlation between tunes and time shows that no major magnets drift is present.

The presence of a certain amount of electrical noise in the current fed to the quadrupoles is instead expected. To estimate the effect induced on the tunes we proceed by calculating the effect produced by the presence of electrical noise in a quadrupole with strength equal to the average of the quadrupoles strength. Equation 1.67 provides the tune shift induced by a quadrupolar error source, that for a source with strength $\bar{\sigma}_K$ equal to the average strength and situated at a location

with beta $\bar{\beta}$ equal to beta value averaged over all the quadrupoles location yields:

$$\bar{\sigma}_Q = \frac{\bar{\beta} \cdot \bar{\sigma}_K}{4\pi} \tag{6.1}$$

Assuming the noise affecting each quadrupole uncorrelated with respect to the others, the overall tune fluctuation induced by N quadrupoles is $\bar{\sigma}_Q\sqrt{N}$. Therefore in the case of the ALBA storage ring, where a typical noise level of 10ppm [**38**] is specified for the quadrupoles power supplies, an overall tune fluctuation of $1.5 \cdot 10^{-4}$ and $1.5 \cdot 10^{-4}$ respectively for the horizontal and vertical plane is expected.

Such lattice fluctuations, as it will be more evident in the next sections, represent one of the most important issues for turn-by-turn measurements that, being by their own nature quick, are sensitive to such fast transients.

To further investigate the temporal evolution of the tune that eventually lead to the observed tune jitter, we decided to carry out another test: a very long acquisition of $2.5 \cdot 10^5$ turns, equivalent to $\sim$250 ms was measured with one BPM, the turn by turn data were sliced in short portions of 1000 turns each and analyzed in order to get a picture of the temporal evolution of the tune. Since the betatron motion excited with the pinger can not last for such long time a different strategy was required to achieve such a long tune observation. The necessary excitation was produced on the vertical plane by reducing the chromaticity enough to observe a vertical transverse beam instability.

The betatron oscillation induced by the instability is generally very difficult to control and therefore not a recommendable approach to carry out turn-by-turn measurement. Nevertheless the quality of the acquired data was good enough to obtain a complete picture of the vertical tune spectrum from 8 Hz to 550 Hz.

The spectrum in Fig. 6.5 shows two clear peaks at 100 Hz and 300 Hz, this are suspiciously related with the 50 Hz line frequency and are typically produced by single phase and three phases rectifiers as the one used in magnets power supplies. On the other hand the integral of the spectrum shows that the two peaks take into account only for a small fraction of the overall noise where instead a rather constant floor provides the strongest contribution. Such result suggest that the overall power

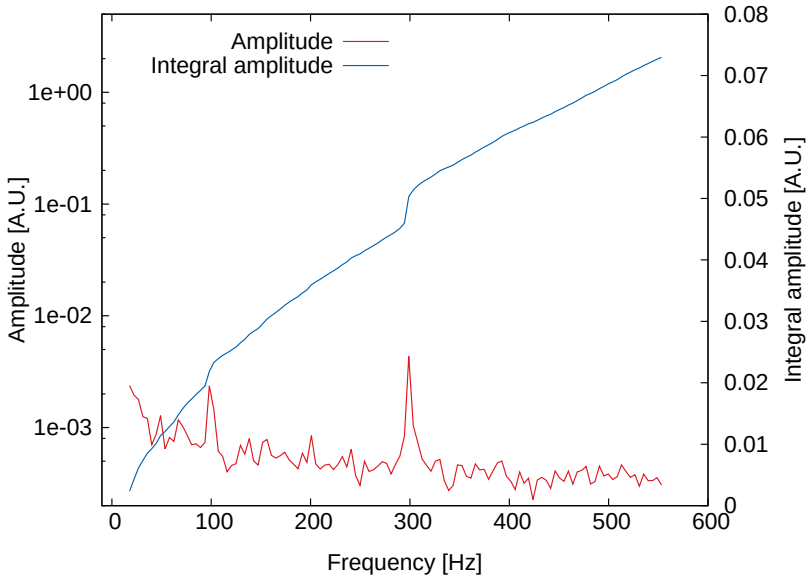

FIGURE 6.5. Vertical tune spectrum. The spectrum (red) shows two main peaks at 100 Hz and 300 Hz above a constant floor that provides the strongest contribution as shown by the spectrum integral (blue). The plot has been obtained by averaging the spectrum of 30 acquisitions.

supplies performance is as specified and no major leak or noise driving source is affecting the accelerator.

6.1.2. *Betatron amplitude*

Also the betatron motion amplitude provides some important information on the storage ring optics. Equation 1.4 shows that an intimate relation exists between the function β and the motion amplitude A:

$$\beta_i = \frac{A_i^2}{J} \tag{6.2}$$

where J represents the kick strength and the index i identifies the BPM where the observation is carried out.

Unfortunately a reliable estimation of the kick strength J is not easily accessible. In fact the pinger shows a kick repeatability of around 1%, therefore limiting to this level the precision to estimate β_i. To workaround the problem we have

introduced a new normalization of the β-function $\bar{\beta}$ defined as:

$$\bar{\beta}_i = \frac{\beta_i}{\sum_{i=0}^{N} \beta_i} N \tag{6.3}$$

where N represents the total number of BPMs. By enforcing a normalization constraint the dependency on any scale factor common to all BPMs is eliminated. The same way the $\bar{\beta}$-function is obtained from the motion amplitude as:

$$\bar{\beta}_i = \frac{A_i^2}{\sum_{i=0}^{N} A_i^2} N \tag{6.4}$$

allowing to compare experimental observations to the theoretical storage ring model. It is important to note that by applying such renormalization to the experimental data, a strong deviation in one BPM induces a systematic error in the evaluation of $\bar{\beta}_i$ at all the other locations, limiting such technique to the case of small optics error only. Furthermore the presence of malfunctioning BPMs now represents a significant danger since a single outlier BPM can produce a significant deviation in the whole analysis, therefore a particular care is required in order to locate faulty BPMs.

The results of the $\bar{\beta}_i$ measurement in the ALBA storage ring is plotted in Fig. 6.6. The experimental observations are compared against the design model of the storage ring resulting in an overall r.m.s. discrepancy (β-beat) between design model and measurements of 2.0% and 2.5% respectively for the horizontal and vertical planes, in agreement with what observed in similar experiments [**29, 8, 21**].

6.1.3. *Phase advance*

Another useful observable accessible from turn by turn measurements is the betatron phase. Since the betatron phase is defined up to an overall phase, depending on the initial motion conditions (determined by the pinger timing and location), it is preferable to introduce a new quantity, the phase advance $\Delta\psi^{\dagger}(s_n)$, defined as the difference of the betatron phase observed by two neighbor BPMs:

$$\psi^{\dagger}(s_n) = \psi(s_n) - \psi(s_{n+1}). \tag{6.5}$$

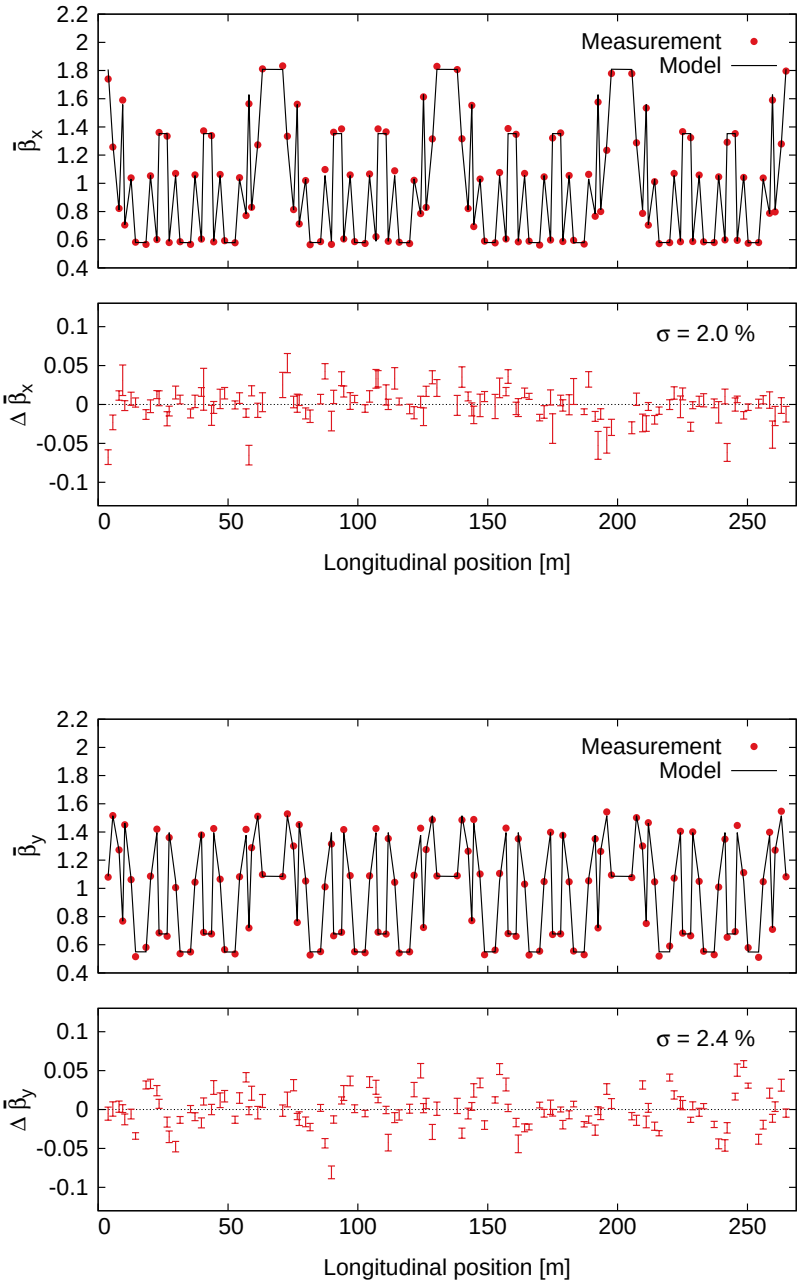

FIGURE 6.6. Comparison of the measured and model horizontal and vertical $\bar{\beta}$ at the BPMs in the ALBA storage ring. The measured value of $\bar{\beta}$ (red dots) is compared against the nominal value of the ALBA storage ring model (black solid line). The discrepancy (beta-beat) between the two along with the acquisition to acquisition fluctuation is also shown (red error bars).

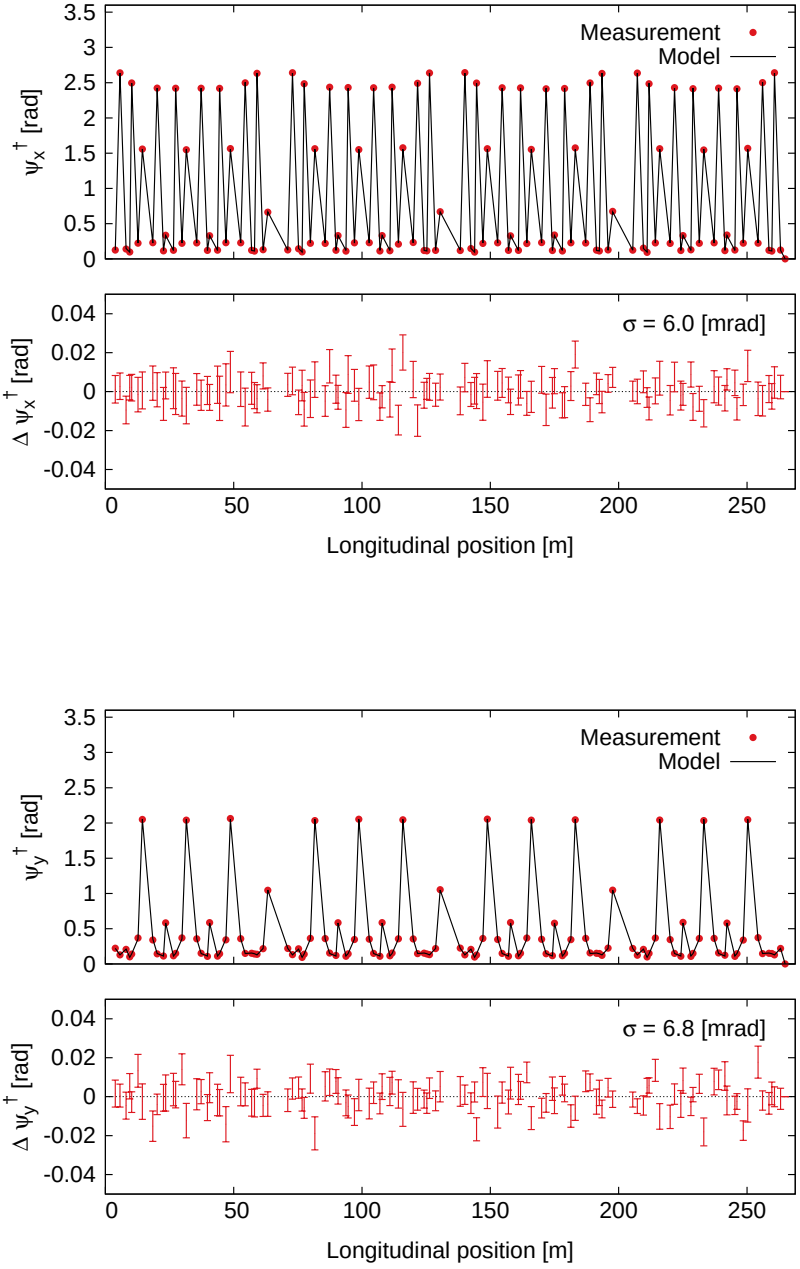

FIGURE 6.7. Horizontal and vertical $\psi^\dagger$ measurement in the ALBA storage ring. The measured value of $\psi^\dagger$ (red dots) is compared against the nominal value of the ALBA storage ring model (black solid line). The discrepancy between the two along with the acquisition to acquisition fluctuation is also shown (red error bars).

Where the index n identifies the BPM. Because $\Delta\psi^{\dagger}(s_n)$ is obtained from the difference of two betatron phase observations, any initial phase offset common to all BPMs is canceled and therefore the dependency on the initial condition removed.

Figure 6.7 shows the results of the phase advance measurement in the ALBA storage ring. The experimental observations are compared against the nominal model of the storage ring showing an overall r.m.s. discrepancy "phase-beating" between model and measurements of 6.0 mrad and 6.8 mrad respectively for the horizontal and vertical planes. Also in this case the observed disagreement compares well with similar experiments [**8, 21**].

6.1.4. *Further measurement and analysis optimization*

Up to now the choice of the excitation amplitude and the number of turns considered in the analysis has been set solely on the basis of a rough estimation. On the other hand a methodical study of the effect produced by changing this two parameters is important to understand the limit of validity of the measurement and to optimize the analysis.

A high excitation amplitude is desirable in order to maximize the beam excursion and therefore to reduce the measurements uncertainty, on the other hand the validity of the analysis carried out in Section 1.1.2 is limited to small excitation amplitude, where non-linear effects can be neglected.

The results of the $\bar{\beta}$ and $\psi^{\dagger}$ measurements for different amplitudes are plotted in Fig. 6.8, it is evident how an increase in the kick strength produces a distortion of the observed $\bar{\beta}$ and $\psi^{\dagger}$. Choosing the best working condition is matter of defining the required measurement precision and consequently fix a kick strength producing a distortion lower than the fixed limit.

The precision of the analysis presented in Appendix A is strongly dependent on the number of acquired turns: a high number of turns is generally preferable. On the other hand because of the natural damping of the betatron motion, increasing the number of turns above a certain level does not produce any noticeable improvement, while resulting in a higher load on the BPM network due to the increased data transfer. In fact, since the data transfer is achieved on a network shared between many different nodes, an overall erratic behavior was observed when dealing with

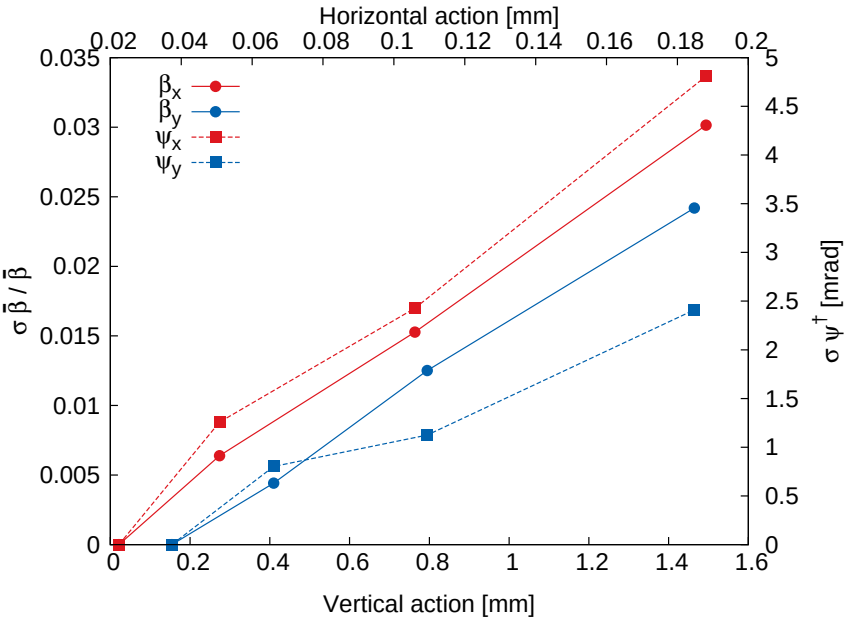

FIGURE 6.8. Variation of $\bar{\beta}$ and $\psi^{\dagger}$ with the kick strength. The $\bar{\beta}$ and $\psi^{\dagger}$ measured for the smallest kick strength has been used as a reference. The r.m.s. of the difference between the reference case and the measurements with higher kick strength is plotted against the kick strength.

heavy data transfers. The experience showed that to measure consistently up to 500 consecutive acquisitions the number of turns has to be kept below 500.

The results of the $\bar{\beta}$ and $\psi^{\dagger}$ observed when analyzing the same acquisition using different number of turns are presented in Fig. 6.9.

With 500 turns a precision better than 0.5% is observed for the $\bar{\beta}$ measurements and 0.5 mrad for $\psi^{\dagger}$, values that are below the optics fluctuations due to the quadrupoles magnet induced noise. Therefore there is no advantage in increasing the number of turns used in the analysis above 500 whenever measuring average properties of the storage ring optics.

6.2. SOLEIL turn-by-turn measurements

A similar set of measurements for the tune, $\bar{\beta}$ and $\psi^{\dagger}$ as the one acquired at ALBA was also repeated in the case of SOLEIL. Figure 6.10 shows the results for the vertical and horizontal tunes measurement, also in this case a certain amount

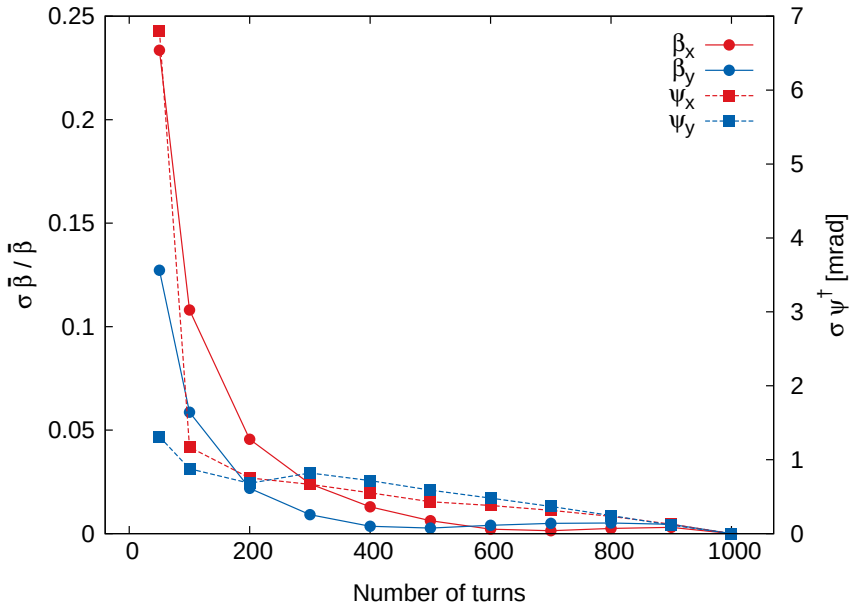

FIGURE 6.9. Variation of $\bar{\beta}$ and $\psi^{\dagger}$ with the number of turns used in the analysis. The $\bar{\beta}$ and $\psi^{\dagger}$ obtained from the analysis with 1000 turns has been used as a reference. The r.m.s. of the difference between the 1000 turns analysis and any other is plotted against the used number of turns.

of tune jitter was visible, even if around a half of what has been observed in the case of ALBA.

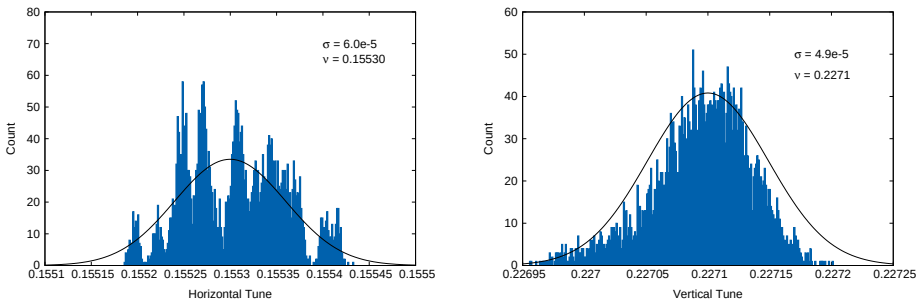

FIGURE 6.10. Histogram of the horizontal and vertical tune measured by 120 BPMs during 100 acquisition. A gaussian fit of the experimental data is shown along with the value of the sigma and average value for both planes.

$\bar{\beta}$ and $\psi^{\dagger}$ measurements (Fig. 6.11 and Fig. 6.12) show a disagreement with respect to the theoretical value similar to what observed at ALBA, on the other hand the acquisition to acquisition fluctuations appear to be much higher possibly because of the older BPM electronics employed in the SOLEIL storage ring.

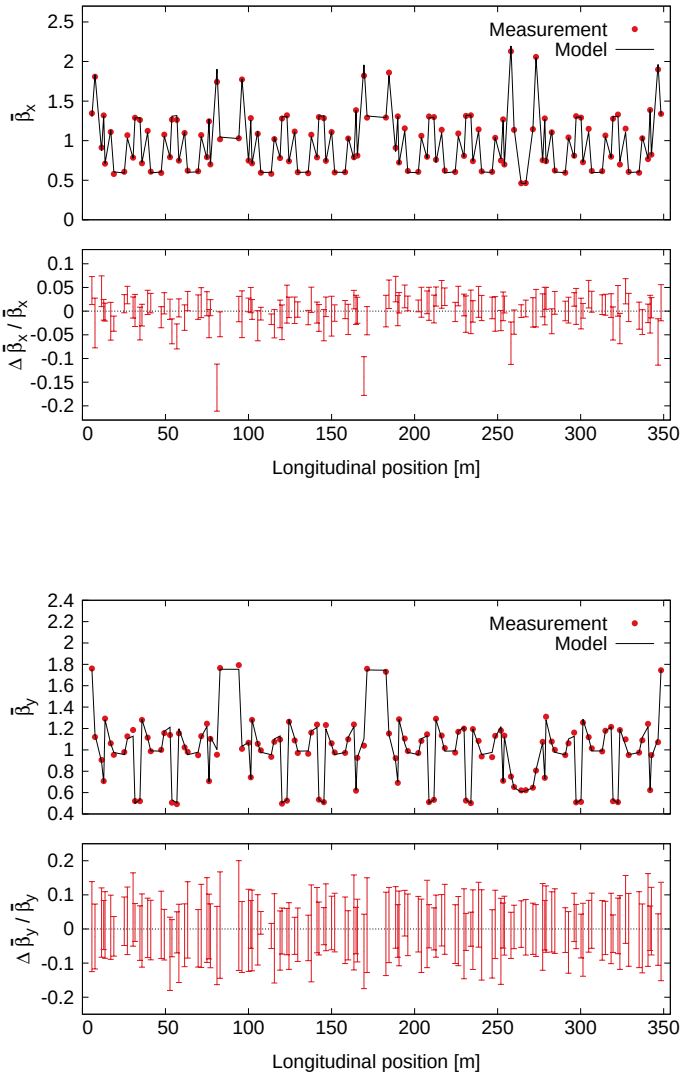

FIGURE 6.11. Horizontal and vertical $\bar{\beta}$ measurement in the SOLEIL storage ring. The measured value of $\bar{\beta}$ (red dots) is compared against the nominal value of the SOLEIL storage ring model (black solid line). The discrepancy between the two along with the acquisition to acquisition fluctuation is also shown (red error bars). An overall $\bar{\beta}$-beat of 2.3% and 2.2% was observed respectively for the horizontal and vertical plane.

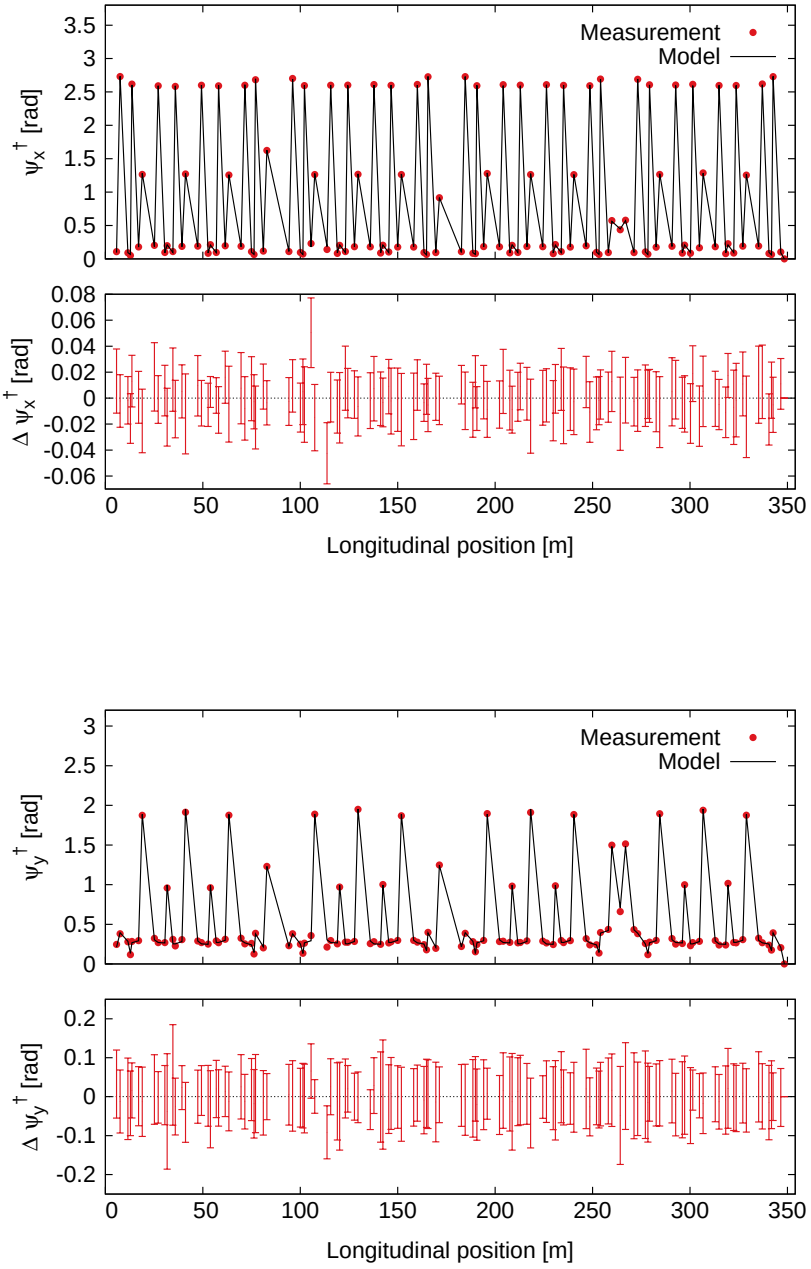

FIGURE 6.12. Horizontal and vertical $\psi^\dagger$ measurement in the SOLEIL storage ring. The measured value of $\psi^\dagger$ (red dots) is compared against the nominal value of the SOLEIL storage ring model (black solid line). The discrepancy between the two along with the acquisition to acquisition fluctuation is also shown (red error bars). An overall phase-beat of 10 mrad and 19 mrad was observed respectively for the horizontal and vertical plane.

CHAPTER 7

Measurement and correction of lattice errors

In the previous sections the setup to carry out turn-by-turn measurements in the ALBA and SOLEIL storage rings has been presented and demonstrated, in this chapter instead the same analysis is used as the base to characterize the presence of single sources of gradient error in the lattice of a storage ring. In a first test single gradient error sources has been introduced on purpose in the lattice of ALBA and SOLEIL, hence turn-by-turn measurements have been used to characterize the produced error distortion. Once confirmed the validity of the measurements against the theoretical expectations, the same data have been used to infer a complete lattice error model.

The analysis is then extended to coupling and sextupolar errors. For this purpose the same approach employed for the gradient errors characterization is applied, but this time introducing skew quadrupolar or sextupolar error sources in the lattice.

Such analysis is of particular interest since it represents the first step to attempt a complete linear and non-linear lattice correction.

7.1. Linear optics corrections

As discussed in Section 1.2.5 the presence of a quadrupolar error source in the magnetic lattice results in an alteration of the $\bar{\beta}$ and $\psi^{\dagger}$ functions. Such variation depends on the strength and position of the error sources (Eqs. 1.75 and 1.77), turning $\bar{\beta}$ and $\psi^{\dagger}$ measurements into a suitable tool to characterize magnetic gradient errors in a storage ring.

To assess the sensitivity of turn-by-turn measurements to quadrupolar errors, we conducted a series of experiments where known gradient error sources were introduced on purpose in the magnetic lattice. Two quadrupoles, QH01 and QH08 (see Figs. 2.3 and 2.4), were detuned in order to introduce, in a controlled manner

the error. First the current in QH01 was decreased in steps up to -1% of the nominal value and next also the current in QH08 was reduced in steps up to -1%. For each quadrupole configuration turn-by-turn beam position data were acquired and $\bar{\beta}$ and $\psi^{\dagger}$ derived following the same procedure described in the previous chapter. Hence the $\bar{\beta}$ and $\psi^{\dagger}$ variations have been calculated as:

$$\begin{aligned} \Delta\bar{\beta}_{x,y} &= \frac{\bar{\beta}^{0}_{x,y} - \bar{\beta}^{n}_{x,y}}{\bar{\beta}^{0}_{x,y}} \\ \Delta\psi^{\dagger}_{x,y} &= \psi^{\dagger 0}_{x,y} - \psi^{\dagger n}_{x,y}, \end{aligned} \tag{7.1}$$

where the superscript 0 identifies the reference measurement carried out before having introduced any quadrupolar error, while the superscript n refers to any other configuration where an error in QH01 and QH08 was present.

In a first test the measurements of $\Delta\bar{\beta}_{x,y}$ and $\Delta\psi^{\dagger}_{x,y}$, for a decrease of current in QH01 of -1% while no change was applied to QH08, have been compared with the value predicted by the theory. The results, presented in Fig. 7.1, agree with the theoretical predictions, only a minor disagreement is visible in the case of $\Delta\bar{\beta}_{x}$.

The next step consists in trying to characterize the gradient error from the same measurements. This is achieved by fitting an error model in order to reproduce the observed $\Delta\bar{\beta}_{x,y}$, $\Delta\psi^{\dagger}_{x,y}$: a set of error sources is assumed, in this case located at QH01 and QH08 only, and their strength is optimized in order to reproduce the measured observables ($\Delta\bar{\beta}_{x,y}$ and $\Delta\psi^{\dagger}_{x,y}$).

To simplify the fitting procedure we take advantage of the linear response of the optical functions to small gradient errors. We proceed by evaluating the theoretical value of $\Delta\bar{\beta}_{x,y}$ and $\Delta\psi^{\dagger}_{x,y}$ The results are arranged in a rectangular $m \times n$ matrix M known as the "beta and phase to quadrupole response-matrix", where produced by a quadrupole of unitary strength located at each error source (in this case QH01 or QH08). every column represents the deviation of the observables of interest ($\Delta\bar{\beta}_{x,y}$, $\Delta\psi^{\dagger}_{x,y}$ or a combination of the two) sampled at the position of the m BPMs, for each one of the n error sources. As it is shown by Eqs. 1.64 and 1.71, the response matrix provides a picture of the errors footprint in terms of the produced optical function distortions and contains information that can be exploited to carry out the fit of a lattice error model. In fact, because of the linear dependency of $\Delta\bar{\beta}_{x,y}$

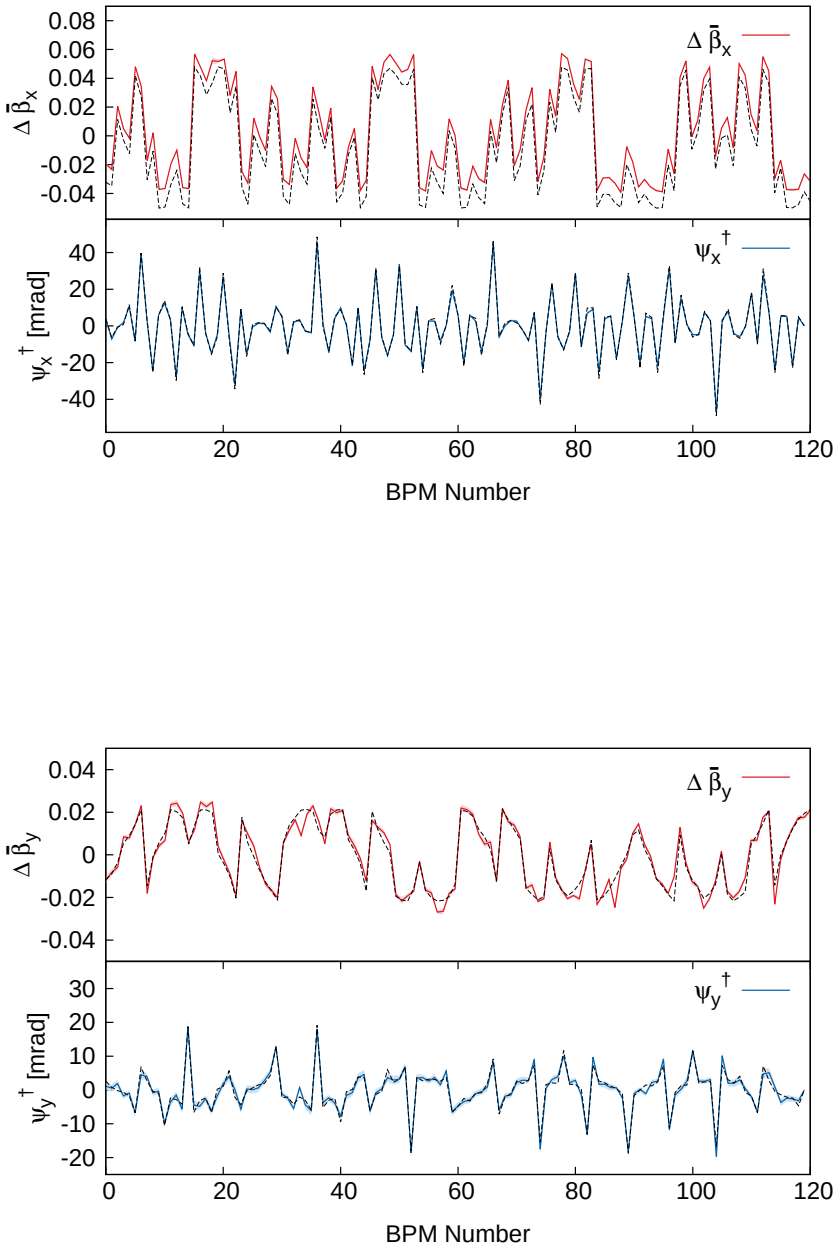

FIGURE 7.1. Horizontal and vertical $\Delta\bar{\beta}_{x,y}$ and $\Delta\psi^{\dagger}_{x,y}$ observed for a change of 1.0% in QH01. The solid lines represent the one-sigma uncertainty due to acquisition to acquisition fluctuations, while the dashed lines are the expected theoretical values. The measurement consists of 100 acquisitions that have been averaged in order to reduce the noise. The overall fluctuation induced by the noise after the averaging process is too small to be appreciable on the plot.

and $\Delta\psi^{\dagger}_{x,y}$ on the errors strength, the effect of an arbitrary configuration of errors can be calculated as:

$$\vec{\Delta} = M \cdot \vec{E}, \tag{7.2}$$

where the entries of the vector $\vec{E}$ represent the strength of each error source and $\vec{\Delta}$ the observables of interest ($\Delta\bar{\beta}_{x,y}$, $\Delta\psi^{\dagger}_{x,y}$ or a combination of the two). Therefore, given an experimental observation $\vec{\Delta}^{\sharp}$ of the vector $\vec{\Delta}$, we can calculate the strength of each error source as:

$$\vec{E}^{\sharp} = M^{-1} \cdot \vec{\Delta}^{\sharp}. \tag{7.3}$$

Since the response matrix M in general is not square or full rank, the system of linear equations (Eq. 7.2) lacks a unique solution and a pseudoinverse matrix M^{-1} has to be used to compute a "best fit" (in the least squares sense) solution. A recipe to calculate M^{-1} is provided by the singular value decomposition, where a rectangular $m \times n$ matrix M is factorized as:

$$M = U\Sigma V^{*}, \tag{7.4}$$

with U an $m \times m$ unitary matrix, Σ a diagonal $m \times n$ matrix with non-negative real numbers on the diagonal known as the singular values and V an $n \times n$ unitary matrix. Given the previous factorization of M it can be shown that the generalized inverse matrix M^{-1} (that satisfy the condition $MM^{-1}M = M$) is:

$$M^{-1} = V\Sigma^{-1}U^{*}. \tag{7.5}$$

From a practical point of view the decomposition of Eq. 7.4 can be obtained with several different numerical methods, in this case the QR algorithm [**22**] implemented in the LAPACK computer library [**4**] was used.

In the first instance four independent fits have been performed analyzing separately $\Delta\bar{\beta}_x$, $\Delta\bar{\beta}_y$, $\Delta\psi^{\dagger}_x$ and $\Delta\psi^{\dagger}_y$. A comprehensive comparison of the results is shown in Figs. 7.2 and 7.3. The level of accuracy of the results is similar for $\Delta\bar{\beta}_{x,y}$ and $\Delta\psi^{\dagger}_{x,y}$ and regardless of the plane. While a minor deviation on the estimation of the strength of QH01, compatible with the acquisition to acquisition

fluctuation noise, is shown in every measurement, this is not the case for QH08 where a constant deviation (around 15%) is encountered. Being independent of the measurement approach, the discrepancy suggests a miscalibration of the magnet strength or a deviation in the evaluation of the beta functions at the magnet location. The results point out that, at this level the measurements to be fitted are equivalent and no superiority of one parameter (betatron amplitude or phase) over the other is shown.

Having proved the functionality of the method, we proceed to extend the analysis to the full lattice, including all the quadrupoles in the storage ring. In order to gather together the information provided by the amplitude and phase of the betatron oscillation and extend the fitting process to $\Delta\bar{\beta}_{x,y}$ and $\Delta\psi^{\dagger}_{x,y}$ measurements at the same time, we define a new complex quantity $\vec{\zeta}$ to replace $\vec{\Delta}$ in Eq. 7.3:

$$\zeta^{i}_{x,y} = \bar{\beta}^{i}_{x,y} \cdot e^{\imath\psi^{i}_{x,y}}, \tag{7.6}$$

where i identifies the BPM. Moreover, by joining together the vectors $\vec{\zeta}_x$ and $\vec{\zeta}_y$ in one single vector it is possible to extend the fit to the full set of observables.

Unfortunately the straight application of the previous method to the full lattice does not provide any useful results, even by extending the fit to the whole set of observables by means of the previously defined complex variable $\vec{\zeta}$. As it is visible from Fig. 7.4a the fit is characterized by a very high level of uncertainty that completely submerge the signal, making the method useless in practice.

The reason for such poor result is to be attributed to the limited precision of the experimental observations together with the high number of quadrupoles included in the fit. In fact, since two closely located error sources produce a very similar beta-beat and phase-beat pattern, the presence of an increased number of near quadrupoles makes it hard to distinguish correctly the sources of error. Furthermore two close-by error sources with equal strength but opposite sign produce an effect that cancels out giving rise to an ambiguous condition where multiple fake errors with opposite sign can be erroneously fitted still being compatible with the measured data.

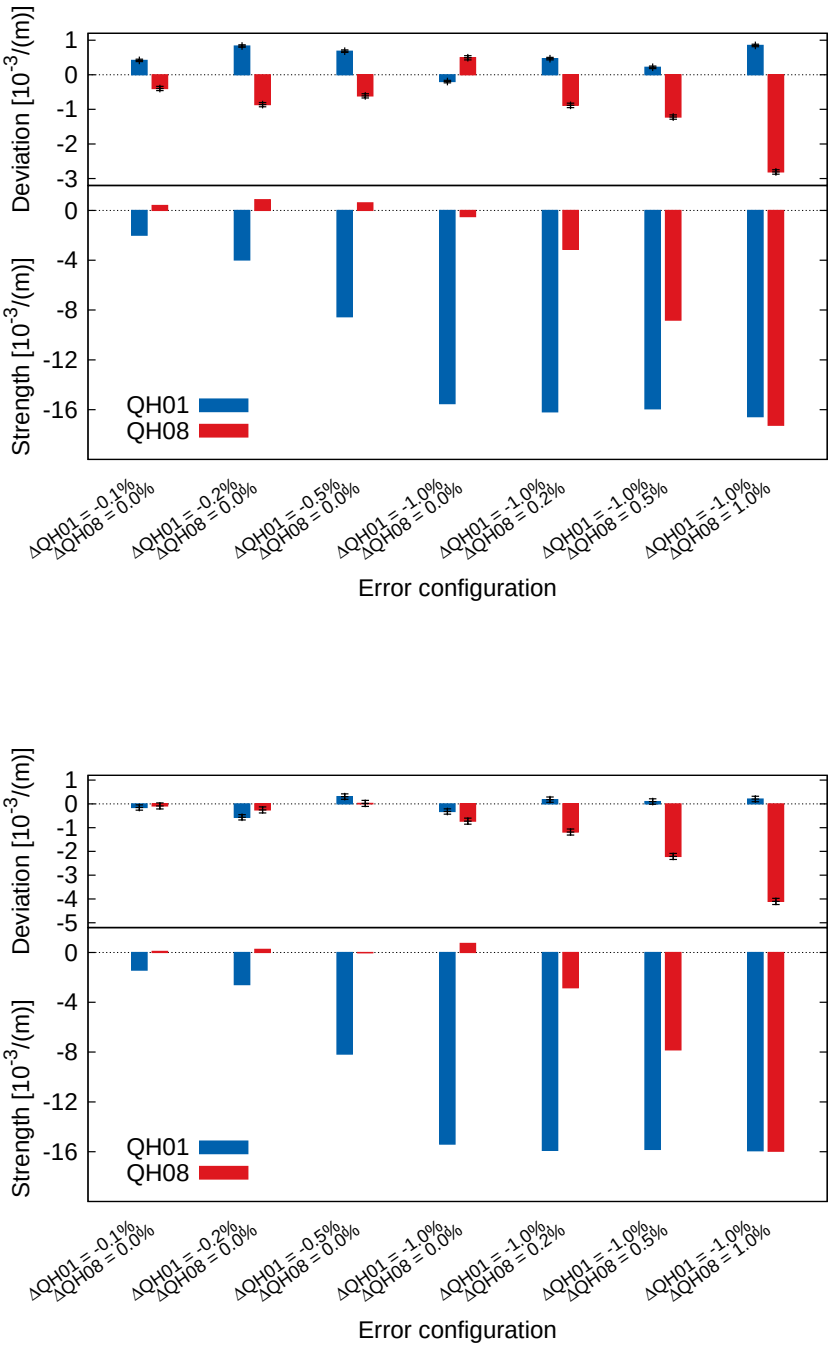

FIGURE 7.2. Results of the fit of QH01 and QH08 using the betatron amplitude measurements only. Two separated fits have been carried for $\Delta_{\bar{\beta}_x}$ (top) and for $\Delta_{\bar{\beta}_y}$ (bottom).

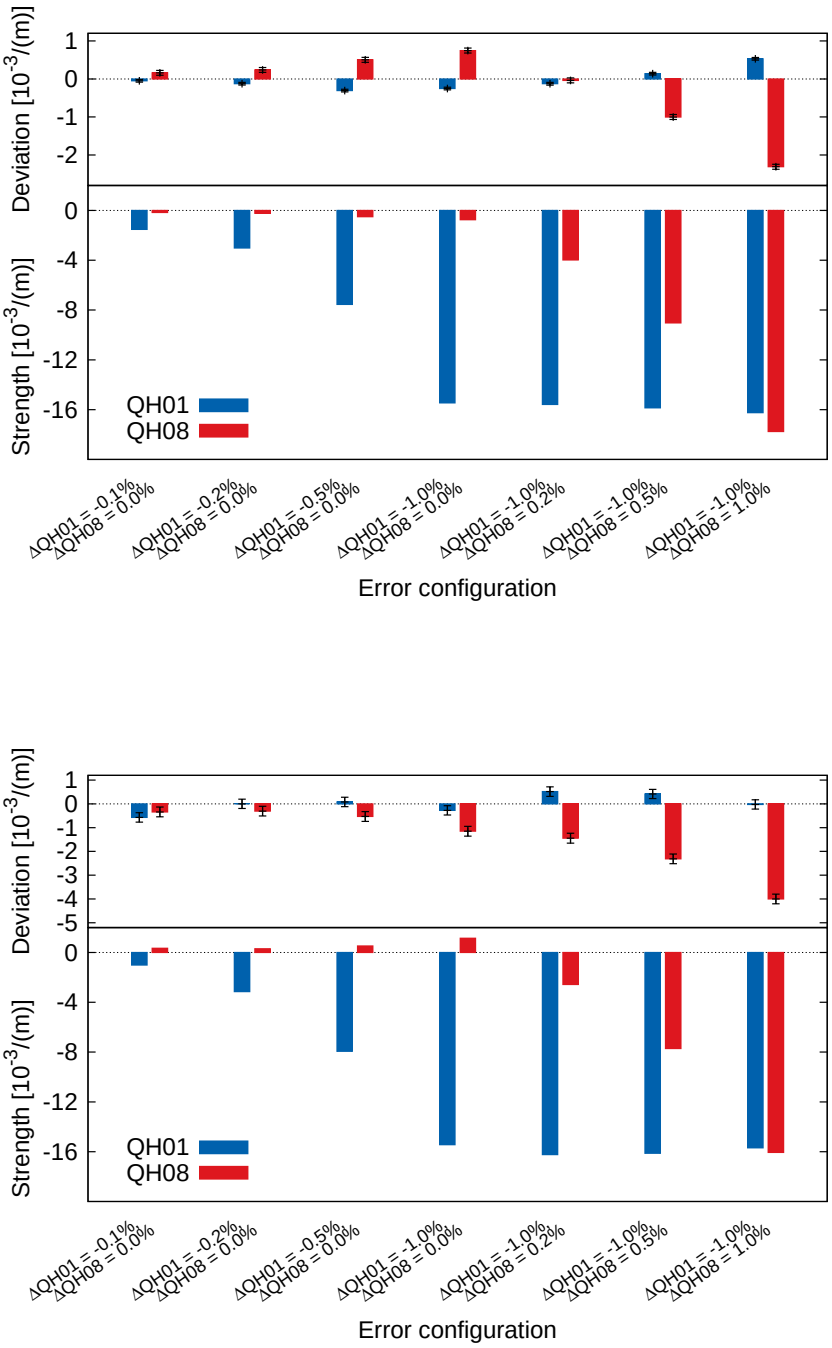

FIGURE 7.3. Results of the fit of QH01 and QH08 using the betatron phase measurements only. Two separated fits have been carried for Δ_{ϕ_x} (top) and for Δ_{ϕ_y} (bottom).

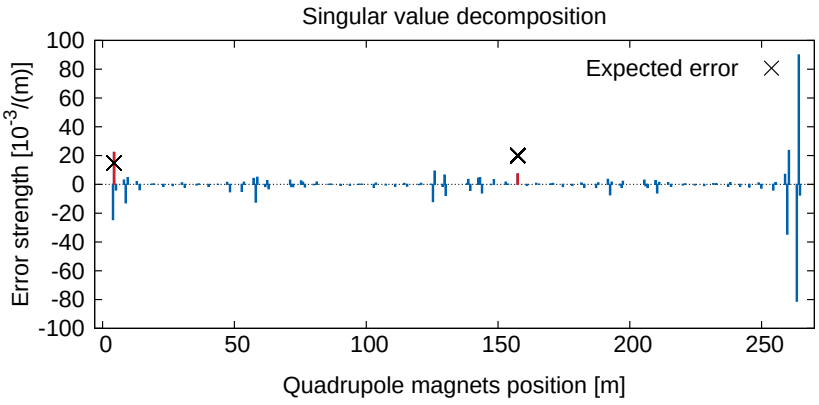

(A)

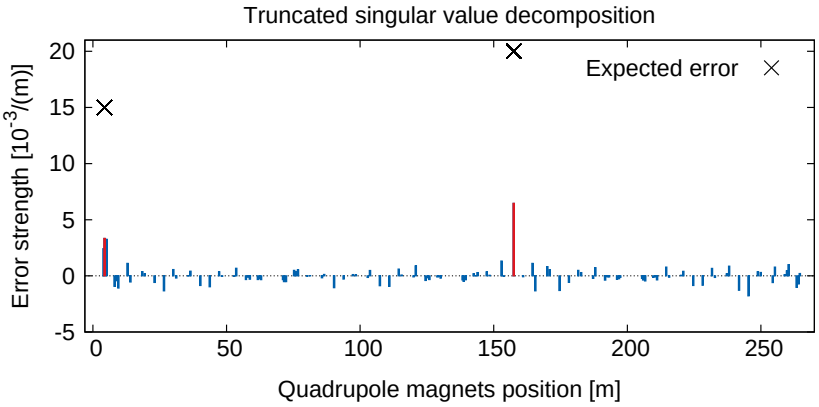

(B)

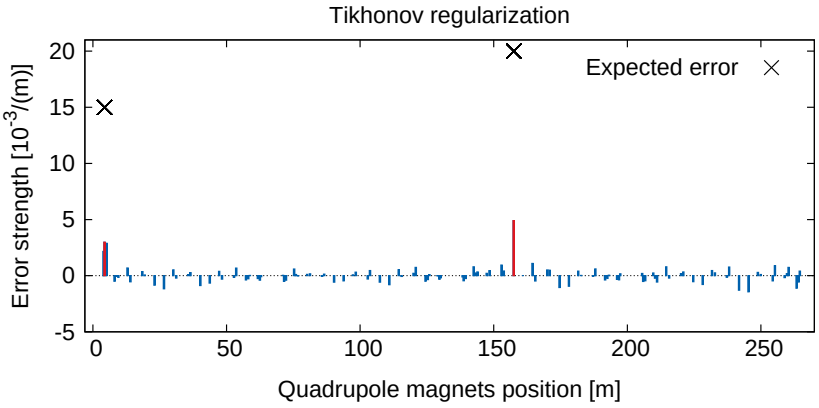

(C)

FIGURE 7.4. Results of the fit including all the 112 quadrupoles of the ALBA storage ring. The full set of observables, including betatron phase and amplitude for both planes, has been used. The fit has been repeated three times: first using the singular value decomposition technique (A), than using the truncated singular value decomposition (B) and finally with the Tikhonov regularization (C). While the plain singular value decomposition appears to be dominated by noise, the other two techniques produce a much cleaner result.

An improvement to the analysis can be obtained by constraining the norm of the vector $\vec{E}^{\sharp}$ to a small value in order to limit the identification of fake errors.

This condition can be achieved by introducing a truncation [**33**] in the computation of the inverse matrix M^{-1}:

$$M^{-1} = V\Sigma^{-1}U^{*} \qquad \Sigma_{ii}^{-1} = \begin{cases} 1/\Sigma_{ii} & \text{if } \Sigma_{ii} > k \\ 0 & \text{if } \Sigma_{ii} \leq k, \end{cases} \tag{7.7}$$

where all the components of the solution associated to singular values smaller than the threshold k have been removed. In the decomposition of Eq. 7.4 only the higher singular values provide an important contribution to the matrix M, identifying a strong correlation between a certain error configuration and the generated set of observables. The opposite is true for the inverse matrix M^{-1}, where the strongest contribution comes from the small singular values that in turn identify a loose correlation between a given set of observable and the actual error configuration that produced it. Because of the lower importance of the terms associated to the smaller singular values, the truncated version of M^{-1} provides a good approximation of M^{-1} for an adequately small value of the threshold parameter k and at the same time damping the noise introduced by loosely correlated error configurations, as in the case of close-by quadrupoles.

The results of the new analysis are shown in Fig. 7.4b, while the spectrum of the singular values is plotted in Fig. 7.5. Lacking of a better approach the threshold has been fixed to $k = 1.9 \cdot 10^{-2}$ following a trial and error technique: the parameter k has been swiped in order to optimize the result, based on the knowledge of the performed lattice manipulation. This technique is prone to introduce a bias, since the analysis is adjusted in order to obtain the expected result, on the other hand the large number of singular values unaffected by the cut (as shown in Fig. 7.4b) ensures a reliable result. To prove the effectiveness of the selected threshold the experiment should be repeated for many different error configurations, test that has not been carried out because of the extensive time requirements.

A drastic reduction of the noise is clear and the two sources of gradient error located at QH01 and QH08 are clearly identified above the noise.

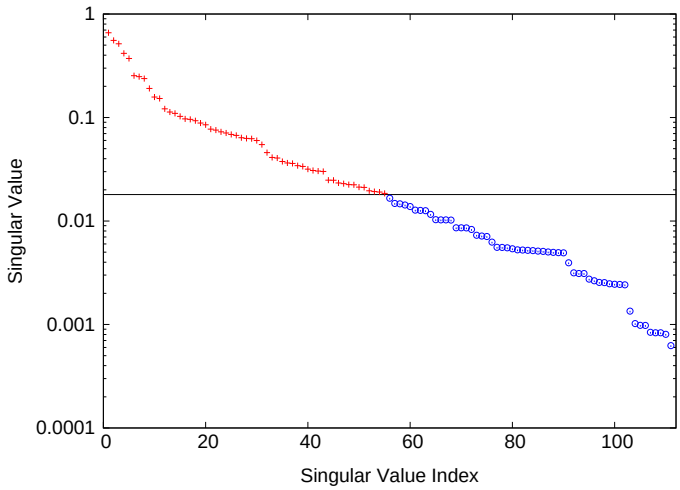

FIGURE 7.5. Singular values spectrum. The black line shows the threshold $k = 1.9 \cdot 10^{-2}$: red crosses are included in the calculation of the truncated inverse response matrix M^{-1} while blue dots are discarded.

An alternative approach to the truncated singular value decomposition is provided by the "Tikhonov regularization" [**44, 33**]: the inversion of Eq. 7.4 is reformulated as a least squares minimization problem, where the squared residuals to be minimized are:

$$||M\vec{E} - \vec{\Delta}||^2. \tag{7.8}$$

Now an explicit constrain on the norm of the vector $\vec{E}^\sharp$ is introduced turning the residuals to be minimized into:

$$||M\vec{E} - \vec{\Delta}||^2 + ||\Gamma\vec{E}||^2, \tag{7.9}$$

where the Tikhonov parameter Γ is set to $5 \cdot 10^{-4}$, following a trial and error approach as previously done for the parameter k. As shown in Fig. 7.4c the Tikhonov regularization is also an effective approach to cut down the noise producing a result very similar to the truncated singular value decomposition.

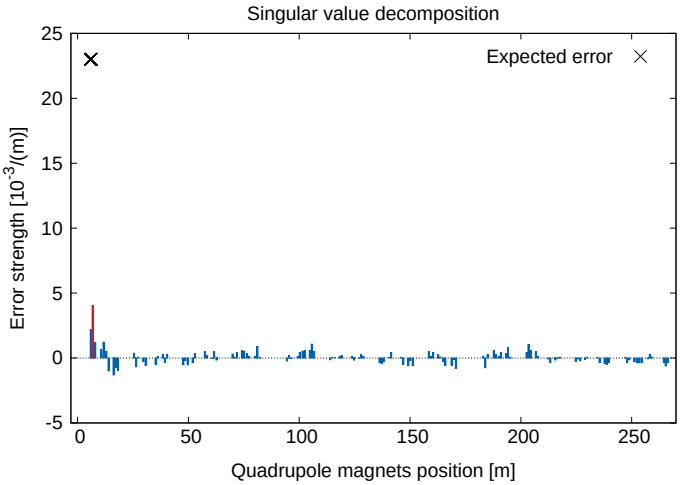

FIGURE 7.6. Plot of the fit including the 163 quadrupoles of the SOLEIL storage ring using the Tikhonov regularization method with $\Gamma = 1.5 \cdot 10^{-3}$. The full set of observables, betatron phase and amplitude for both planes, has been used.

From the previous results, the underestimation of the error strength appears a common side effect to both methods (the truncated singular value decomposition and the Tikhonov regularization). This is not surpising since the norm of the error vector $\vec{E}$ has been constrained to small values.

A similar experiment was also attempted in the SOLEIL storage ring. Here the quadrupole Q1 of the first cell (see Fig. 2.5) was selected as the source of gradient error and changed by 2%. The same analysis, employed at ALBA was applied also in this case with the only exception that the slower turn-by-turn measurements setup allowed only to take 30 acquisitions for each configuration.

Also in this case the error reconstruction based on the simple singular value decomposition was dominated by a strong noise, therefore the Tikhonov regularization has been employed. Figure 7.6 shows the result of the fit, similar to what observed in the case of ALBA: the position of the error source has been correctly discriminated but its strength is by far underestimated as a consequence of the constraint on the norm of the error vector $\vec{E}$.

7.2. Coupling and Non-Linear Corrections

The same procedure used in the previous section to localize single sources of gradient error can be extended to the case of coupling sources and sextupoles magnets. However, since tune spectral lines carry mainly information related to the quadrupoles, different spectral lines have to be included in the analysis in order to obtain a complete picture of coupling and non-linear sources.

7.2.1. *Coupling*

For the case of coupling, as discussed in Section 1.2, the signature lines for the horizontal and vertical plane have frequency respectively equal to the vertical and horizontal tune respectively. With this understanding, amplitude and phase of the coupling lines are extracted from the turn-by-turn data as described in Appendix A. To get rid of the amplitude and phase dependency of the coupling lines on the excitation conditions produced by the pinger magnets, coupling lines are renormalized by the tune lines as explained in Section 1.2.2. As a result the two new quantities (F_{xy} and F_{yx}) are completely independent from any variable but the lattice parameters and therefore can be used as the base for the analysis.

Following the same strategy adopted in the previous section, a gradient change was applied in one of the 32 skew quadrupoles of the ALBA storage ring. The skew quadrupole magnet QS08 was powered with increasing values of current and the quantities F_{xy} and F_{yx} measured for 100 acquisitions for each current setpoint. A proper observation of the coupling spectral lines required to increase the maximum betatron amplitude to $\sim 1.2\,\mathrm{mm}$ and $\sim 1.8\,\mathrm{m}$, respectively for the horizontal and vertical plane (that correspond to an action J_x=0.88 µm and J_y=1.5 µm or to an average amplitude of $\sim 1.0\,\mathrm{mm}$ for both planes).

A variation vector analogous to $\vec{\Delta}$ has been calculated for each line and every different magnet strength:

$$\begin{aligned} \vec{\Delta}F_{xy} &= F^0_{xy} - F^n_{xy} \\ \vec{\Delta}F_{yx} &= F^0_{yx} - F^n_{yx}, \end{aligned} \tag{7.10}$$

where the superscript 0 identifies the reference measurement performed with QS08 switched off, while the superscript n refers to any other configuration where QS08 was on.

Figure 7.7 shows the phase and amplitudes of F_{xy} and F_{yx} measured with QS08 excited with a current of 8 A: simulated and measured data agree within the experimental uncertainty. As in the case of the quadrupolar change, we fit the strength of QS08 from the experimental data by means of the singular value decomposition technique.

The fit results for each different excitation strength of QS08 are presented in Fig. 7.8: the agreement between measurements and model is still present, but there is a constant discrepancy of around 10 %. The origin of such mismatch is not clear, but most likely it is to be attributed either to a miscalibration of the magnet response to the excitation current or to the presence of a linear optics error at the position of the skew magnet.

As a final test the fit is extended to all the 32 skew quadrupoles present in the storage ring. The result plotted in Fig. 7.9 shows that the simple singular value decomposition is able to properly identify the source of coupling.

7.2.2. *Non-linear optics*

As discussed in Section 1.2 sextupoles are mainly responsible for four different spectral lines: two lines for the horizontal plane (F_{ns2} and F_{ns3}) and two for the vertical one (F_{ns0} and F_{ns1}) with frequency defined by combinations of the horizontal and vertical tunes. To facilitate the observation of the non-linear spectral lines, the pinger strength was increased in order to produce a maximum betatron amplitude of $\sim$ 2.4 mm and $\sim$ 3.6 mm, respectively in the horizontal and vertical plane (that correspond to an action J_x=3.5 µm and J_y=5.9 µm or to an average amplitude of $\sim$ 2.0 mm for both planes). Similarly to the case of coupling, the spectral lines have been properly renormalized by the tune lines to remove any dependency on the dynamical variables and obtain a signal that depends only on the lattice parameters.

The results of the experimental observation of the amplitude and phase for each one of the four sextupolar spectral lines averaged over 100 acquisitions is presented

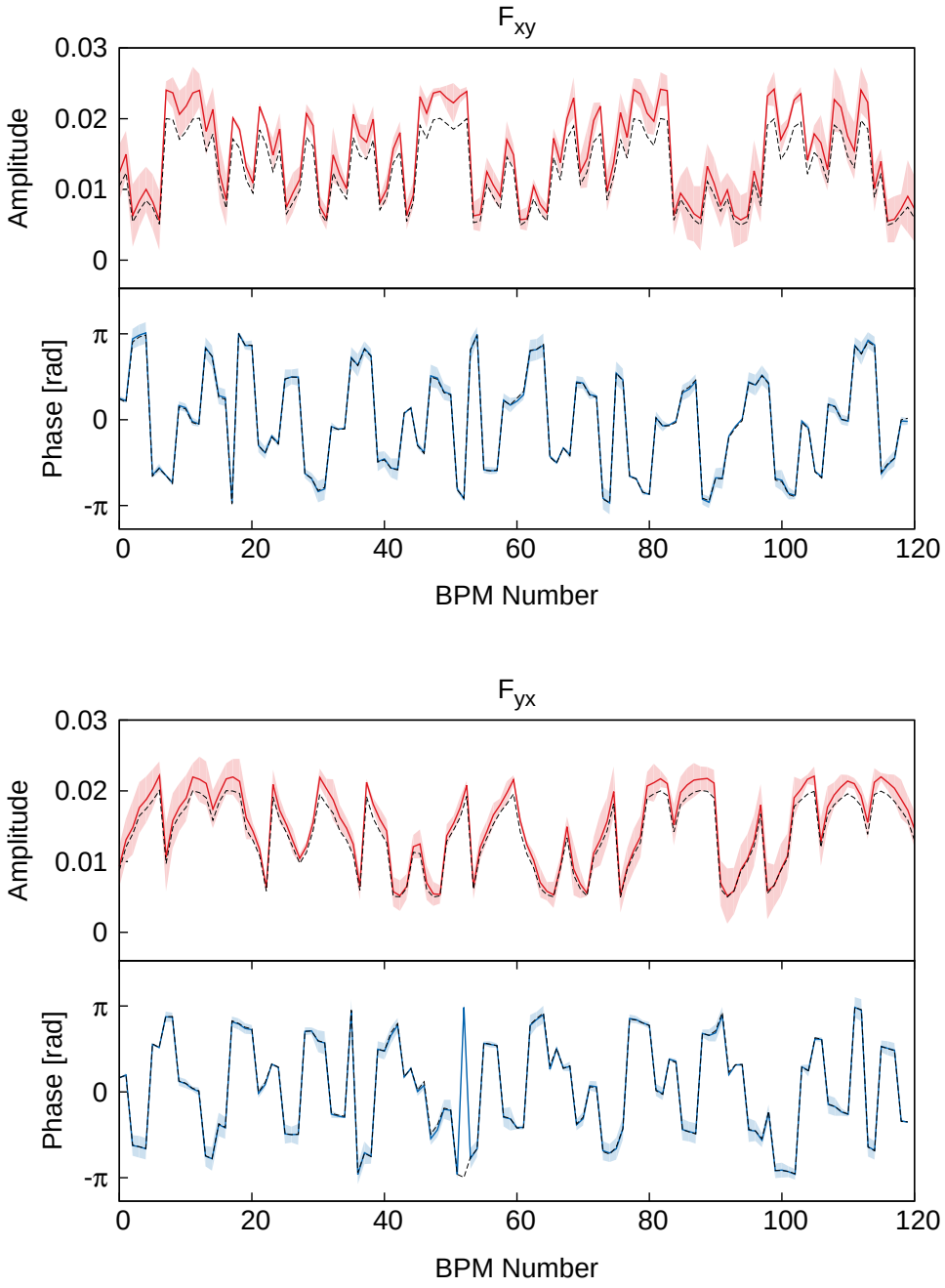

FIGURE 7.7. Upper and lower plots shows respectively the variation of amplitude and phase of the spectral lines F_{xy} and F_{yx} for a change in current of the skew quadrupole QS08 of 8 A. value. The solid lines represent the one-sigma uncertainty due to acquisition to acquisition fluctuations, while the dashed black lines, that follow closely the experimental results, show the theoretical value obtained from simulation.

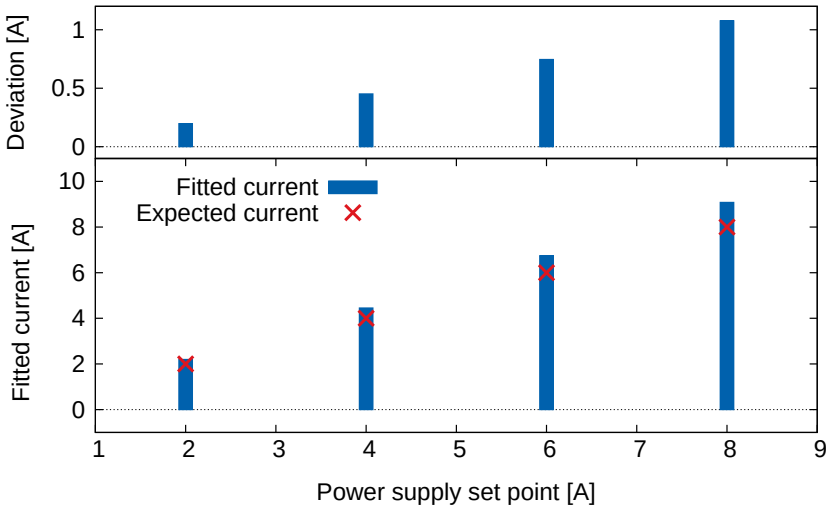

FIGURE 7.8. Results of the fit of QS08 using the spectral lines F_{xy} and F_{yx} for different values of the excitation current. A constant discrepancy of around 10% is always visible.

in Figs. 7.10 and 7.11: the measurements follow within the statistical error the theoretical values predicted by simulations.

To study the sensitivity of the measurements to single source of sextupolar error, an experiment similar to what already done in the case of quadrupoles and skew quadrupoles was carried out. Unfortunately the particular arrangement in families of the sextupoles in the ALBA storage ring required a special setup in order to detune one single magnet. In fact in each family, sextupoles are powered in series by a common current power supply, preventing from tuning individually a single magnet. To work around the problem, a resistive shunt was installed in one individual sextupole (SH02 in sector 7) to decrease its strength. Nevertheless, since the exact value of current flowing through the resistor was known only approximately, a precise comparison against the theoretical model, as done previously for quadrupoles and skew quadrupoles, was not possible.

Figure 7.12 shows the results of the fit based on the same singular value decomposition procedure used in the previous cases. The single error source stands

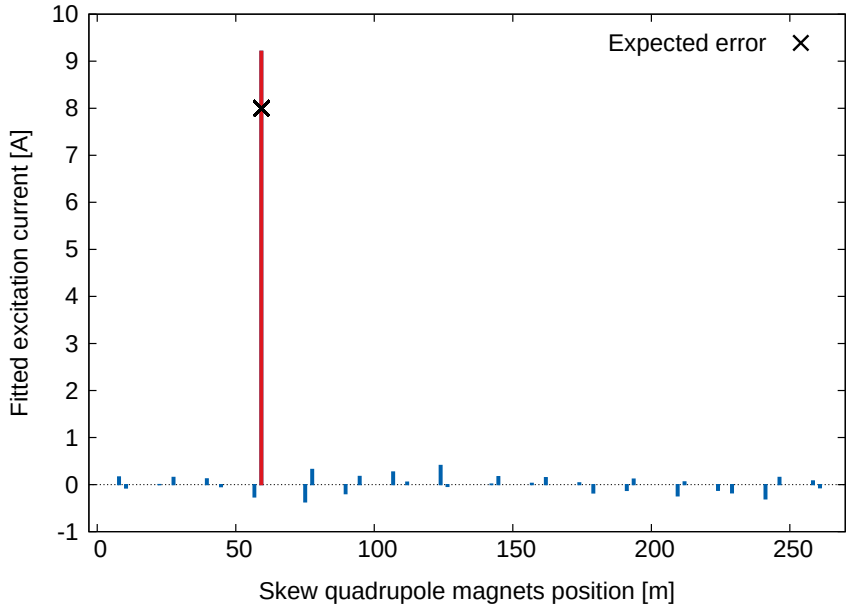

FIGURE 7.9. Results of the fit of the 32 skew quadrupoles of the ALBA storage ring using the spectral lines F_{xy} and F_{yx} measured while QS08 was powered at 8 A. In this case even a simple singular value decomposition is able to provide a clean reconstruction of the error source but a discrepancy of around 10% is present.

out clearly above the noise floor even without applying the Tikhonov regularization or a truncation in the singular value decomposition.

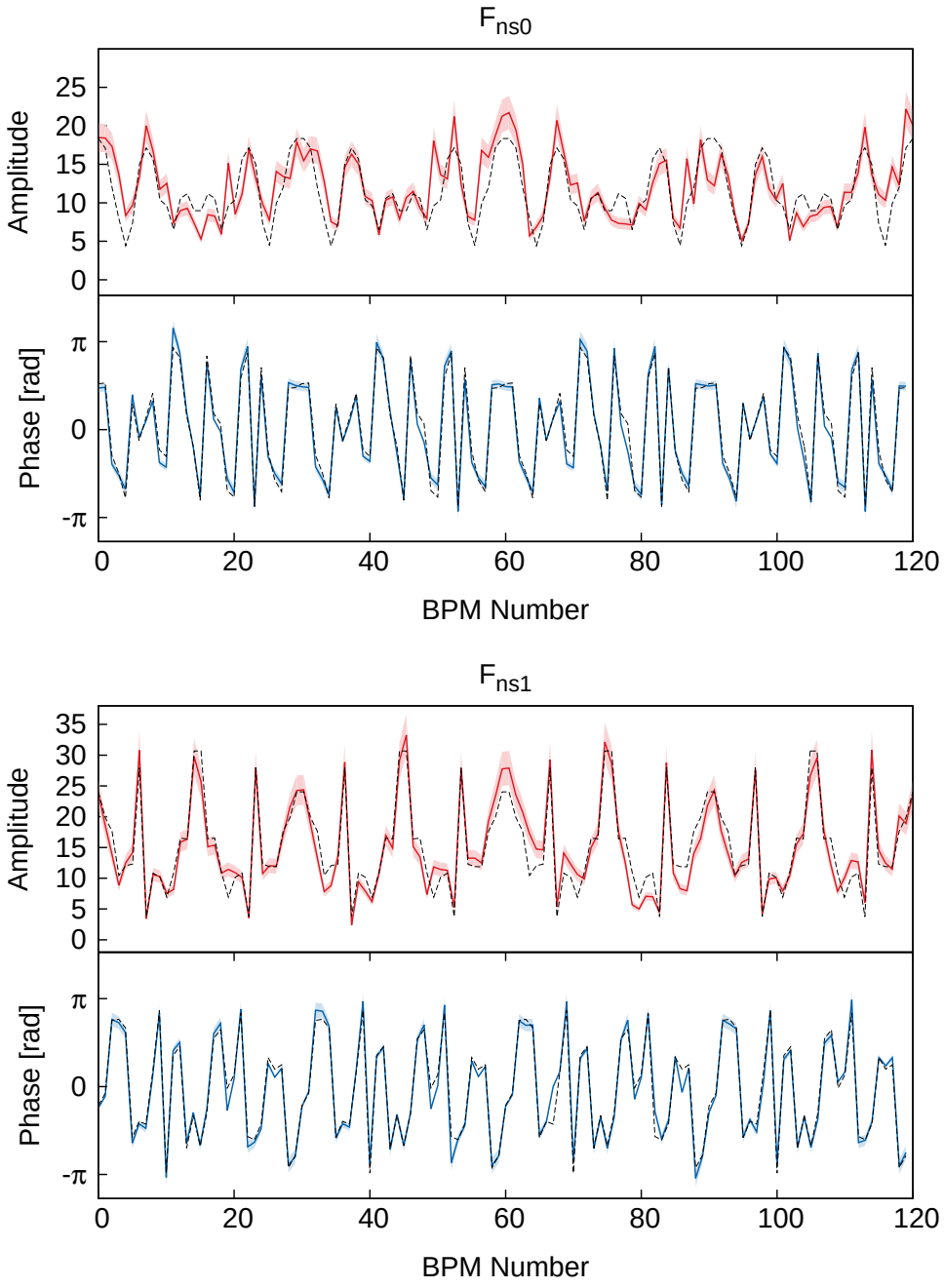

FIGURE 7.10. Amplitude and phase of the spectral lines F_{ns0} and F_{ns1} averaged over 100 acquisitions. The solid lines represent the one-sigma uncertainty due to acquisition to acquisition fluctuations, while the dashed black lines that follow closely the experimental results, shows the theoretical value obtained from simulation.

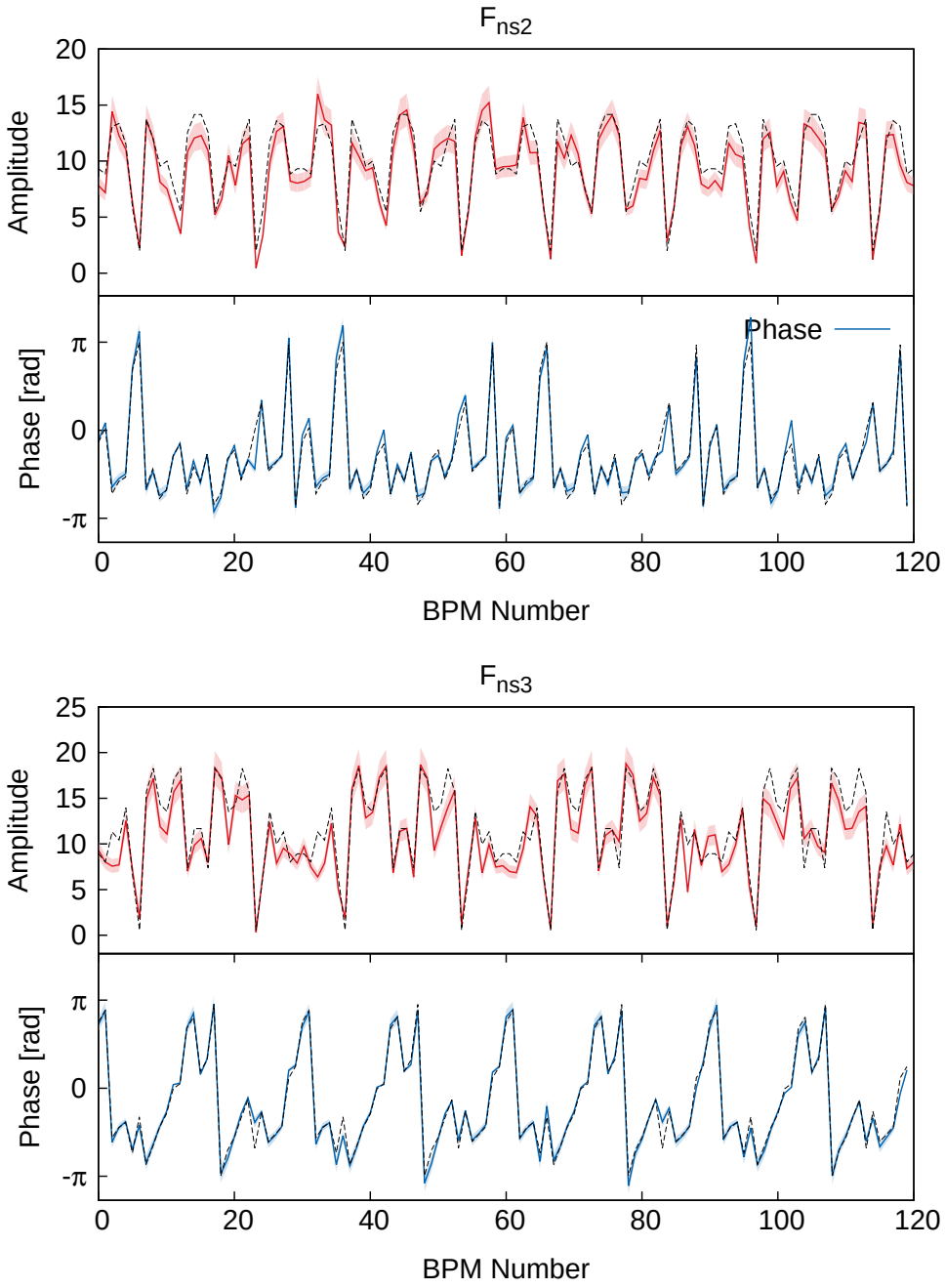

FIGURE 7.11. Amplitude and phase of the spectral lines F_{ns2} and F_{ns3} averaged over 100 acquisitions. The solid lines represent the one-sigma uncertainty due to acquisition to acquisition fluctuations, while the dashed black lines, that follow closely the experimental results, show the theoretical value obtained from simulation.

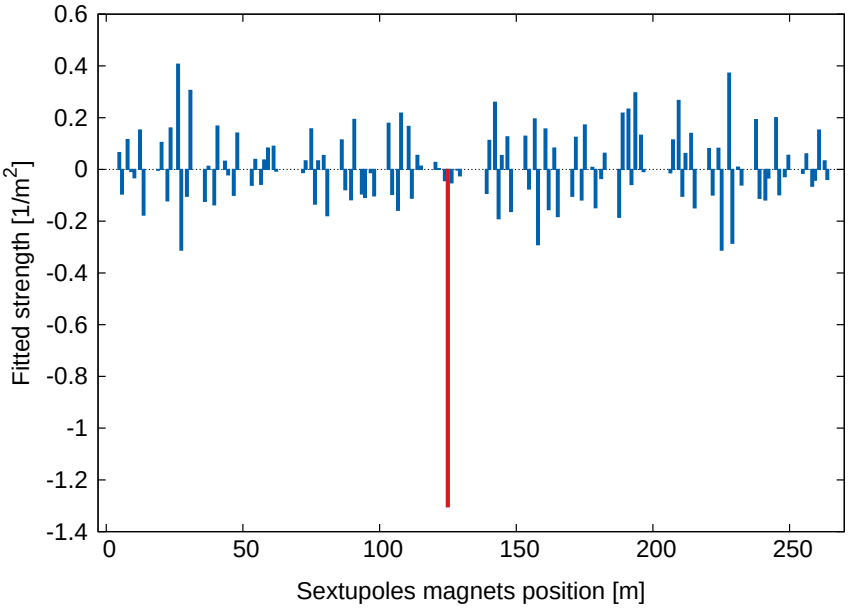

FIGURE 7.12. Results of the fit of the 120 sextupoles of the ALBA storage ring using the spectral lines F_{ns0}, F_{ns1}, F_{ns2} and F_{ns3} measured while SF2.4 was shunted. A simple singular value decomposition was able to provide a clean reconstruction of the error source.

CHAPTER 8

Measurement of errors due to transverse impedance

In this chapter we investigate how the turn-by-turn optics measurements previously described can be applied to study transverse coupling impedance sources in a storage ring.

The electromagnetic interaction between a charged beam and the vacuum chamber excites of an electromagnetic field: the wakefield. Such wakefields allow a long range interaction that couples not only the motion of particles within the same bunch but also the motion of different bunches. This coupling mechanism can lead to beam instabilities, especially at high value of bunch charge where the generated wakefileds are stronger, eventually limiting the maximum allowed stored current in the ring [**17**].

In the case of ALBA, a past theoretical study [**25**] shows how the contribution of the transverse impedance sources adds up, resulting in a maximum current threshold of $\simeq 20\,\mathrm{mA}$ (at zero chromaticity). To relieve the problem and allow for higher currents to be stored, ALBA rely on a combination of different approaches: An active transverse feedback [**36**] to damp the instabilities, increased value of chromaticity (Landau damping) and using a special filling pattern with long gaps between train of bunches that allows the wakefields to extinguish.

This solution allows to operate the storage ring on a regular basis with a stored current of 150 mA with a large stability margin that would allow to increase easily the current. On the other hand, in a young machine such as ALBA, the frequent requests for the design and installation of new hardware (e.g. insertion devices or diagnostic devices) brings continuously renewed attention to the problem.

The study of impedances of new vacuum chamber components constitutes a delicate task that steps through many different challenges, involving the correct

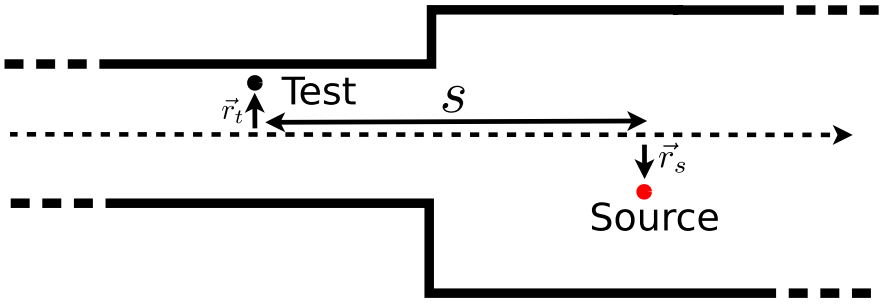

FIGURE 8.1. Two relativistic charges travels parallel through an accelerator component displaced by a longitudinal distance s. The first one, the source particle, excite an electromagnetic field in the surrounding structure, the field couple to the trailing test particle.

characterization of the electromagnetic properties of complex materials, as multilayer materials and coating and the electromagnetic computer simulation of the different structure geometries. Therefore the ability of measuring directly the contribution of impedance sources generated by the different vacuum chamber elements provides a valuable tool not only to validate the results of such complex design process, but also to directly characterize the behavior of such materials, as in the case of multilayer structures that otherwise would be difficult to model with a more traditional analytical or numerical approach.

Beam position monitor turn-by-turn analysis for impedance characterization has been usually employed in large circumference machines [**9, 16, 13, 12**], while synchrotron light sources have mainly used slow orbit based techniques. On the other hand the quality of the measurement demonstrated in the previous chapters suggests that the turn-by-turn technique can be applied succesfully to measure the typically small impedance values of a modern light source.

8.1. Transverse coupling impedance

A schematic representation of the wakefield-particles interaction is provided in Fig. 8.1. A particle (source charge) travels through the device under investigation exciting a wakefiled. A second trailing particle (the test charge) follows the source charge separated by a distance s on a parallel trajectory. A force acting on the test particle is observed due to the interaction with the wakefield.

The interaction has a longitudinal and a transverse component, since only the first one affects the transverse beam dynamics, making the phenomenon detectable by means of the turn-by-turn technique described in the previous chapters, the longitudinal component has not been considered in this work.

Indeed the problem that we aim to solve is more complicated, involving a whole bunch of particles, where each one acts at the same time as the source and the test particle. To study the generic case of a complex charge distribution we proceed by calculating the effect induced on the test particle by a point like source charge or the "impulse response" of the system. Hence, the cumulative effect is determined by doing a convolution between the bunch charge distribution and the impulse response that acts as a Green's function.

In the ultrarelativistic case, the integrated transverse kick exerted by a point-like source charge on a test particle moving parallel to the longitudinal direction $\hat{z}$ can be expressed trough the transverse wake function, defined as:

$$w_\perp(\vec{r}_s, \vec{r}_t, s) = \frac{c}{e}\int_{-\infty}^{\infty} [\vec{E} + c\hat{z} \times \vec{B}]_{z_t = z_s + s} dt \tag{8.1}$$

Where, $\hat{z}$ is the versor of the longitudinal axis, $\vec{r}_s$ and $\vec{r}_t$ are the transverse displacements of the source and test particles, while their longitudinal coordinates are z_s and z_t respectively. The fields $\vec{E}$ and $\vec{B}$ in general have a complicated dependency on the boundary conditions defined by the geometry of the surrounding and by the particles coordinates.

In a system with reflection symmetry around the axis of motion of the bunch, as in most of the vacuum chambers employed in accelerators, the wake function $w_\perp(\vec{r}_s, \vec{r}_t, s)$ is null on the axis of symmetry and increases moving away from it. The result is a gradient in the force that happens to be always defocusing in both transverse planes.

The above wake-field represents the Green's function (impulse response of the of the system) we are looking for and therefore can be used to calculated the cumulative wake-field produced by an arbitrary longitudinal bunch distribution $\rho(s)$ as follows:

$$W_\perp(\vec{r}_s, \vec{r}_t, s) = \int_{-\infty}^{\infty} \rho(s - s') w_\perp(\vec{r}_s, \vec{r}_t, s') ds'. \tag{8.2}$$

Finally we obtain the average transverse kick received by the bunch interacting with the wakefield as:

$$\Theta = \frac{Ne^2}{E_0} \vec{r}_s \int_{-\infty}^{\infty} \rho(s) W_\perp(\vec{r}_s, \vec{r}_t, s) ds. \tag{8.3}$$

The assessment of $w_\perp$ for a given geometry represents a very complicated problem by its own and will not be addressed in this context. However, since it is usually preferable to solve such problem in the frequency domain, it is common to express the wake field $w_\perp$ trough its Fourier transform $Z_\perp$ that happen to have the dimension of Ω/m and is commonly referred as the "impedance":

$$Z_\perp(\omega) = -\frac{i}{c} \int_{-\infty}^{\infty} \frac{\partial w_\perp(\vec{r}_s, \vec{r}_t, s)}{\partial r_s} e^{-i\omega s/c} ds. \tag{8.4}$$

Following the same path as before we proceed defining a quantity, this time in the frequency domain, that takes into account the contribution of the whole bunch distribution: the effective impedance $Z_\perp^{\text{eff}}$.

$$Z_\perp^{\text{eff}} = \frac{\int_{-\infty}^{\infty} Z_\perp(\omega) S(\omega) d\omega}{\int_{-\infty}^{\infty} S(\omega) d\omega}, \tag{8.5}$$

where $S(\omega)$ represents the spectrum of the bunch charge density. Using the definition of $Z_\perp^{\text{eff}}$ the kick produced by an impedance source now is written as:

$$\Delta K = \frac{d\Theta}{dr_s} = -\frac{N_p q^2}{E_0} Im(Z_\perp^{\text{eff}}) \int_{-\infty}^{\infty} \rho(s)^2 ds, \tag{8.6}$$

which, specialized for the case of a Gaussian distribution of particles that resembles closely the longitudinal particle distribution in a bunch of electrons stored in a synchrotron, provides:

$$\Delta K_{x,y} = -\frac{N_p q^2}{E_0} Im(Z_{x,y}^{\text{eff}}) \frac{1}{2\sqrt{\pi}\sigma_\tau}, \tag{8.7}$$

where σ_τ is the standard deviation of the Gaussian distribution (i.e. the bunch length). $\Delta K_{x,y}$ represents a defocusing kick similar to the one produced by a

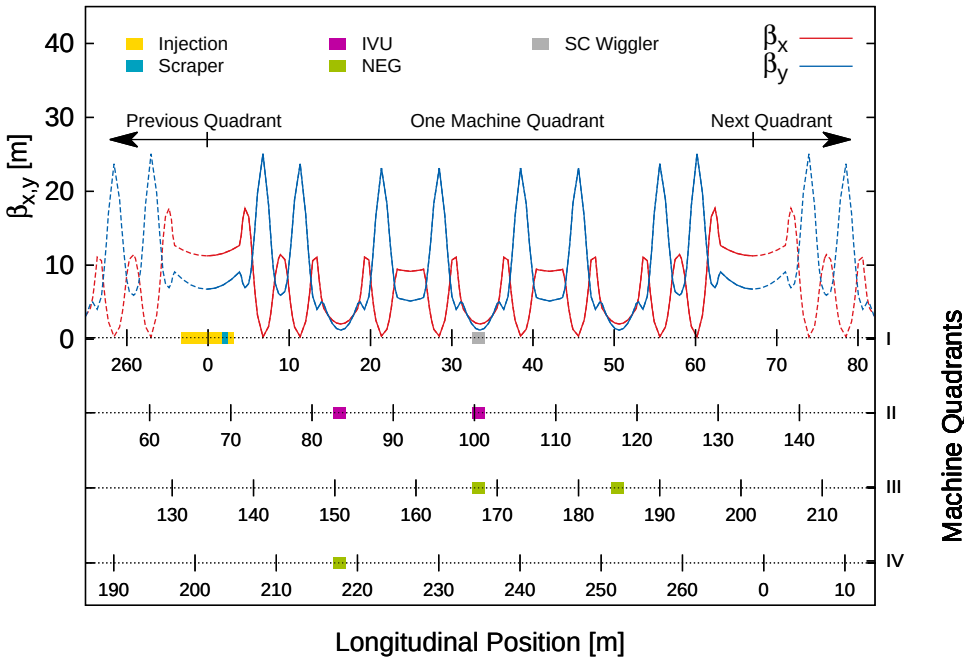

FIGURE 8.2. Betatron functions and location of the major transverse impedance sources in the ALBA storage ring. Insertion devices and the four kickers of the injection section accounts for the most of the overall impedance. Also the standard vacuum chamber, not represented in the picture, that extends all around the machine provides a strong contribution.

quadrupole (but defocusing on both planes). Note that for asymmetric structures the defocusing kick has different strength on the vertical and horizontal planes.

8.2. Impedance sources in the ALBA storage ring

All the elements contribute to the transverse impedance budget in a modern synchrotron light source, among them the insertion devices stand out, that requiring the beam to pass through a very narrow vertical aperture results in a strong wake-fields. Another important source of impedance is represented by the multilayer structures used in vacuum chamber the case of pulsed magnets, usually made of ceramic coated with a layer of metal, or by getter coated vacuum chambers, vastly used in modern synchrotron light source to supplement the vacuum system wherever other traditional means of pumping could not be employed, as in the case of ID vacuum chamber where the lack of space does not allow to install pumping ports. On the other hand, it is important to note that not only the impedance strength and therefore the resulting defocusing gradient but, also the betatron function plays

an equally important role in defining the overall optical functions distortion that we aim to measure (Eq. 1.64). This is particularly true in the case of insertion devices that usually are located where the beam has the minimum transverse cross section, while the opposite is true for the injection pulsed magnets.

A schematic view of the ALBA storage ring including the main sources of impedance along with the betatron functions is depicted in Fig. 8.2. As in many electron synchrotrons the strongest effect is observed in the vertical plane while no major contribution is present on the horizontal one. This asymmetry is due to the elliptical vacuum chamber, wider on the horizontal plane to allow the extraction of the synchrotron radiation, that is commonly employed in this kind of machine. Also the IDs, because of the "flat" geometry do not produce a significant effect on the horizontal plane. In the case of ALBA such asymmetry is extremely pronounced therefore the horizontal plane has not been considered in this study.

The main impedance contributors in the ALBA storage ring (Fig. 8.3) include 6 insertion devices (IDs) of which 3 use flat NEG coated aluminum chambers, 2 are in-vacuum undulators (IVUs) and one is a superconducting wiggler (SCW). The injection section, that includes 4 kickers with ceramic vacuum chambers coated with a 0.4 m layer of titanium [**35**], is also an important source of impedance and along with the standard beam pipe of the entire ring. IDs, kicker magnets and standard beam pipe account for most of the total transverse impedance budget.

A further strong source of impedance is provided by the vertical beam scraper (Fig. 8.4) located in the injection section. During normal operation this element does not contribute significantly, being placed far away from the beam (during normal operation the two jaws of the scraper are placed at ± 4.75 mm from the beam which means 9 mm full gap), on the other hand the ability to change its aperture and so to modulate its impedance contribution is of particular interest for this study, allowing to observe the optical functions distortion produced by a single impedance source.

A comprehensive list of the main impedance sources of the ALBA storage ring is presented in table 8.1 along with the produced defocusing kick per stored current obtained from computer simulations using the code GdfidL[**5**]. The listed values

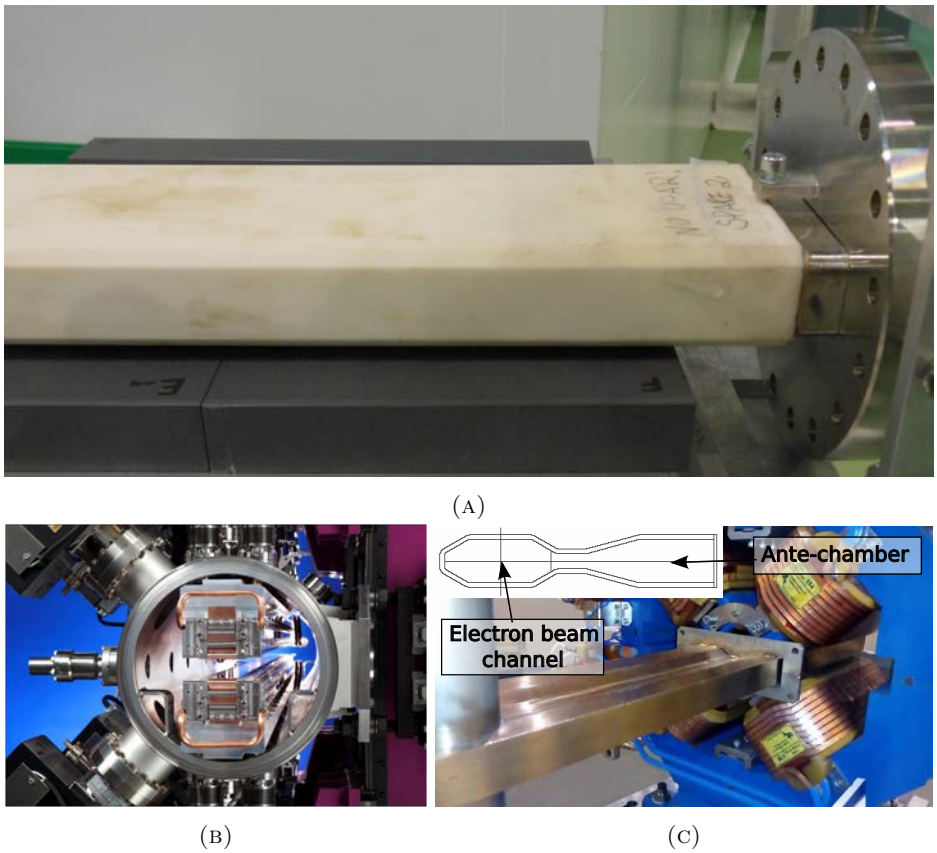

(A)

(B) (C)

FIGURE 8.3. The three main contributors to the ALBA impedance budget. Similar devices are found in many synchrotron light sources. A) A titanium coated alumina vacuum chamber used in pulsed magnet of the beam injection system. B) The impedance of an in-vacuum insertion device depends on the jaws position. During normal operation gaps up to 6 mm are allowed resulting in a noticeable impedance. C) the standard flat vacuum chamber represents one of the strongest contributor to the overall storage ring impedance.

include the device and the nearby transition elements of the vacuum chamber like absorbers, tapers, etc.

8.3. Measurement setup

Before engaging in the proper transverse impedance measurement, it is important to understand the required level of precision in order to allow the observation of the tiny optical distortion due to a impedance source of the order of magnitude typical of the ALBA storage ring. For this purpose we can take advantage of the experience gained with the measurements and correction of errors presented in Chapter 7. In fact the quadrupole QH01, used in the previous study, happens to be

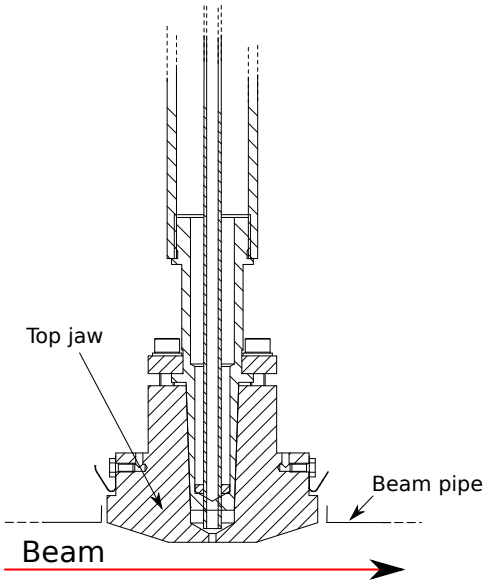

FIGURE 8.4. The top jaw of the vertical scraper. The scraper is made of two opposing copper jaws, that close one against the other in order to limit or stop (absorb) tha passage of the beam. During normal operations the jaws are closed symmetrically to ±4.75mm from the beam.

TABLE 8.1. ALBA storage ring vertical impedance budget and defocusing kicks per stored current. Standard beam pipe refers to the overall contribution of the standard vacuum chamber used in most part of the machine. The IVU value corresponds to the minimum gap configuration(6 mm), while being negligible at full open position. The contribution of the vertical scraper has been characterized for different gaps other than the nominal position at ±4.75 mm. In all cases the jaws aperture was kept symmetric with respect to the beam.

Element	Impedance [kΩ/m]	Kick [1/(A · m)]
Injection section	25.3	0.098
IVU	38.2	0.147
NEG-coated Al-chamber	31.2	0.120
Superconducting wiggler	14.6	0.056
Standard beam pipe	105.6	0.404
Scraper ± 4.75 mm	10.6	0.041
Scraper ± 3.0 mm	24.1	0.093
Scraper ± 2.5 mm	38.4	0.148
Scraper ± 2.0 mm	59.5	0.230

positioned next to the injection section, therefore resulting in an optical distortion

that mimics very well the one expected from a transverse impedance source located at this position.

The same analysis carried out in Chapter 7 based on the observation of the phase advance among consecutive BPMs $\psi_y^\dagger$ was repeated, but in this case by adjusting in the fit the strength of the quadrupole QH01 only (the betatron function $\bar{\beta}_y$ was excluded from the analysis because of the strong systematic error found in the betatron amplitude observations, as it will be shown in the next section). The results are plotted in Fig. 8.5, where an almost constant statistical r.m.s. fluctuation of $\sim 1.1 \times 10^{-4}\,\mathrm{m}^{-1}$ is evidenced for each setpoint of QH01, value that has to be compared against the defocusing gradient introduced by a typical impedance source.

In order to enhance the defocusing force of the impedance sources under investigation, the amount of charge stored in each bunch has to be maximized. Because in the ALBA storage ring values of bunch charge higher than 8 nC would drive the beam unstable, a value of 5 nC per bunch was chosen as a safe value to carry out the measurements.

Given such amount of charge, in the case of the injection section the expected integrated defocusing strength of around $5 \times 10^{-4}\,\mathrm{m}^{-1}$, that corresponds to five times the noise level.

On the other hand in order to explore the main impedance contributors found in Tab. 8.1, a smaller experimental uncertainty respect to what was observed for QH01, would be advisable. For this reason the number of acquisitions for each measurement was increased from 100 to 500, reducing the statistical error by a factor $\sqrt{5}$ with respect to what is observed in Fig. 8.5. Note that a higher number of acquisitions would lead to other problems, as for instance the effect of the stored current decay in the ring during the measurements, which are enhanced when operating the machine at high charge per bunch and the risk to come across slow thermal drifts. Running the acquisition system at 3 Hz, the whole measurement process lasts less than 3 minutes and causes a stored current drop of less than 5%, which is acceptable for our purposes.

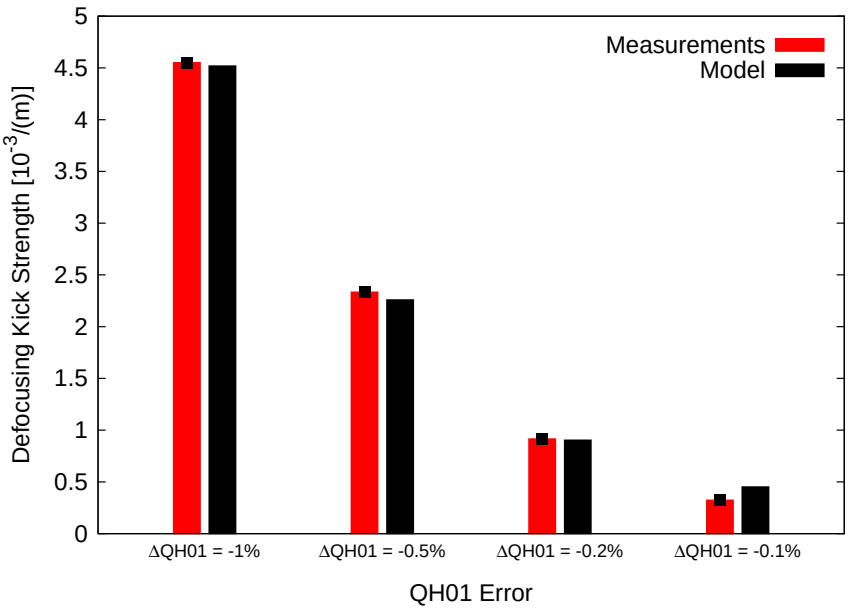

FIGURE 8.5. In red, measured change in the focusing kick for different QH01 setpoints. Each measurement is obtained averaging over datasets containing 100 acquisitions each. The error bars represent the standard deviation of the estimated focusing kick due to the acquisition to acquisition fluctuations. In black, the expected kick based on magnetic calibrations.

8.4. Test with a scraper device

A scraper with variable gap provides a good benchmark to verify the quality of the measurement method by varying a single and well localized impedance source. In particular this test allowed a direct comparison of the reproducibility of the $\bar{\beta}_y$ and $\psi_y^{\dagger}$ observations, highlighting the superiority of the latter.

As observed in the previous section, measurements have to be carried out using a large amount of charge per bunch in order to enhance the optical distortion induced by impedance sources. For this purpose a special filling pattern containing only two high charge bunches was used. An example of the actual filling pattern is shown in Fig. 8.6. The ability to directly observe the stored filling pattern has been a valuable tool, in fact because of the frequent injections required to keep up

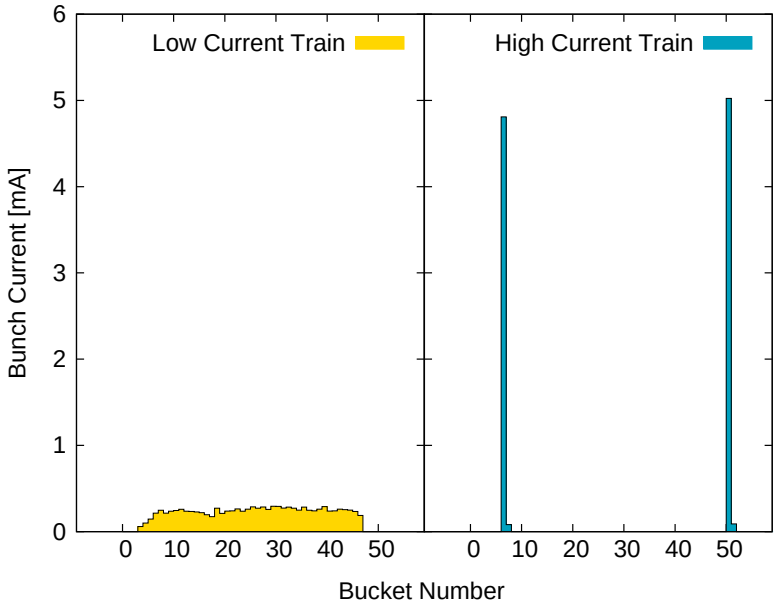

FIGURE 8.6. The two different filling patterns used during the impedance measurements of the scraper. A low charge per bunch filling pattern (left), similar the one used in all the previous measurements, composed by a train of 45 bunches, each one with a current of 0.22 mA on average. A high charge per bunch filling pattern (right) composed by only two bunches carrying around 4.9 mA each. The total current for the two filling pattern is approximately the same in order to produce a similar signal in the BPM and minimize any effect related to the different response of the BPM receivers to different signal strength.

with the strong beam losses, the risk of spoiling the filling pattern by injecting in a wrong bunch was high.

An optical measurement has been repeated for different apertures of the vertical scraper (6, 5 and 4 mm) plus a reference one at the nominal scraper position (9.5 mm). The measurements have been carried out following the same procedure described in Chapter 7 but with an increased number of acquisitions to 500.

The measurement with nominal scraper aperture (± 9.5 mm) was taken as a reference, hence a beta-beat function $\Delta\bar{\beta}_y$ and phase-beat function $\Delta\psi^{\dagger}$ calculated

as:

$$\begin{aligned} \Delta\bar{\beta}_y &= \bar{\beta}_y^0 - \bar{\beta}_y^1 \\ \Delta\psi_y^\dagger &= \psi_y^{\dagger 0} - \psi_y^{\dagger n}, \end{aligned} \tag{8.8}$$

where the index 0 stands for the reference measurement while n identify any other measurement carried out at different scraper positions (6, 5 and 4 mm). Then the same fit procedure was used as before to distinguish the vertical defocusing kick produced by the scraper impedance for each different gap.

Special attention was paid to keep the stored current decay fairly equal during the acquisitions of all the different data-sets, guaranteeing a good cancellation of the contribution due to any other impedance source except the scraper itself. In fact a difference in current between the two measurements would introduce also a beating due to any other impedance source aside from the scraper.

The measured defocusing kicks produced by the scraper obtained separately trough the fit of the observables $\bar{\beta}_y$ or $\psi_y^\dagger$ are presented in Fig. 8.7. The plot shows how the results obtained trough the fit of $\Delta\psi^\dagger$ follow much better the model value from Table 8.1 than the ones obtained from the fit of $\Delta\bar{\beta}_y$. In order to investigate the issue, the measured $\Delta\bar{\beta}_y$ and $\Delta\psi^\dagger$ have been plotted (Fig 8.8) together with the values obtained from a simulation of the storage ring lattice, where a defocusing error with strength equal to the one obtained from the fit, was placed at the injection section. The measured $\Delta\psi^\dagger$ appears to follow more tightly the simulated value than what observed in the case of $\Delta\bar{\beta}_y$. A quantitative evaluation of the mismatch is provided by the χ^2 test, that, as shown in the plot, in the case of $\Delta\bar{\beta}_y$ is found to be 15 times higher than for $\Delta\psi^\dagger$. The different behavior is probably to be attributed to the intrinsic different nature of the two observables: while phase measurements are essentially time measurements, therefore requiring only a very clean and stable source of clock for the BPM to provide reliable results, amplitude measurements depend strongly on the calibration accuracy and stability of each one of the four BPM channels that could have some minor drift during the long time required to carry out the measurement. In fact the

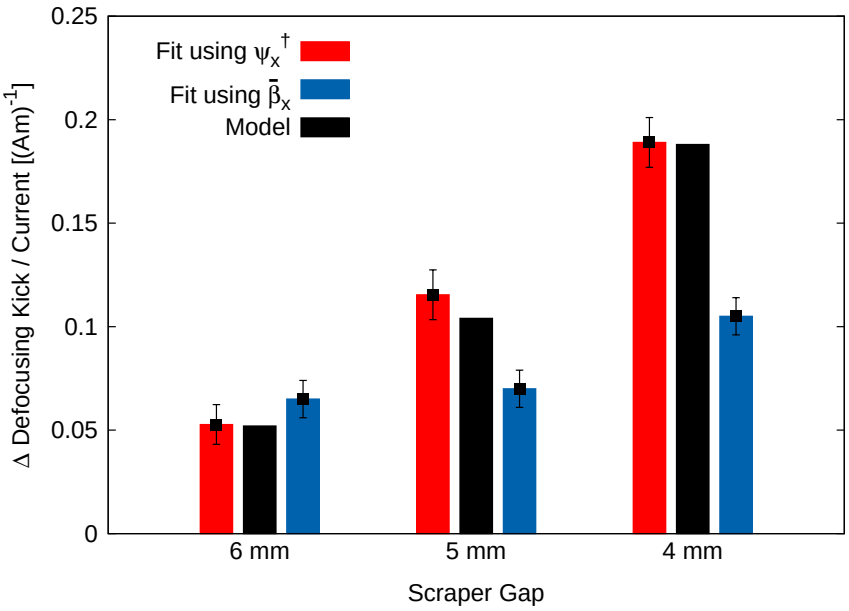

FIGURE 8.7. Measured and model change in the defocusing kick per current unit due to the transverse impedance of the vertical scraper for different gaps with respect to the scraper at reference aperture (9.5 mm). In red and blue, the values obtained from a fit of the quantities $\Delta\bar{\beta}_y$ or $\Delta\psi^{\dagger}$. Each measurement is obtained averaging over datasets containing 500 acquisitions each. The error bars represent the standard deviation of the estimated focusing kick due to the fluctuations among acquisitions. In black, the predicted values from the impedance computation calculated as kick differences of the considered gap to the reference scraper gap. While the fit of $\Delta\psi^{\dagger}$ (in red) follows the theoretical results (in black) the measurements based on the observation of $\Delta\bar{\beta}_y$ (in blue) show a discrepancy up to 47%.

Because of the poor results observed with the betatron amplitude measurements, the results presented in the rest of the work rely solely on the observation of the phase $\Delta\psi_y^{\dagger}$.

8.5. Local transverse impedance measurement

In this section we aim to fit the most important contributors to the overall ALBA impedance. For this purpose a phase-beat measurement is performed by repeating optics observations for two different bunch charges.

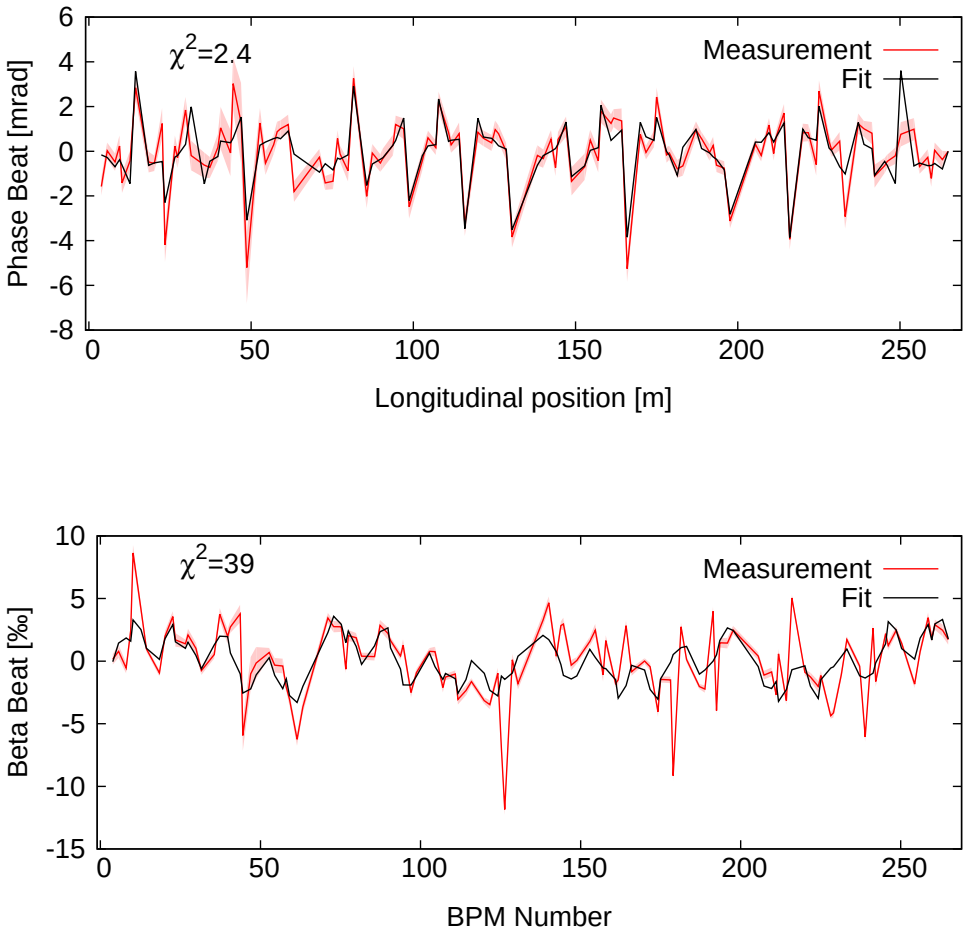

FIGURE 8.8. Measured $\Delta\psi_y^\dagger$ (top) and $\Delta\bar{\beta}_y$ (bottom) for each BPM along with the results obtained from a simulation of the storage ring lattice, where a defocusing error was placed at the injectction section with strength equal to the one obtained from the fit. The value of the χ^2 is also shown, highlighting the superiority of the phase-advance measurments.

The scraper position was set to the nominal value and the gap of each IVU was open to the maximum to reduce their impedance contribution to a negligible value. Data were acquired using two different filling patterns with high and low charge per bunch as shown in Fig. 8.6. The phase-beat function $\psi_y^\dagger$ is now defined from the previous measurements as:

$$\psi_y^\dagger = \psi_y^{\dagger\text{low}} - \psi_y^{\dagger\text{high}} \tag{8.9}$$

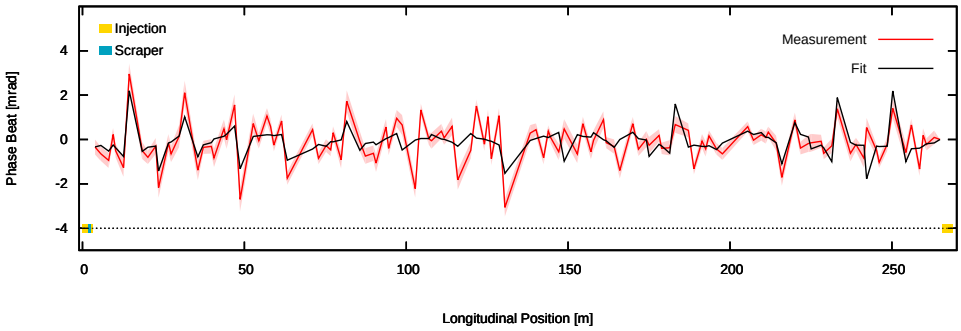

FIGURE 8.9. Measured phase beat for each BPM along with the one computed from the nominal machine model including the two measured defocusing kick produced by the beam pipe and the injection section.

hereafter the analysis follows the same path as in the previous cases. This time all the elements in Tab. 8.1 (except the IVUs and the scraper that were kept open) are expected to contribute with a kick.

Figure 8.10 shows the result of the analysis including the two strongest impedance sources: the injection section and the beam pipe. The fit is limited here to these two elements as the effect of the low-gap chambers of the IDs is actually small due to the rather low beta-function at their location (Fig 8.2). A crosscheck of such assumption is due.

The proof is provided by the measurement of the tune shift ΔQ^{meas} induced by the bunch charge, which can be expressed as:

$$\Delta Q^{\text{meas}} = \Delta Q^{\text{fit}} + \Delta Q^{\text{not-fit}} \tag{8.10}$$

where ΔQ^{fit} corresponds to the tune shift induced by the two fitted impedance sources (beam pipe and injection section) and $\Delta Q^{\text{not-fit}}$ is the tune shift produced by all the impedance sources not accounted by the fit.

A satisfactory agreement was found as the tune measurement revealed a tune shift $\Delta Q^{\text{meas}} = -2.3 \cdot 10^{-3}$ where a value $\Delta Q^{\text{fit}} = -1.8 \cdot 10^{-3}$ was inferred from the two fitted impedance sources, leading to a discrepancy of around 22%, confirming that most of the coupling contributors have been correctly taken into account by the impedance model.

The discrepancy between the left and right hand side of Eq.(8.10) gets smaller if we consider also the impedance sources that have not been included in the fit

that all together provide still a not completely negligible contribution. Adding up the tune shift induced by all the elements presented in Tab. 8.1 except the IVUs, which where opened to the maximum gap, the beam pipe and the injection section, already considered by the fit, we obtain an overall tune shift $\Delta Q^{\text{not-fit}} = -0.46 \cdot 10^{-3}$, reducing the discrepancy to 2%.

The observed phase-beat is plotted in Fig. 8.9 along with the one computed from the nominal storage ring model including the two fitted impedance sources. Even if the agreement between the experimental and the computed curve is not excellent the fitting procedure is still able, by averaging the information from each BPM, to extract the strength of the two impedance sources with a good level of agreement with respect to what expected from the electromagnetic simulation of Tab. 8.1.

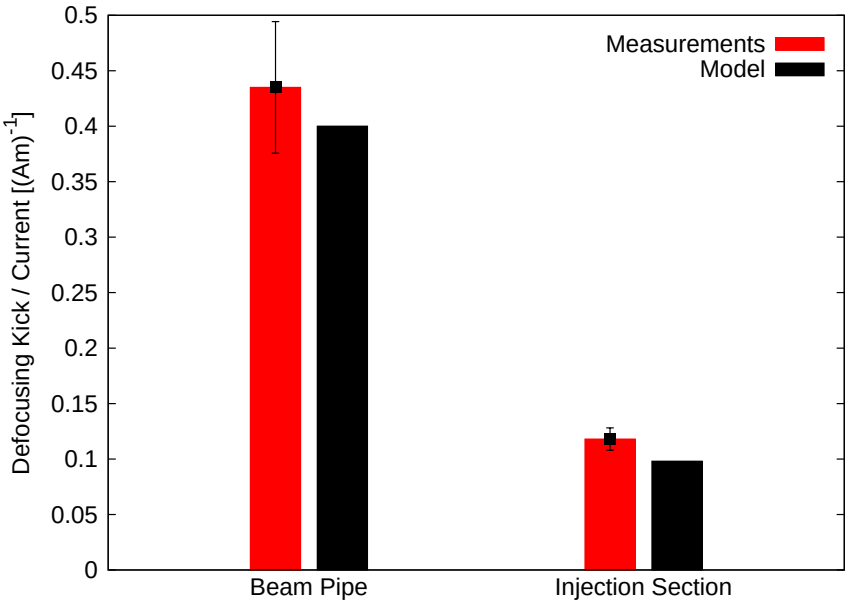

FIGURE 8.10. In red, the defocusing kick strength per current unit obtained from the fit including the beam pipe and the injection section. Each measurement is obtained averaging over datasets containing 500 acquisitions each. The error bars represent the standard deviation of the estimated focusing kick due to the fluctuations among acquisitions. In black, the predicted value from the impedance computation.

The agreement between the measurements and the values obtained by the impedance computation confirms that the machine impedance model is sound and well understood (see Ref. [**26**]). In particular, it is shown that the actual impedance model of the Ti-coated ceramic chambers, of which four are located in the injection section, is about correct.

8.6. Impedance of an in-vacuum undulator

The vertical impedance provided by the small-gap chambers and IVUs are a priori stronger than the other vacuum chamber contributions, however the small values of the vertical betatron function of the ALBA nominal lattice at their position (Fig 8.2) distinctly mitigate their effect (Eq. 1.64).

In order to amplify the effect on the optics and gain sensitivity for its impedance measurement, the nominal lattice has been detuned at the location of one of the IVUs increasing the vertical beta function by a factor 5.2 (see Fig. 8.11 and Ref.

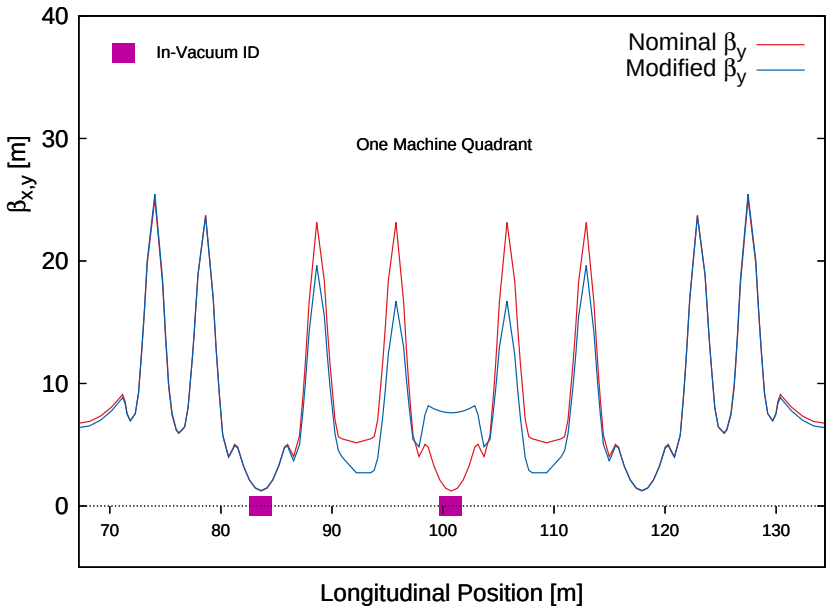

FIGURE 8.11. Vertical betatron functions for the nominal and modified ALBA lattices. The vertical betatron function is increased from 1.2 m to 6.5 m at the location of one IVU.

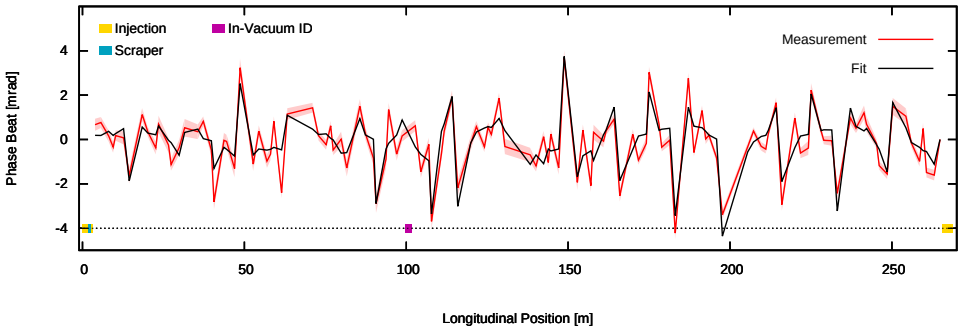

FIGURE 8.12. Measured phase beat for each BPM along with the one computed from the high β_v model including the three measured defocusing kicks produced by the beam pipe, the injection section and the IVU located at the high vertical beta position.

[**24**]), resulting in an increase of the phase beating due to the defocusing kick induced by the impedance.

Performing the same measurements of the phase beat described in the previous section (Fig. 8.12), but in this case using the lattice with high vertical beta at the IVU, allows to characterize its impedance. The gap of the insertion device was closed to 6 mm, and the same procedure used in the previous case was repeated. Figure 8.13 shows the results of the analysis including the defocusing kick produced by the insertion device impedance along with the one of the injection section and the beam pipe. The measurement results for the injection section and for the beam pipe are consistent with the previous analysis, while the effect of the insertion device is estimated with an even smaller statistical error, that makes the 20% discrepancy with respect to the theoretical predictions not negligible. On the other hand the phase beat fit (Fig. 8.12) shows a good agreement confirming the reliability of the measurement.

Since measurements and computations are supposed to be affected by very different error sources, the observed discrepancy allows to set a limit on the overall measurement uncertainty, including all the systematic errors that would be barely estimated otherwise. The most significant disagreement between measurement and simulation is found in the case of the IVU, exhibiting an overall kick discrepancy of $\Sigma_K = 0.029\,(\mathrm{Am})^{-1}$ equivalent to a transverse impedance of $7.6\,\mathrm{k\Omega/m}$ (20% of the model value of $38.2\,\mathrm{k\Omega/m}$). On the other hand, since the phase beat induced by an impedance source is proportional to the beta value, a better error estimation

is obtained by multiplying the kick error by the beta, $\beta\Sigma_K = 0.19\,\mathrm{A}^{-1}$ equivalent to a β-weighted transverse impedance of $49\,\mathrm{k}\Omega$.

8.7. Measurement Limits and Possible Improvements

In order to characterize smaller impedance contributors an improved sensitivity and a reduction of noise and systematic errors is desirable. In this section we propose a few options to improve the overall measurements quality, which for technical limitations of the present ALBA experimental setup could not be tested. Nevertheless we think that it would be beneficial for machines equipped with more advanced hardware [**37, 6**].

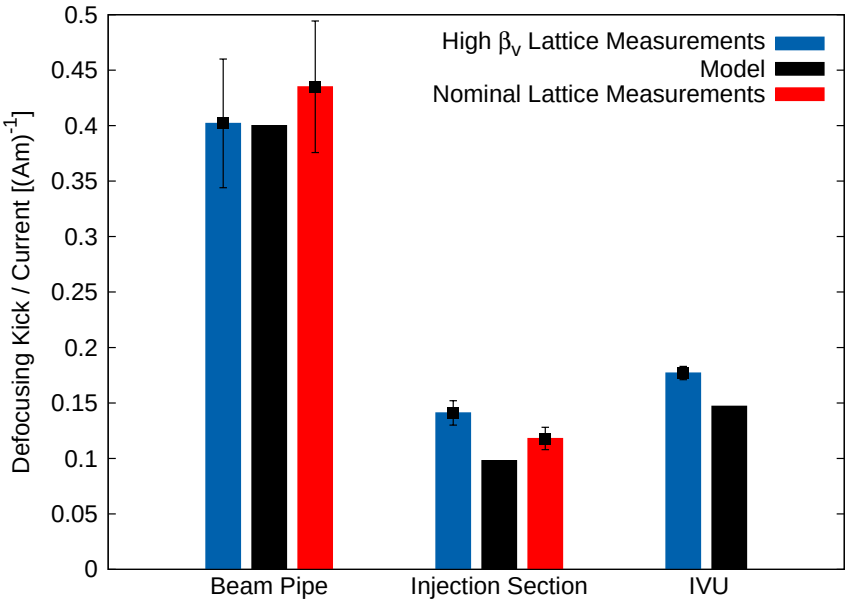

FIGURE 8.13. In blue the defocusing kick strength per current unit obtained from the fit including the beam pipe, the injection section and the IVU located at the high vertical beta spot. Each measurement is obtained averaging over datasets containing 500 acquisitions each. The error bars represent the standard deviation of the estimated focusing kick due to the acquisition to acquisition fluctuations. In black the predicted value from the impedance computation while red bars represent the defocusing kick obtained from the previous measurement (Fig. 8.10) where the nominal lattice was employed.

Two main factors were identified as the main source of measurement uncertainty: fast optics fluctuations, due to the electric noise in the quadrupoles power supplies; and slow machine drifts, likely due to the different thermal loads on the machine components produced by the different filling patterns.

Having identified the main sources of error, we can proceed to analyze possible solutions. Regarding machine drifts related with filling pattern, a possible cure could be found by storing together a high and a low current bunch trains in a hybrid filling pattern fashion. In this configuration there would be no need anymore to switch from one filling pattern to the other, avoiding thus different thermal loads in the machine. Moreover, avoiding the injection of a different filling pattern between acquisitions would result in the beneficial side effect of speeding up the measurement process, reducing also the effect produced by any other slow machine drift unrelated with the change in filling pattern. To discriminate the signal produced by only one of the two trains, BPMs with sub-turn resolution are needed. Unluckily the radio-frequency front-end employed in the BPM system of ALBA does not meet such requirements, preventing us from testing this option.

Since the employed BPM system does not provide any way to isolate the signal produced by each one of the two trains, a way to disentangle the two signals downstream is required. An option is provided by the small tune shift due to the optic distortion itself produced by the transverse impedance. In this case the two signals are acquired simultaneously and separated afterward by means of spectral analysis. In this approach BPM with sub-turn resolution are not required, instead very good linearity is mandatory. A first attempt to apply the proposed techniques at ALBA did not deliver the expected results.

Conclusions

The goal of this thesis is to test and validate the turn-by-turn beam position measurement technique applied to the study of the linear and non-linear beam dynamics in third generation of synchrotron light sources, in particular at ALBA, where the turn-by-turn acquisition and analysis chain was needed from scratch.

First, an approximated analytical representation of the linear and non-linear transverse beam dynamics, derived by means of a perturbative approach, was implemented in a first place as a Matlab routine and subsequently as part of the Elegant accelerator simulation software. This allowed for a fast computation of the non-linear transverse beam motion (an improvement of more than one order of magnitude on the execution speed was observed respect to tracking). The prediction obtained with the approximated formulas agrees with numerical simulations (tracking) within a 0.1%.

Regarding the acquisition system, the major limitation is located in the BPM electronics by the turn-smearing problem. In light sources like SOLEIL, no other solution than compensating the smearing through a deconvolution technique was possible. Instead, a different approach was followed at ALBA, where the firmware employed by the BPM electronics has been replaced with a new one (MAF) designed specifically for turn-by-turn applications, this procedure involved a great deal of work requiring to understand in depth the BPMs internals. This approach allowed indeed for better quality data, on the other hand the incompatibility between MAF and standard firmware (required for slow orbit acquisition) prevented from taking advantage of the turn-by-turn measurements during normal machine operation.

The turn-by-turn data acquired in the experiments were treated using a novel optimized spectral analysis procedure developed in this thesis. It is based on the approach proposed by Laskar, but extended to take into account also the damping.

The spectral components of the transverse beam motion, due to the different lattice elements, were isolated and studied using the first-order approximated formulas.

The experimental work was articulated through several tests. A first set of measurements was dedicated to the characterization of the linear lattice. The measurements show a level of agreement (β-beat $< 2\%$), with respect to the nominal values, comparable to what observed with LOCO (β-beat $< 1\%$). Further tests to establish the ultimate sensitivity to small optical functions variations were obtained by manipulating single lattice elements and measuring the resulting optics variations. The tests, carried out at ALBA and SOLEIL, showed how a $\sim$1% quadrupole strength variation (with respect to the nominal quadrupolar strength) can be localized with a similar degree of accuracy to what is observed with LOCO. This limitation stems from the large number of quadrupoles and their close placement that makes it difficult to disentangle correctly the contribution of each magnet.

Turn-by-turn technique has also been applied to the characterization of coupling and non-linear lattice elements (sextupoles) in the ALBA light source. The ability of turn-by-turn to correctly localize a single source of coupling was challenged by introducing in the storage ring lattice a controlled coupling source. A high degree of precision was observed in localizing the error source, and only a 10% disagreement between measurements and theoretical predictions on the coupling source strength was observed.

A similar test was also carried out for the sextupole families using a resistive shunt to change the excitation current of a single element. The ability to localize the sextupolar error position in the lattice was successfully demonstrated.

The experiments showed how the turn-by-turn acquisitions shine as for sensitivity,/ enabling the detection of very small variations of the optics function. This made it possible to apply the turn-by-turn technique, for the first time in a light source, to the measurement of localized transverse impedance sources. The experiment, carried out in the ALBA storage ring, led to the characterization of the individual defocusing effects produced by different transverse impedance sources, including elements like scraper, injection zone, in-vacuum undulator and standard vacuum beam pipe. The good agreement between the measurements and the transverse impedance model based on analytical calculation of the resistive wall and

GdfidL simulation of the geometrical impedance confirmed that the turn-by-turn technique is a valid diagnostic tool to carry out very sensitive and non-intrusive optics measurements. Furthermore it has been shown how the smaller impedance sources can still be properly characterized by manipulating the machine optics in order to obtain a magnification of the induced defocusing kick. This method has been used to characterize impedances as small as the one of the ALBA IVUs.

Acknowledgements

The author wishes to express his gratitude to Gabriele Benedetti who followed closely the work and guided patiently the preparation of the thesis, Zeus Martí for helping carrying out the experimental work and the many fruitful discussions, Andrea Franchi for proof reading the thesis and making constructive suggestions, Thomas Günzel for the fruitful discussions regarding collective effects, Ubaldo Iriso for the fruitful discussions and making valuable suggestions, Ricard Núñez and Nuria Ayala for their work on the ALBA pinger magnet, Angel Olmos and Jairo Moldes for helping setting up the ALBA BPM system, Laura Torino for her work on the single photon counting, Andriy Nosych for helping setting up the bunch length measurement setup, Raquel Muñoz for setting up the single bunch injection and the ALBA operation group for helping with the measurements.

The author is also grateful to Michael Borland for helping integrating the simulation code into Elegant, Laurent Nadolsky, Alexandre Loulergue and Nicolas Hubert for helping with the experimental work at SOLEIL and the fruitful discussions.

APPENDIX A

Spectral analysis of turn-by-turn data

This appendix deals with the problem of the precise determination of the main spectral components of the turn-by-turn beam motion, described in Section 1.2.2, from the experimental data measured with BPMs. Let x_n a vector representing the turn-by-turn horizontal or vertical beam position for N turns. The discrete Fourier transform

$$F_q = \sum_{n=0}^{N-1} x_n e^{2\pi\imath qn/N} \tag{A.1}$$

provides a very general approach to the problem of the spectral analysis. The frequency of the main spectral components can be easily identified, being the ones with strongest amplitude, and consequently amplitude and phase of each spectral line estimated. Once a list of the main spectral components has been filled out, it is easy to associate every spectral line with the ones exhibiting closest frequency to the lines predicted by the theoretical model (see Tab. 1.1).

On the other hand the spectral decomposition produced by the discrete Fourier transform has an intrinsic frequency resolution limited to $1/N$, far from being satisfactory for our purpose. A strong improvement is obtained by taking advantage of the knowledge of the structure of the turn-by-turn signal. In fact by providing a model of the expected signal that depends only on a small set of unknown parameters it is possible to proceed by optimizing such parameters in order to fit the measured turn-by-turn signal. Such approach produces a very precise amplitude and phase estimations. Looking at Tab. 1.1 in Section 1.2.2 we find out that the beam transverse motion can be decomposed in a rather large set of spectral lines, each one characterized by his own frequency, amplitude and phase leading to a rather complicated and time consuming fit procedure. On the other hand, taking advantage of the larger amplitude of the tune lines with respect to any other line, it is possible to proceed in a two steps approach, were in a first phase only the

tune lines are fitted neglecting the weaker ones. Because of the reduced amount of parameters the fit is now carried out in a much shorter time, while the amplitude disparity between lines still allows to produce a very accurate estimation of the parameters of the tune lines despite the approximation.

Before proceeding to the evaluation of the weaker spectral lines, the contribution of the dominating tune lines has to be removed from the turn-by-turn signal x_n. In fact, as shown in Fig A.1, higher amplitude lines can mask or offset the weaker

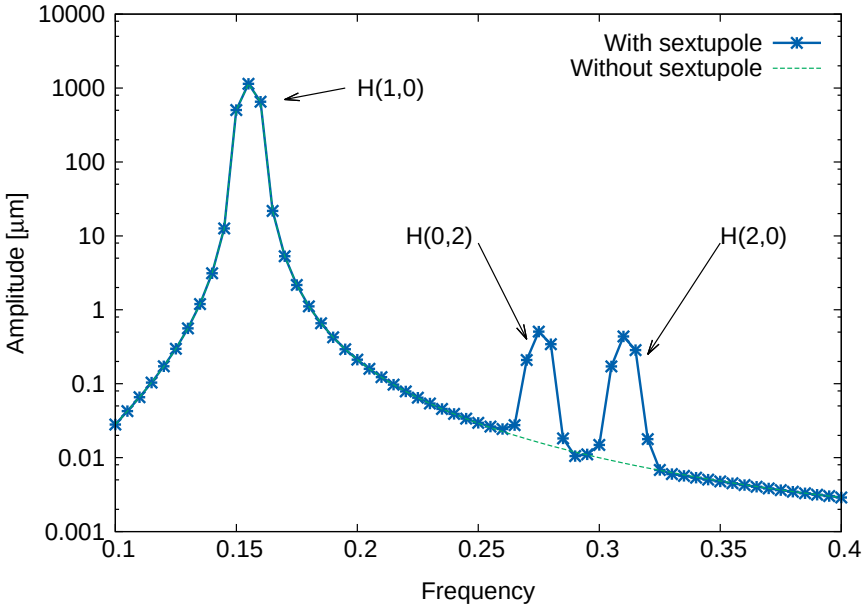

FIGURE A.1. Spectrum of the turn-by-turn horizontal transverse motion in presence of sextupoles. The data have been obtained from tracking, following the same procedure used in Fig 2.8, but this time the high amplitude tune line H(1,0) has not been removed. The result is an offset on the two faint sextupolar lines H(0,2) and H(2,0). A correct evaluation of amplitude and phase of the weaker lines requires to remove the contribution of the stronger ones.

ones. This is obtained by defining a new "purged" turn-by-turn signal defined as:

$$X_n^{\mathrm{P}} = x_n - A_0 \cdot \sin(2\pi n\nu_0 + \phi_0), \tag{A.2}$$

where A_0 and ϕ_0 are respectively the amplitude and phase of the tune line obtained from the fit.

Now by exploiting the fixed relations between the tunes and the frequency of skew quadrupolar and sextupolar lines shown in Tab. 1.1, it is possible to evaluate amplitude and phase of these lines, without the need to establish again, with a time consuming fit, their frequency.

The precise estimation of the frequency of every spectral line is obtained through the largely used method developed by Laskar [**30**]. In this method the discrete Fourier transform F_q is extended to continuous values of the frequency:

$$\mathcal{F}(\nu) = \sum_{n=0}^{n=N-1} x_n \cdot e^{-2\pi\imath\nu n/N}. \tag{A.3}$$

The line frequency ν_0 is then estimated by maximizing $|\mathcal{F}(\nu)|^2$. A Hanning window is also applied to the turn-by-turn position x_n to reduce the truncation errors as prescribed by Laskar.

The search for the maximum is operated using the Brent algorithm implemented in the Gnu Scientific Library [**7**]. In order to speed up the process a first guess of the line frequency is obtained from a discrete Fourier transform. For this purpose the power spectrum $|F_q|^2$ of the turn-by-turn position is calculated and a second order interpolation is used to estimate the frequency of the spectral line under investigation. The obtained initial guess is generally precise enough to reduce the required number of iterations of the Brent algorithm to less than 3.

Once the frequency ν_0 has been precisely determined, amplitude and phase are calculated as $\sqrt{|\mathcal{F}(\nu_0)|^2}$ and $\operatorname{atan}\left(\frac{\mathrm{Im}[\mathcal{F}(\nu_0)]}{\mathrm{Re}[\mathcal{F}(\nu_0)]}\right)$ respectively.

Up to now the natural damping of the signal has not been considered in the analysis, on the other hand the presence of damping, even if small, has two major consequences on the analysis which are an incorrect estimation of the spectral lines amplitude and a bad cancellation of the tune lines from the turn-by-turn position when calculating the "purged" signal.

In the case of small damping (as in the case of ALBA where a damping time of about 3000 turns is observed for both planes) the previous estimation of the frequency ν_0 and phase ϕ_0 of the tune lines is unaffected. Therefore we can proceed

to evaluate the amplitude A_0 and damping time τ_0 of the tune line by fitting the turn-by-turn position x_n with the function

$$X_n(A,\tau) = A \cdot \sin(2\pi n\nu_0 + \phi_0) \cdot e^{-n/\tau}, \tag{A.4}$$

where only the amplitude A and damping time τ are varied. The correct amplitude and damping time estimation can now be used to calculate a new "purged" signal as:

$$X_n^{\mathrm{p}} = x_n - X_n(A_0,\tau_0). \tag{A.5}$$

Before proceeding with the estimation the skew quadrupolar line (that decay with the same damping time as the tune line) the damping is removed from the "purged" signal, producing an "undamped" signal:

$$X_n^{\mathrm{u}} = X_n^{\mathrm{p}} \cdot e^{n/\tau}. \tag{A.6}$$

Amplitude and phase of the skew quadrupolar lines can now be calculated by evaluating Eq. A.3 at the proper frequency and following the same procedure used to evaluate amplitude and phase of the tune line.

Since the damping of the sextupolar lines is two times faster than the damping of the tune line a second "undamping" is operated. Therefore their amplitude and phase is evaluated following the same procedure employed for the skew quadrupolar lines.

Thus the full algorithm flow can be summarized as follows:

(1) A Fast Fourier transform followed by a second order interpolation is used to produce a first guess of the the tune line frequencies.

(2) A precise frequency estimation for the tune lines is obtained by numerically maximizing Eq. A.3, where the frequency guess obtained at point 1 is used as starting point for the optimization.

(3) Amplitude and decay time are now fitted while keeping frequency and phase fixed.

(4) A "purged" signal is created, by removing the tune line from the original signal.

(5) The estimated decay time of the tune line is used to remove the damping from the "purged" signal by multiplying the signal by an inverse damping law.

(6) Amplitude and phase of the coupling lines is estimated by evaluating Eq. A.3 on each plane using the tune frequency of the other plane.

(7) Step 5 is repeated another time in order to evaluate higher order lines that decay two times as fast as the tune line.

(8) Amplitude and phase of the sextupolar lines are estimated by evaluating Eq. A.3 using the proper combination of tunes frequencies.

In order to speed up the analysis, the whole algorithm has been implemented as a compiled code library using the computer programming language C (see Annex II). With such precaution it was possible analyzing in just a few minutes large datasets comprising up to 500 acquisitions, each one containing 1000 turn-by-turn beam position measurements for both planes. The library has been wrapped to Matlab for easiness of use.

ANNEX I

Elegant Patch

Main routine of the Elegant simulation code patch. The new routine enables the calculation of the first-order corrections to the transverse motion due to skew quadrupoles and sextupoles in Elegant.

```
1  void computeSDrivingTerms(LINE_LIST *beamline)
2  {
3
4    /* Skew quadrupole */
5    std::complex <double> f10010, f10100;
6    /* Normal sextupole */
7    std::complex <double> f30000, f12000, f10200, f01200, f01110;
8    /* Skew Sextupole */
9    std::complex <double> f00300, f00120, f20100, f20010, f11010;
10
11   std::complex <double> ii = std::complex<double>(0,1);
12
13   double tilt;
14   double k2;                /* k2 <- normal sext */
15   double j1, j2;            /* j1 <- skew quad, j2 <- skew sext */
16   double src_betax, src_betay;   /* betas where the source is located */
17   double obs_phix, obs_phiy;
18   double src_phix, src_phiy;
19   double delta_phix, delta_phiy; /* phase advance between source and
       observator */
20   double qx, qy;          /* tunes */
21
22   int count;
23   int idx;
24
25   ELEMENT_LIST *src_ptr, *obs_ptr;
26
27   qx = beamline->tune[0];
28   qy = beamline->tune[1];
29
30   if (beamline->sDrivingTerms.f10010 == NULL) {
```

```
31      beamline->sDrivingTerms.f10010 = (double (*)[3])malloc(sizeof(double
        [3]) * beamline->n_elems);
32      beamline->sDrivingTerms.f10100 = (double (*)[3])malloc(sizeof(double
        [3]) * beamline->n_elems);
33      beamline->sDrivingTerms.f30000 = (double (*)[3])malloc(sizeof(double
        [3]) * beamline->n_elems);
34      beamline->sDrivingTerms.f12000 = (double (*)[3])malloc(sizeof(double
        [3]) * beamline->n_elems);
35      beamline->sDrivingTerms.f10200 = (double (*)[3])malloc(sizeof(double
        [3]) * beamline->n_elems);
36      beamline->sDrivingTerms.f01200 = (double (*)[3])malloc(sizeof(double
        [3]) * beamline->n_elems);
37      beamline->sDrivingTerms.f01110 = (double (*)[3])malloc(sizeof(double
        [3]) * beamline->n_elems);
38      beamline->sDrivingTerms.f00300 = (double (*)[3])malloc(sizeof(double
        [3]) * beamline->n_elems);
39      beamline->sDrivingTerms.f00120 = (double (*)[3])malloc(sizeof(double
        [3]) * beamline->n_elems);
40      beamline->sDrivingTerms.f20100 = (double (*)[3])malloc(sizeof(double
        [3]) * beamline->n_elems);
41      beamline->sDrivingTerms.f20010 = (double (*)[3])malloc(sizeof(double
        [3]) * beamline->n_elems);
42      beamline->sDrivingTerms.f11010 = (double (*)[3])malloc(sizeof(double
        [3]) * beamline->n_elems);
43    }
44
45    idx = 0;
46    obs_ptr = beamline->elem_twiss;
47    while (obs_ptr) {  /* loop over each observation point */
48
49      f10010 = f10100 = f30000 = f12000 =
50      f10200 = f01200 = f01110 = f00300 =
51      f00120 = f20100 = f20010 = f11010 = std::complex<double>(0,0);
52
53      src_ptr = beamline->elem_twiss;
54
55      if (obs_ptr->pred) {
56        obs_phix  = (obs_ptr->twiss->phix + obs_ptr->pred->twiss->phix)/2;
57        obs_phiy  = (obs_ptr->twiss->phiy + obs_ptr->pred->twiss->phiy)/2;
58      } else {
59        obs_phix  = (obs_ptr->twiss->phix + beamline->twiss0->phix)/2;
60        obs_phiy  = (obs_ptr->twiss->phiy + beamline->twiss0->phiy)/2;
61      }
62
```

```
63      while (src_ptr) {  /* loop over each source */
64        k2 = j1 = j2 = 0.;  /* get source strength */
65        switch (src_ptr->type) {
66        case T_SEXT:
67          tilt = ((SEXT*)src_ptr->p_elem)->tilt;
68          k2 = ((SEXT *)src_ptr->p_elem)->k2 * ((SEXT *)src_ptr->p_elem)->
    length;
69          break;
70        case T_KSEXT:
71          tilt = ((KSEXT*)src_ptr->p_elem)->tilt;
72          k2 = ((KSEXT *)src_ptr->p_elem)->k2 *
73               ((KSEXT *)src_ptr->p_elem)->length;
74          break;
75        case T_KQUSE:
76          tilt = ((KQUSE*)src_ptr->p_elem)->tilt;
77          j1 = -((KQUSE*)src_ptr->p_elem)->k1 *
78               ((KQUSE*)src_ptr->p_elem)->length * sin(2. * tilt);
79          k2 = ((KQUSE*)src_ptr->p_elem)->k2 * ((KQUSE*)src_ptr->p_elem)->
    length;
80          break;
81        case T_SBEN:
82        case T_RBEN:
83          tilt = ((BEND*)src_ptr->p_elem)->tilt;
84          j1 = -((BEND*)src_ptr->p_elem)->k1 *
85               ((BEND*)src_ptr->p_elem)->length * sin(2. * tilt);
86          k2 = ((BEND*)src_ptr->p_elem)->k2 * ((BEND*)src_ptr->p_elem)->
    length;
87          break;
88        case T_CSBEND:
89          tilt = ((CSBEND*)src_ptr->p_elem)->tilt;
90          j1 = -((CSBEND*)src_ptr->p_elem)->k1 *
91               ((CSBEND*)src_ptr->p_elem)->length * sin(2. * tilt);
92          k2 = ((CSBEND*)src_ptr->p_elem)->k2 *
93               ((CSBEND*)src_ptr->p_elem)->length;
94          break;
95        case T_CSRCSBEND:
96          tilt = ((CSRCSBEND*)src_ptr->p_elem)->tilt;
97          j1 = -((CSRCSBEND*)src_ptr->p_elem)->k1 *
98               ((CSRCSBEND*)src_ptr->p_elem)->length * sin(2. * tilt);
99          k2 = ((CSRCSBEND*)src_ptr->p_elem)->k2 *
100              ((CSRCSBEND*)src_ptr->p_elem)->length;
101         break;
102       case T_QUAD:
103         tilt = ((QUAD*)src_ptr->p_elem)->tilt;
```

```
104         j1 = -((QUAD*)src_ptr->p_elem)->k1 *
105              ((QUAD*)src_ptr->p_elem)->length * sin(2. * tilt);
106         break;
107       case T_KQUAD:
108         tilt = ((KQUAD*)src_ptr->p_elem)->tilt;
109         j1 = -((KQUAD*)src_ptr->p_elem)->k1 *
110              ((KQUAD*)src_ptr->p_elem)->length * sin(2. * tilt);
111         break;
112       default:
113         break;
114       }
115
116       if (!(k2 || j1 || j2)) {
117         src_ptr = src_ptr->succ;
118         continue;
119       }
120
121       /* Apply rotation */
122       j2 = -k2 * sin(3. * tilt);
123       k2 *= cos(3. * tilt);
124
125       if (src_ptr->pred) {
126         src_betax = (src_ptr->twiss->betax + src_ptr->pred->twiss->betax)
    /2;
127         src_betay = (src_ptr->twiss->betay + src_ptr->pred->twiss->betay)
    /2;
128         src_phix = (src_ptr->twiss->phix + src_ptr->pred->twiss->phix)/2;
129         src_phiy  = (src_ptr->twiss->phiy + src_ptr->pred->twiss->phiy)/2;
130       } else {
131         src_betax = (src_ptr->twiss->betax + beamline->twiss0->betax)/2;
132         src_betay = (src_ptr->twiss->betay + beamline->twiss0->betay)/2;
133         src_phix  = (src_ptr->twiss->phix + beamline->twiss0->phix)/2;
134         src_phiy  = (src_ptr->twiss->phiy + beamline->twiss0->phiy)/2;
135       }
136
137       delta_phix = obs_phix - src_phix;
138       delta_phiy = obs_phiy - src_phiy;
139
140       if (delta_phix < 0.) {
141         delta_phix += 2. * M_PI * qx;
142       }
143
144       if (delta_phiy < 0.) {
145         delta_phiy += 2. * M_PI * qy;
```

```
146       }
147
148       f10010 += j1 * sqrt(src_betax * src_betay) * exp(ii * (delta_phix -
        delta_phiy));
149       f10100 += j1 * sqrt(src_betax * src_betay) * exp(ii * (delta_phix +
        delta_phiy));
150       f30000 += k2 * src_betax * sqrt(src_betax) * exp(3. * ii * delta_phix
        );
151       f12000 += k2 * src_betax * sqrt(src_betax) * exp(-ii * delta_phix);
152       f10200 += k2 * sqrt(src_betax) * src_betay * exp(ii * (delta_phix +
        2. * delta_phiy));
153       f01200 += k2 * sqrt(src_betax) * src_betay * exp(ii * (2. *
        delta_phiy - delta_phix));
154       f01110 += k2 * sqrt(src_betax) * src_betay * exp(-ii * delta_phix);
155       f00300 += j2 * src_betay * sqrt(src_betay) * exp(ii * 3. * delta_phiy
        );
156       f00120 += j2 * src_betay * sqrt(src_betay) * exp(-ii * delta_phiy);
157       f20100 += j2 * src_betax * sqrt(src_betay) * exp(ii * (2. *
        delta_phix + delta_phiy));
158       f20010 += j2 * src_betax * sqrt(src_betay) * exp(ii * (2. *
        delta_phix - delta_phiy));
159       f11010 += j2 * src_betax * sqrt(src_betay) * exp(-ii * delta_phiy);
160
161       src_ptr = src_ptr->succ;
162     }
163     f10010 /= 4. * (1. - exp( 2. * M_PI * ii * (qx - qy)));
164     f10100 /= 4. * (1. - exp( 2. * M_PI * ii * (qx + qy)));
165     f30000 /= 48.* (1. - exp( 2. * M_PI * ii * 3. * qx));
166     f12000 /= 16.* (1. - exp( 2. * M_PI * ii * qx));
167     f10200 /= 16.* (1. - exp( 2. * M_PI * ii * (qx + 2. * qy)));
168     f01200 /= 16.* (1. - exp( 2. * M_PI * ii * (2. * qy - qx)));
169     f01110 /= 8. * (1. - exp(-2. * M_PI * ii * qx));
170     f00300 /= 48.* (1. - exp( 2. * M_PI * ii * 3. * qy));
171     f00120 /= 16.* (1. - exp(-2. * M_PI * ii * qy));
172     f20100 /= 16.* (1. - exp( 2. * M_PI * ii * (2. * qx + qy)));
173     f20010 /= 16.* (1. - exp( 2. * M_PI * ii * (2. * qx - qy)));
174     f11010 /= 8.*  (1. - exp(-2. * M_PI * ii * qy));
175
176     beamline->sDrivingTerms.f10010[idx][0] = std::abs<double>(f10010);
177     beamline->sDrivingTerms.f10100[idx][0] = std::abs<double>(f10100);
178     beamline->sDrivingTerms.f30000[idx][0] = std::abs<double>(f30000);
179     beamline->sDrivingTerms.f12000[idx][0] = std::abs<double>(f12000);
180     beamline->sDrivingTerms.f10200[idx][0] = std::abs<double>(f10200);
181     beamline->sDrivingTerms.f01200[idx][0] = std::abs<double>(f01200);
```

```
182     beamline->sDrivingTerms.f01110[idx][0] = std::abs<double>(f01110);
183     beamline->sDrivingTerms.f00300[idx][0] = std::abs<double>(f00300);
184     beamline->sDrivingTerms.f00120[idx][0] = std::abs<double>(f00120);
185     beamline->sDrivingTerms.f20100[idx][0] = std::abs<double>(f20100);
186     beamline->sDrivingTerms.f20010[idx][0] = std::abs<double>(f20010);
187     beamline->sDrivingTerms.f11010[idx][0] = std::abs<double>(f11010);
188
189     beamline->sDrivingTerms.f10010[idx][1] = f10010.real();
190     beamline->sDrivingTerms.f10100[idx][1] = f10100.real();
191     beamline->sDrivingTerms.f30000[idx][1] = f30000.real();
192     beamline->sDrivingTerms.f12000[idx][1] = f12000.real();
193     beamline->sDrivingTerms.f10200[idx][1] = f10200.real();
194     beamline->sDrivingTerms.f01200[idx][1] = f01200.real();
195     beamline->sDrivingTerms.f01110[idx][1] = f01110.real();
196     beamline->sDrivingTerms.f00300[idx][1] = f00300.real();
197     beamline->sDrivingTerms.f00120[idx][1] = f00120.real();
198     beamline->sDrivingTerms.f20100[idx][1] = f20100.real();
199     beamline->sDrivingTerms.f20010[idx][1] = f20010.real();
200     beamline->sDrivingTerms.f11010[idx][1] = f11010.real();
201
202     beamline->sDrivingTerms.f10010[idx][2] = f10010.imag();
203     beamline->sDrivingTerms.f10100[idx][2] = f10100.imag();
204     beamline->sDrivingTerms.f30000[idx][2] = f30000.imag();
205     beamline->sDrivingTerms.f12000[idx][2] = f12000.imag();
206     beamline->sDrivingTerms.f10200[idx][2] = f10200.imag();
207     beamline->sDrivingTerms.f01200[idx][2] = f01200.imag();
208     beamline->sDrivingTerms.f01110[idx][2] = f01110.imag();
209     beamline->sDrivingTerms.f00300[idx][2] = f00300.imag();
210     beamline->sDrivingTerms.f00120[idx][2] = f00120.imag();
211     beamline->sDrivingTerms.f20100[idx][2] = f20100.imag();
212     beamline->sDrivingTerms.f20010[idx][2] = f20010.imag();
213     beamline->sDrivingTerms.f11010[idx][2] = f11010.imag();
214
215     idx++;
216     obs_ptr = obs_ptr->succ;
217   }
218 }
```

elegant/twiss.cc

ANNEX II

Spectral Analysis Code

The code is organized as a library where the function *pf_find*, contained in *pf.c*, represents the main entry point to carry out the spectral analysis of turn-by-turn data.

```
#define PARAMS_COUNT 4

#define OMEGA(n) (0 + PARAMS_COUNT * n)
#define PHI(n)       (1 + PARAMS_COUNT * n)
#define AMP(n) (2 + PARAMS_COUNT * n)
#define DECAY(n) (3 + PARAMS_COUNT * n)

extern double *hanning_window;
```

libpf–0.3/src/pf_utils.h

```

double *
pf_find(double *data_x, double *data_y, int turns, double tune_bound[4]);
```

libpf–0.3/src/pf.h

```
#include <stdio.h>
#include <stdlib.h>
#include <math.h>

#include "pf_utils.h"
#include "guess.h"
#include "fa.h"
#include "fa_utils.h"
#include "damping.h"

double *hanning_window;

double *
pf_find(double *data_x, double *data_y, int turns, double tune_bound[4])
{
```

```
16  double *guess_x, *guess_y;
17  double *windowed_data;
18  double qx, qy;
19  int l, lines;
20
21  /* Tune lines and skew are calculated apart */
22  double line_table[4][2] = {{-2, 0}, {0, -2}, {-1, -1}, {1, -1}};
23  lines = 6;  /* Lines for each plane */
24
25  guess_x = malloc(sizeof(double) * PARAMS_COUNT * lines * 2);
26  guess_y = &guess_x[PARAMS_COUNT * lines];
27
28  hanning_window = malloc(sizeof(double) * turns);
29  windowed_data = malloc(sizeof(double) * turns);
30
31  init_guess(turns);
32  init_hanning(turns);
33
34  /* X plane tune analysis */
35  window_data(data_x, windowed_data, turns);
36
37  if(guess_tune(windowed_data, turns, guess_x, &tune_bound[0]))
38    goto error;
39
40  freq_an(windowed_data, turns, guess_x);
41
42  guess_x[DECAY(0)] = -0.0003;
43
44  fit_damping(data_x, turns, guess_x);
45
46  subtract_and_undump(data_x, turns, guess_x);
47
48  /* Y plane tune analysis */
49        window_data(data_y, windowed_data, turns);
50
51        if(guess_tune(windowed_data, turns, guess_y, &tune_bound[2]))
52                goto error;
53
54        freq_an(windowed_data, turns, guess_y);
55
56        guess_y[DECAY(0)] = -0.0003;
57
58        fit_damping(data_y, turns, guess_y);
59
```

```
60          subtract_and_undump(data_y, turns, guess_y);
61
62      /* X plane higher order analysis */
63
64      window_data(data_x, windowed_data, turns);
65
66      qx = guess_x[OMEGA(0)];
67      qy = guess_y[OMEGA(0)];
68
69      l = 1;
70      /* Calculate skew lines */
71      guess_x[OMEGA(l)] = qy;
72      ortho_projection(windowed_data, turns, guess_x[OMEGA(l)],
73                              &guess_x[PHI(l)], &guess_x[AMP(l)]);
74
75
76      /* Times for sextupoles and octupoles */
77      undump(windowed_data, turns, guess_x[DECAY(0)]);
78          for (l = 2; l < lines; l++) {
79                  guess_x[OMEGA(l)] = line_table[l - 2][0] * qx + line_table[
        l - 2][1] * qy;
80
81                  ortho_projection(windowed_data, turns, guess_x[OMEGA(l)],
82                                  &guess_x[PHI(l)], &guess_x[AMP(l)]);
83
84          }
85
86
87          /* Y plane higher order analysis */
88
89          window_data(data_y, windowed_data, turns);
90
91          l = 1;
92          /* Calculate skew lines */
93          guess_y[OMEGA(l)] = qx;
94          ortho_projection(windowed_data, turns, guess_y[OMEGA(l)],
95                          &guess_y[PHI(l)], &guess_y[AMP(l)]);
96
97
98          /* Times for sextupoles and octupoles */
99      undump(windowed_data, turns, guess_y[DECAY(0)]);
100         for (l = 2; l < lines; l++) {
101                 guess_y[OMEGA(l)] = line_table[l - 2][0] * qy + line_table[
        l - 2][1] * qx;
```

```
102
103                 ortho_projection(windowed_data, turns, guess_y[OMEGA(1)],
104                                  &guess_y[PHI(1)], &guess_y[AMP(1)]);
105
106         }
107
108 error:
109   release_guess();
110   free(hanning_window);
111   free(windowed_data);
112
113   /* Guess_y is allocated after guess_x */
114   return guess_x;
115 }
```

libpf–0.3/src/pf.c

```
1 void init_guess(int turns);
2 void release_guess(void);
3 int guess_tune(double *data, int turns, double *guess, double tune_bound
      [2]);
```

libpf–0.3/src/guess.h

```
1 #include <stdlib.h>
2 #include <string.h>
3 #include <math.h>
4 #include <gsl/gsl_fft_real.h>
5 #include <gsl/gsl_fft_halfcomplex.h>
6
7 #include "pf_utils.h"
8
9 double *amp, *buf;
10 gsl_fft_real_wavetable *wave;
11 gsl_fft_real_workspace *work;
12
13 /* Find first "count" peaks.
14  * Warning: derivative vector gets modified */
15 int
16 spot_peaks(double *buf, int count, double tune_bound[2])
17 {
18   int i;
19   int peak;
20   int low, hi;
```

```
21   double aux;
22
23   low = 2. * tune_bound[0] * (double)count;
24   hi = 2. * tune_bound[1] * (double)count;
25
26   aux = 0.;
27   peak = -1;
28   for (i = low; i < hi; i++) {
29
30     if (buf[i] > aux) {
31       aux = buf[i];
32       peak = i;
33     }
34   }
35
36   if (peak == i - 1)
37     peak = -1;
38
39   return peak;
40 }
41
42 void
43 init_guess(int turns)
44 {
45         amp = malloc(sizeof(double) * turns / 2);
46         buf = malloc(sizeof(double) * turns);
47
48         work = gsl_fft_real_workspace_alloc(turns);
49         wave = gsl_fft_real_wavetable_alloc(turns);
50 }
51
52 void
53 release_guess()
54 {
55         free(buf);
56         free(amp);
57
58         gsl_fft_real_workspace_free(work);
59   gsl_fft_real_wavetable_free(wave);
60 }
61
62 /* On success returns 0 */
63 int
64 guess_tune(double *data, int turns, double *guess, double tune_bound[2])
```

```
65 {
66   double alpha, beta, gamma;
67   double p;
68         int i, j;
69   int peak;
70
71   /* Copy data */
72   for (i = 0; i < turns; i++) {
73     buf[i] = data[i];
74   }
75
76         gsl_fft_real_transform(buf, 1, turns, wave, work);
77
78   /* Skip the offset */
79   amp[0] = 0;
80   j = 1;
81   /* 2j - 1 = i */
82   for (i = 1; i < turns - 1; i += 2) {
83     amp[j] = buf[i] * buf[i] +
84                           buf[i + 1] * buf[i + 1];
85     j++;
86   }
87
88   /* Remember the spectrum has half points of the data buffer */
89   peak = spot_peaks(amp, turns / 2, tune_bound);
90   if (peak == -1)
91     return -1;
92
93   /* Omega from quadratic interpolation */
94   alpha = sqrt(amp[peak - 1]);
95   beta = sqrt(amp[peak]);
96   gamma = sqrt(amp[peak + 1]);
97
98   p = 0.5 * (alpha - gamma) / (alpha - 2. * beta + gamma);
99
100  guess[0] = p;
101  guess[0] += peak;
102
103  guess[0] *= 2. * M_PI / (double)turns;
104
105  return 0;
106 }
```

libpf–0.3/src/guess.c

```
1 void freq_an(double *buf, int turns, double *guess);
```

libpf–0.3/src/fa.h

```
1 #include <math.h>
2 #include <gsl/gsl_errno.h>
3 #include <gsl/gsl_math.h>
4 #include <gsl/gsl_min.h>
5
6 #include "pf_utils.h"
7 #include "fa_utils.h"
8
9 struct Data {
10         double *buf;        /* Data to be fitted */
11         int turns;          /* Number of turns */
12 };
13
14 double
15 test_amplitude(double q, void *param)
16 {
17         int i, count;
18   double *buf;
19         double im, re;
20   double amp;
21
22   buf = ((struct Data *)param)->buf;
23   count = ((struct Data *)param)->turns;
24
25         re = 0.;
26         im = 0.;
27
28         for (i = 0; i < count; i++) {
29                 im += buf[i] * sin(q * (double)i);
30                 re += buf[i] * cos(q * (double)i);
31         }
32
33         amp = hypot(im, re);
34
35   return -1. * amp;
36 }
37
38 void
39 freq_an(double *data, int turns, double *guess)
40 {
```

```
41  int status;
42  int iter;
43  gsl_min_fminimizer *minimizer;
44  double omega;
45  double lower_bound, upper_bound;
46  gsl_function f;
47
48  struct Data fit_data;
49
50  fit_data.buf = data;
51  fit_data.turns = turns;
52
53  omega = guess[OMEGA(0)];
54
55  lower_bound = omega - 2. * M_PI / (double)turns;
56  upper_bound = omega + 2. * M_PI / (double)turns;
57
58  if (test_amplitude(omega, &fit_data) > test_amplitude(lower_bound, &
      fit_data) ||
59      test_amplitude(omega, &fit_data) > test_amplitude(upper_bound, &
      fit_data)) {
60    return;
61  }
62
63  f.function = &test_amplitude;
64  f.params = &fit_data;
65
66  minimizer = gsl_min_fminimizer_alloc(gsl_min_fminimizer_brent);
67  gsl_min_fminimizer_set(minimizer, &f, omega,
68              lower_bound, upper_bound);
69
70  iter = 0;
71  do {
72    iter++;
73    status = gsl_min_fminimizer_iterate(minimizer);
74
75    omega = gsl_min_fminimizer_x_minimum(minimizer);
76    lower_bound = gsl_min_fminimizer_x_lower(minimizer);
77    upper_bound = gsl_min_fminimizer_x_upper(minimizer);
78
79    status = gsl_min_test_interval(lower_bound, upper_bound, 1e-6, 1e-6);
80
81  } while (status == GSL_CONTINUE && iter < 10);
82
```

```
83   ortho_projection(data, turns, omega,
84                    &guess[PHI(0)], &guess[AMP(0)]);
85
86   guess[OMEGA(0)] = omega;
87
88   gsl_min_fminimizer_free(minimizer);
89 }
```

libpf–0.3/src/fa.c

```
1 void ortho_projection(double *buf, int count, double q,
2                       double *phase, double *amplitude);
3
4 void init_hanning(int count);
5
6 void window_data(double *data, double *windowed_data, int turns);
7
8 void undump(double *data, int turns, double k);
9
10 void subtract_and_undump(double *data, int turns, double *guess);
```

libpf–0.3/src/fa_utils.h

```
1 #include <math.h>
2
3 #include "pf_utils.h"
4
5 void
6 ortho_projection(double *buf, int count, double q,
7                  double *phase, double *amplitude)
8 {
9         int i;
10        double im, re;
11
12        re = 0.;
13        im = 0.;
14
15        for (i = 0; i < count; i++) {
16                im += buf[i] * sin(q * (double)i);
17                re += buf[i] * cos(q * (double)i);
18        }
19
20        *amplitude = hypot(im, re) * 2. / (count - 1.);
21        *phase = -atan2(im, re);
```

```
22 }
23
24 /* Hanning window */
25 void
26 init_hanning(int count)
27 {
28         int i;
29   double *window;
30
31   window = hanning_window;
32
33         for (i = 0; i < count; i++) {
34                 window[i] = cos(2. * M_PI * (double)i / (double)(count - 1)
       );
35                 window[i] = (1. - window[i]);
36         }
37 }
38
39 void
40 window_data(double *data, double *windowed_data, int turns)
41 {
42         int i;
43
44         for (i = 0; i < turns; i++) {
45                 windowed_data[i] = hanning_window[i] * data[i];
46         }
47 }
48
49 void
50 undump(double *data, int turns, double k)
51 {
52         int t;
53
54         for (t = 0; t < turns; t++) {
55                 data[t] *= exp(- k * t);
56         }
57 }
58
59 void
60 subtract_and_undump(double *data, int turns, double *guess)
61 {
62   int t;
63   double omega, a, phi, k;
64
```

```
65   omega = guess[OMEGA(0)];
66   a = guess[AMP(0)];
67   phi = guess[PHI(0)];
68   k = guess[DECAY(0)];
69
70   for (t = 0; t < turns; t++) {
71     data[t] *= exp(- k * t);
72     data[t] -= a * cos(omega * t + phi);
73   }
74 }
```

libpf–0.3/src/fa_utils.c

```
1 void fit_damping(double *buf, int turns, double *guess);
```

libpf–0.3/src/damping.h

```
1 #include <math.h>
2 #include <gsl/gsl_multifit_nlin.h>
3 #include <gsl/gsl_blas.h>
4
5 #include "pf_utils.h"
6
7 struct Data {
8         double *y;          /* Data to be fitted */
9         int turns;          /* Number of turns */
10   double omega;
11   double phi;
12 };
13
14 int
15 tune_f (const gsl_vector *x, void *data,
16        gsl_vector *f)
17 {
18         double *y;
19         double aux;
20         double omega, phi, a, k;
21         int turns, t;
22
23         turns = ((struct Data *)data)->turns;
24         y = ((struct Data *)data)->y;
25   omega = ((struct Data *)data)->omega;
26   phi = ((struct Data *)data)->phi;
27
```

```
28          for (t = 0; t < turns; t++) {
29      a = gsl_vector_get(x, 0);
30                  k = gsl_vector_get(x, 1);
31
32                  aux = a * cos(omega * t + phi) * exp(t * k);
33                  gsl_vector_set(f, t, aux - y[t]);
34          }
35
36          return GSL_SUCCESS;
37  }
38
39  int
40  tune_df (const gsl_vector * x, void *data,
41          gsl_matrix * J)
42  {
43          double omega, phi, a, k;
44          double d_a, d_k;
45          int turns, t;
46
47          turns = ((struct Data *)data)->turns;
48          omega = ((struct Data *)data)->omega;
49          phi = ((struct Data *)data)->phi;
50
51          for (t = 0; t < turns; t++) {
52      a = gsl_vector_get(x, 0);
53                  k = gsl_vector_get(x, 1);
54
55      d_a =          cos(omega * t + phi) * exp(t * k);
56                  d_k = t * a * cos(omega * t + phi) * exp(t * k);
57
58      gsl_matrix_set(J, t, 0, d_a);
59                  gsl_matrix_set(J, t, 1, d_k);
60          }
61
62          return GSL_SUCCESS;
63  }
64
65  int
66  tune_fdf (const gsl_vector * x, void *data,
67           gsl_vector * f, gsl_matrix * J)
68  {
69          tune_f (x, data, f);
70          tune_df (x, data, J);
71
```

```
72          return GSL_SUCCESS;
73  }
74
75  void
76  fit_damping(double *buf, int turns, double *guess)
77  {
78          gsl_multifit_fdfsolver *s;
79
80          int iter;
81          int status;
82
83          struct Data data;
84
85          data.turns = turns;
86          data.y = buf;
87    data.omega = guess[OMEGA(0)];
88    data.phi = guess[PHI(0)];
89
90          gsl_vector_view x;
91    /* Amplitude and decay are stored one after the other in the guess vector
         */
92    x = gsl_vector_view_array(&guess[AMP(0)], 2);
93
94          gsl_multifit_function_fdf f;
95
96          f.f = &tune_f;
97          f.df = &tune_df;
98          f.fdf = &tune_fdf;
99          f.n = turns;
100         f.p = 2;
101         f.params = &data;
102
103         s = gsl_multifit_fdfsolver_alloc(gsl_multifit_fdfsolver_lmsder,
104            turns, 2);
105         gsl_multifit_fdfsolver_set(s, &f, &x.vector);
106
107         iter = 0;
108         do {
109                 iter++;
110                 status = gsl_multifit_fdfsolver_iterate(s);
111
112                 if (status)
113                         break;
114
```

```
115                 status = gsl_multifit_test_delta(s->dx, s->x,
116                                                  1e-6, 1e-6);
117
118         } while (status == GSL_CONTINUE && iter < 10);
119
120   /* Copy back results (s->x) on to the initial guess vector (x) */
121   gsl_vector_memcpy (&x.vector, s->x);
122
123   gsl_multifit_fdfsolver_free(s);
124 }
```

libpf–0.3/src/damping.c

Bibliography

[1] `http://www.i-tech.si`.

[2] `http://www.cmi-ferrite.com/`.

[3] `http://www.behlke.com/`.

[4] `http://www.netlib.org/lapack/`.

[5] `www.gdfidl.de`.

[6] `http://www.ohwr.org/projects/bpm/wiki`.

[7] `https://www.gnu.org/software/gsl/`.

[8] M. Aiba, M. Böge, J. Chrin, N. Milas, T. Schilcher, and A. Streun. Comparison of linear optics measurement and correction methods at the swiss light source. *Phys. Rev. ST Accel. Beams*, 16:012802, Jan 2013.

[9] G. Arduini, C. Carli, and F. Zimmermann. Localizing impedance sources from betatron phase beating in the CERN SPS. In *9th European Particle Accelerator Conference (EPAC 2004) Lucerne, Switzerland, July 5-9, 2004*, 2004.

[10] R. Bartolini, I. P. S. Martin, G. Rehm, and F. Schmidt. Calibration of the nonlinear ring model at the diamond light source. *Phys. Rev. ST Accel. Beams*, 14:054003, May 2011.

[11] G. Benedetti, D. Einfeld, Z. Martì, and M. Munoz. LOCO in the ALBA Storage Ring. *Conf. Proc.*, C110904:2055–2057, 2011.

[12] N. Biancacci and R. Tomás. Using ac dipoles to localize sources of beam coupling impedance. *Phys. Rev. Accel. Beams*, 19:054001, May 2016.

[13] Nicolo Biancacci, Michael Blaskiewicz, Yann Dutheil, Chuyu Liu, Kevin Mernick, Michiko Minty, and Simon White. Transverse Impedance Measurement in RHIC and the AGS. In *Proceedings, 5th International Particle Accelerator Conference (IPAC 2014), Dresden, Germany*, page TUPRI071, 2014.

[14] M. Borland. Elegant: A Flexible SDDS-Compliant Code for Accelerator Simulation, Advanced Photon Source LS-287, 2000.

[15] P. Brunelle, J. M. Filhol, M. P. Gacoin, C. Herbeaux, M. P. Level, A. Loulergue, O. Marcouille, A. Nadji, D. Raoux, and M. A. Tordeux. A synchrotron called SOLEIL: Main characteristics of the French synchrotron source. *ICFA Beam Dyn. Newslett.*, 28:11–18, 2002.

[16] Rama Calaga, Gianluigi Arduini, Elias Métral, Giulia Papotti, Diego Quatraro, Giovanni Rumolo, Benoit Salvant, and Rogelio Tomás. Transverse Impedance Localization Using Dependent Optics. In *Particle accelerator. Proceedings, 23rd Conference, PAC'09, Vancouver, Canada, May 4-8, 2009*, page FR5RFP034, 2010.

[17] A. W. Chao. *Physics of collective beam instabilities in high energy accelerators*. Wiley, 1993.

[18] E.D Courant and H.S Snyder. Theory of the alternating-gradient synchrotron. *Annals of Physics*, 3(1):1 – 48, 1958.

[19] D. Einfeld. ALBA Synchrotron Light Source Commissioning. *Conf. Proc.*, C110904:1–5, 2011.

[20] D. Einfeld, M. Belgroune, G. Benedetti, M. De Lima, J. Marcos, M. Munoz, and M. Pont. Modelling of gradient bending magnets for the beam dynamics studies at alba. In *2007 IEEE Particle Accelerator Conference (PAC)*, pages 1076–1078, June 2007.

[21] A. Franchi, L. Farvacque, F. Ewald, G. Le Bec, and K. B. Scheidt. First simultaneous measurement of sextupolar and octupolar resonance driving terms in a circular accelerator from turn-by-turn beam position monitor data. *Phys. Rev. ST Accel. Beams*, 17:074001, Jul 2014.

[22] J. G. F. Francis. The qr transformation a unitary analogue to the lr transformationpart 1. *The Computer Journal*, 4(3):265–271, 1961.

[23] G Benedetti, D Einfeld, Z Mart, and M Muoz. Loco in the alba storage ring. 2011.

[24] Z. Martí G. Benedetti, J. Campmany. Low horizontal beta optics for alba. In *Proceedings of IPAC2016, Busan, Korea*, page THPMR035, 2016.

[25] T. Günzel and Perez F. Impedance and instabilities for the alba storage ring. *Conf. Proc.*, 2008.

[26] Thomas Günzel and Ubaldo Iriso. Revision of the Impedance Model for the Interpretation of the Single Bunch Measurements at ALBA. In *Proceedings, 6th International Particle Accelerator Conference (IPAC 2015), Richmond, Virginia*, page MOPJE026, 2015.

[27] Nicolas Hubert, Benot Branger, and Laurent Nadolski. BPM Data Correction at SOLEIL. In *Proceedings, 5th International Particle Accelerator Conference (IPAC 2014): Dresden, Germany, June 15-20, 2014*, page THPME083, 2014.

[28] A. Kosicek, V. Poucki, T. Karcnik, and B. K. Scheidt. Modified digital filtering makes possible *True & Pure* t-b-t measurements. In *Proceedings of BIW08, Lake Tahoe*, 2008.

[29] A. Langner, G. Benedetti, M. Carlà, U. Iriso, Z. Martí, J. Coello de Portugal, and R. Tomás. Utilizing the n beam position monitor method for turn-by-turn optics measurements. *Phys. Rev. Accel. Beams*, 19:092803, Sep 2016.

[30] Jacques Laskar, Claude Froeschl, and Alessandra Celletti. The measure of chaos by the numerical analysis of the fundamental frequencies. application to the standard mapping. *Physica D: Nonlinear Phenomena*, 56(2):253 – 269, 1992.

[31] P. Lebasque, R. Ben El Fekih, M. Bol, J. P. Lavieville, A. Loulergue, and D. Muller. Improvement on Pulsed Magnetic Systems at SOLEIL. *Conf. Proc.*, C0806233:WEPC081, 2008.

[32] Z. Martí. LOCO accuracy simulations with ALBA lattice. *Internal report*, 2013.

[33] J. Mueller and S. Siltanen. *Linear and Nonlinear Inverse Problems with Practical Applications*. Society for Industrial and Applied Mathematics, Philadelphia, PA, 2012.

[34] Marc Munoz and Dieter Einfeld. Lattice and beam dynamics of the ALBA storage ring. *ICFA Beam Dyn. Newslett.*, 44:183–193, 2007.

[35] R. Nunez, M. Pont, and E. Huttel. Septum and Kicker Magnets for the ALBA Booster and Storage Ring. *Conf. Proc.*, C110904:2421–2423, 2011.

[36] Angel Olmos, Michael Abbott, Ubaldo Iriso, Jairo Moldes, Francis Prez, Guenther Rehm, and Isa Uzun. Integration of the Diamond Transverse Multibunch Feedback System at ALBA. In *Proceedings, 4th International Beam Instrumentation Conference, IBIC2015*, page TUPB046, 2016.

[37] B. Podobedov. Single micron single-bunch turn-by-turn bpm resolution achieved at nsls-ii. In *Proceedings of IPAC2016, Busan, Korea*, page WEOBB01, 2016.

[38] Montserrat Pont, Domingo Alloza, Roberto Petrocelli, David Yepez, Roger Camell, Gabriel Gross, and Miquel Teixido. Power Converters for ALBA Storage Ring. *Conf. Proc.*, C100523:WEPD066, 2010.

[39] R. núñez. Diseño de imanes pulsados para caracterizacion y diagnostico del anillo de almacenamiento del sincrotron ALBA. *Internal report*, 2010.

[40] James Safranek. Linear Optics from Closed Orbits (LOCO): An introduction. *ICFA Beam Dyn. Newslett.*, 44:43–49, 2007.

[41] Kees Scheidt. Modified (adjustable) ddc filters within libera brilliance - experience with partial fill patterns and pure t-b-t measurements. *white paper*.

[42] M. Takao. Impact of Betatron Motion on Path Lengthening and Momentum Aperture in a Storage Ring. *Conf. Proc.*, C0806233:THPC072, 2008.

[43] Andrei Terebilo. Accelerator toolbox for MATLAB. In *Workshop on Performance Issues at Synchrotron Light Sources Berkeley, California, October 2-4, 2000*, 2001.

[44] A. N. Tikhonov, A. V. Goncharsky, V. V. Stepanov, and A. G. Yagola. *Regularization methods*, pages 7–63. Springer Netherlands, Dordrecht, 1995.

[45] Rogelio Tomás, Masamitsu Aiba, Andrea Franchi, and Ubaldo Iriso. Review of linear optics measurement and correction for charged particle accelerators. *Phys. Rev. Accel. Beams*, 20:054801, May 2017.

[46] G. Vanbavinckhove, M. Aiba, A. Nadji, L Nadolski, R. Tomas, and M-A. Tordeux. LINEAR AND NON-LINEAR OPTICS MEASUREMENTS AT SOLEIL. In *Proceedings, Proceedings of PAC09, Vancouver, BC, Canada*.

[47] H. Wiedemann. *Particle Accelerator Physics I: Basic Principles and Linear Beam Dynamics*. Particle Accelerator Physics I. Springer Berlin Heidelberg, 2012.

[48] Curtis Wilson. *Hill on the Motion of the Lunar Perigee*, pages 31–53. Springer New York, New York, NY, 2010.